Signal Processing for Acoustic Arrays and for Single-Carrier Block-Based Transmission

SONG, Yang

Doctor of Philosophy

The Hong Kong Polytechnic University

2013

The Hong Kong Polytechnic University
Department of Electronic & Information Engineering

Signal Processing for Acoustic Arrays and for Single-Carrier Block-Based Transmission

SONG, Yang

A thesis submitted in partial fulfilment of the requirements
for the degree of Doctor of Philosophy

December 2012

CERTIFICATE OF ORIGINALITY

I hereby declare that this thesis is my own work and that, to the best of my knowledge and belief, it reproduces no material previously published or written, nor material that has been accepted for the award of any other degree or diploma, except where due acknowledgement has been made in the text.

_____ (Signed)

_____ (Name of Students)

Abstract

The dissertation has six contributions towards space-time signal processing for acoustic sensor arrays which are summarized below.

(1) Closed-form direction finding using collocated but orthogonally oriented higher-order acoustic sensors

This work introduces new closed-form formulas to estimate an incident source's azimuth-elevation angle-of-arrival (AOA), for various combinations of *higher-order* directional acoustic sensors, that are orthogonally oriented in a collocated triad.

(2) Azimuth-elevation direction finding using a microphone and three orthogonal velocity sensors as a non-collocated subarray

An acoustic vector-sensor consists of three identical but orthogonally oriented acoustic particle-velocity sensors, plus a pressure sensor - all spatially collocated in a point-like geometry. This collocation constriction is relaxed in this work, to realize a spatially distributed acoustic vector-sensor, allowing its four component-sensors to be separately located.

(3) Acoustic direction finding using a spatially spread tri-axial velocity sensor

This work shows how a triad of orthogonally oriented uni-axial velocity sensors may be spatially separated, yet facilitates direction finding of incident emitters via closed-form subspace-based parameter estimation algorithms, while extending the triads spatial aperture in three-dimensional space to enhance the resolution of the azimuth/elevation direction of arrival estimates.

(4) "Blind" calibration of an array of acoustic vector-sensors suffering gain errors / mis-location / mis-orientation

A series of direction-finding algorithms have recently been advanced, deploying a multi-array network (MAN) of acoustic-vector-sensors, each consisting of three collocated but diversely oriented uni-axial particle-velocity sensors, plus an optional pressure sensor. All these algorithms presume the particle-velocity sensors and the pressure sensors of ideal gain/phase responses, correct orientations, and (in some algorithms) precise locations. Such perfection is seldom (if ever) achieved in realworld systems or in field deployment. Indeed, these non-idealities need to be calibrated,

often blindly without any training signal from any prior known arrival-angle. Towards this end, this work will advance a new "blind" calibration algorithm (a.k.a. "auto-calibration", "self-calibration", or "unaided calibration") that is computationally orders-of-magnitude more efficient than maximum-likelihood estimation. These advantages are achieved here by exploiting the acoustic vector-sensor's quintessential characters, to interplay between two complementary approaches of direction-finding: (1) customary interferometry between vector-sensors, and (2) "acoustic particle-velocity-field normalization" DOA-estimation within each individual vector-sensor.

(5) A lower bound of direction-of-arrival estimation for an acoustic vector sensor subject to sensor breakdown

In an acoustic vector-sensor, any particular velocity sensor must either function or fail, over the entire time-window when measurements are collected. This work derives an approximate lower bound for the error-variance of direction-finding using a single acoustic vector sensor subject to random breakdown in its sensors.

(6) Three dimensional localization of a near-field emitter of unknown spectrum using an acoustic vector sensor

The work develops a parameter estimation algorithm to estimate a near field wide-band emitters azimuth elevation direction of arrival plus radial distance, based on data collected by one acoustic vector sensor. This new algorithm needs no prior knowledge of the incident sources spectrum.

The dissertation has two contributions towards signal processing for single-carrier block-based transmission/reception which are summarized below.

(1) A precoder/two-stage equalizer for block-based single-carrier transmission with an insufficient guard-interval

To reduce the cyclic-prefix overhead in block-based cyclically prefixed single-carrier modulation, herein proposed is a zeros-inserting precoder that can reduce the net overhead in symbols. This precoder allows the formation a data-group that contains only interference and noise but not the desired signal, thereby facilitating a subsequent "signal to interference-plus-noise" (SINR) maximizer. Also proposed is an accompanying two-stage linear equalizer, that may be pre-computed off-line. This equalizer's first stage is a linear minimum mean-square-error (LMMSE) based linear frequency-domain equalizer (FDE); the equalizer's second stage is its second stage is a SINR-maximizer in the time-domain. Monte Carlo simulations show the proposed scheme's capability to shorten the cyclic prefix (CP) more than the inserted number of zero-energy symbol-periods, thereby reducing the transmission's net overhead.

(2) "Blind" reception-beamforming to null unknown interference for block-based single-carrier transmission with an insufficient guard interval

This work proposes a "blind" beamformer to spatially pass the signal-of-interest, but to spatially null any co-channel interference, any adjacent-channel interference, any out-of-system interference, and/or any spatio-temporally correlated additive noises. This proposed scheme's transmission uses zero-padding in an insufficient guard interval, shorter than the temporally spreading channel's order. This proposed scheme's receiver first undergoes frequency-domain equalization, to "clear" the data of the signal-of-interests energy during the nominally zero-padded guard interval, to facilitate subsequent "signal-to-interference-and-noise ratio" maximization in the spatial dimension to realize the aforementioned "blind" beamformer.

Publications

Journal papers: (published / accepted)

1. Yeong-Tzay Su, **Y. Song** & K. T. Wong, "Linear MMSE Estimation of Phase Noise, Which Has a Symmetric Levy Distribution and a Possibly Large Magnitude, from Observables Time-Sampled at Irregular Instants," accepted to appear in the *IET Communications*.

2. **Y. Song**, "Decoupled 2D DOA Estimation Using Partly Calibrated Vector Hydrophones," accepted to appear in the *IEEE Transactions on Aerospace & Electronic Systems*.

3. **Y. Song** & K. T. Wong, "Azimuth-Elevation Direction Finding, Using a Microphone and Three Orthogonal Velocity-Sensors as a Noncollocated Subarray," *Journal of the Acoustical Society of America*, vol. 133, no. 4, pp. 1987-1995, April 2013.

4. **Y. Song** & K. T. Wong, "Three Dimensional Localization of a Near-Field Emitter of Unknown Spectrum Using an Acoustic Vector Sensor," *IEEE Transactions on Aerospace & Electronic Systems*, vol. 49, no. 2, pp. 1035-1041, April 2013.

5. **Y. Song** & K. T. Wong, "Lower Bound of Direction-of-Arrival Estimation for Acoustic Vector Sensor with Sensor Breakdown," *IEEE Transactions on Aerospace & Electronic Systems*, vol. 48, no. 4, pp. 3703-3708, October 2012.

6. **Y. Song** & K. T. Wong, "Closed-Form Direction Finding Using Collocated but Orthogonally Oriented Higher-Order Acoustic Sensors," *IEEE Sensors Journal*, vol. 12, no. 8, pp. 2604-2608, August 2012.

7. K. T. Wong, Y. I. Wu, Y.-S. Hsu & **Y. Song**, "A Lower Bound of DOA-Estimates from an Array Randomly Subject to Sensor-Breakdown," *IEEE Sensors Journal*, vol. 12, no. 5, pp. 911-913, May 2012.

8. **Y. Song**, C. C. Fung, K. T. Wong, H. Meng & D.-F. Tseng, "Precoder / Two-Stage Equaliser for Block-Based Single-Carrier Transmission with Insufficient Guard Interval," *Electronics Letters*, vol. 47, no. 13, pp. 746-748, 23 June, 2011.

Journal papers: (under peer review)

1. **Y. Song**, K. T. Wong & F. J. Chen, ""Blind" Calibration of an Array of Acoustic Vector-Sensors Suffering Gain Errors / Mis-Location / Mis-Orientation," under review by the *IEEE Transactions on Signal Processing*.

2. **Y. Song** & K. T. Wong, ""Blind" Calibration of Electromagnetic Vector Sensors Whose Dipole-Triads/Loop-Triads Deviate from Their Nominal Gains / Phases / Orientations / Locations," under review by the *IEEE Transactions on Signal Processing*.

3. **Y. Song**, K. T. Wong & Xin Yuan, "Errata to "Vector Cross-Product Direction-Finding' With an Electromagnetic Vector-Sensor of Six Orthogonally Oriented But Spatially Noncollocating Dipoles/Loops"," under review by the *IEEE Transactions on Signal Processing*.

4. **Y. Song**, K. T. Wong & Yung-Fang Chen, Blind Reception-Beamforming to Null Unknown Interference for Block-Based Single-Carrier Transmission with an Insufficient Guard Interval, under review by the *IEEE Wireless Communications Letters*.

5. **Y. Song** & K. T. Wong, "Acoustic Direction Finding Using a Spatially Spread Tri-Axial Velocity Sensor," under review by the *IEEE Transactions on Aerospace & Electronic Systems*.

Conference papers:

1. **Y. Song**, "Blind Calibration and Remedy for Mis-Orientation Velocity-Sensor Triads," *2013 IEEE International Conference on Acoustics, Speech & Signal Processing (ICASSP)*, Vancouver, Canada, May, 2013.

2. Y. L. Li, **Y. Song**, & K. T. Wong, "Direction Finding Using a Pair of Orthogonally Oriented Velocity/Pressure Sensors," *IEEE TENCON Spring Conference*, Sydney, Australia, April, 2013.

3. C. L. Yung, **Y. Song**, & K. T. Wong, "How Channel Mis-Match Would Degrade the Bit-Error Rate of the Song-Fung-Wong-Meng-Tseng Transceiver Architecture for Block-Based Single-Carrier Transmission," *National Symposium Telecommunications*, Changhua, Taiwan, November, 2012.

4. C. L. Yung, **Y. Song**, & K. T. Wong, "Performance of the Song-Fung-Wong-Meng-Tseng Scheme of Block-Based Single-Carrier Transmission Under Channel Mis-Match," *Conference on Photonics and Communications*, Kaohsiung, Taiwan, 26 October, 2012.

Acknowledgments

My sincere appreciation goes to my chief supervisor Dr. Kainam Thomas Wong, from the bottom of my heart and beyond words. Without the opportunity he provided, it's impossible for me to pursue my doctorate study in PolyU.

During my doctorate study here, Dr. Kainam Thomas Wong inspired me with high-level ideas from time to time, drafted some of my manuscripts, and thoroughly revised the entirety of every one of my research manuscripts with great patience. Without his professional assistance, it's impossible for me to publish research papers in the world's top journals.

I would like to thank Dr. Yue Ivan Wu, Dr. Xin Yuan, Mr. Bo Wang and many other research collaborators for their help to my work since 2009.

Last but not the least, I would like to express my love and gratitude to my beloved parents for their persistent support and endless love.

Contents

List of Figures

List of Tables

Chapter 1

Introduction

[1]

This dissertation presents 8 research projects by the candidate student since September 2009. These 8 research projects may be categorized into two loosely related research areas: Chapters 2-7 describe 6 research projects on space-time signal processing for acoustic sensor arrays. Chapters 8 describe 2 research projects on signal processing for single-carrier block-based transmission/reception.

1.1 The Acoustic *Vector*-Sensor

1.1.1 The Acoustic Particle-*Velocity* Sensor

Customary microphones (monopoles) treat the acoustic wavefield as a space-time field of the pressure scalar. This overlooks information in the underlying acoustic "particle velocity vector" - a three-dimensional vector representing the three partial derivatives of the pressure-field, taken with respect to the three Cartesian spatial coordinates. To measure any one such Cartesian component of this acoustic particle-velocity field vector, needed is an acoustic particle-*velocity* sensor (a dipole) that is oriented along that Cartesian axis.

Acoustic velocity-sensor technology has been used in underwater-acoustics and air-acoustics for over a century [2], and is the subject of recently renewed interest [30], [94]. The acoustic *velocity*-sensor's various hardware implementations are discussed in [56].

1.1.2 The Velocity-Sensor Triad

A velocity-sensor triad (a.k.a. vector-hydrophone) consists of three identical, but orthogonally oriented, acoustic *velocity*-sensors – all spatially co-located in a point-like geometry, see Figure 1.1. The entire velocity-sensor triad thus distinctly measures all three Cartesian components of the particle-velocity vector. The velocity-sensor triad thus treats the acoustic wavefield as a vector-field (i.e., the particle-velocity field), not merely as a scalar

[1] This chapter is taken from the several papers [158, 162, 165, 163, 159, 160] jointly authored by the candidate and his chief supervisor.

field (i.e., pressure-field), as by the customary microphone or hydrophone. More precisely, an acoustic *vector*-sensor (placed at the origin of the three-dimensional Cartesian coordinates) would have this 3×1 array-manifold [26], [59], in response to a unit-power incident acoustic wave that has traveled through an homogeneous isotropic medium:

$$\mathbf{a}(\theta, \phi) \overset{\text{def}}{=} \begin{bmatrix} u(\theta, \phi) \\ v(\theta, \phi) \\ w(\theta) \end{bmatrix} \overset{\text{def}}{=} \begin{bmatrix} \sin\theta \cos\phi \\ \sin\theta \sin\phi \\ \cos\theta \end{bmatrix}, \tag{1.1}$$

where $0 \leq \theta \leq \pi$ symbolizes the elevation-angle measured from the vertical z-axis, $0 \leq \phi < 2\pi$ denotes the azimuth-angle measured from the positive x-axis, $u(\theta, \phi)$ refers to the direction-cosine along the x-axis, $v(\theta, \phi)$ represents the direction-cosine along the y-axis, and $w(\theta)$ refers to the direction-cosine along the z-axis. The first, second, and third components in $\mathbf{a}(\theta, \phi)$ correspond to the acoustic *velocity*-sensors aligned along the x-axis, the y-axis, and the z-axis, respectively. These three components together give a Frobenius norm, $\sqrt{[u(\psi, \phi)]^2 + [v(\psi, \phi)]^2 + [w(\psi)]^2} = 1, \forall \psi, \phi$.

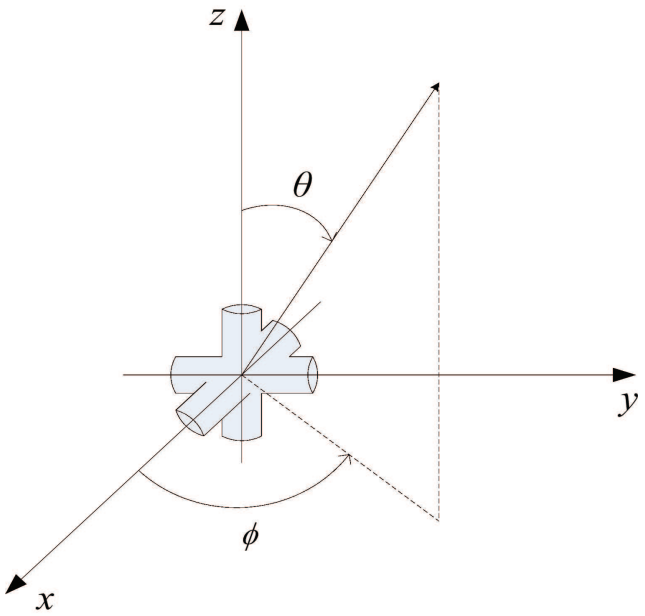

Figure 1.1: A geometric illustration of a velocity-sensor triad.

1.1.3 The Customary Acoustic *Vector*-Sensor: Three Orthogonally Oriented *Velocity*-Sensors Collocating with a Pressure-Sensor

The acoustic *vector*-sensor (a.k.a. vector-hydrophone), consists of three acoustic *velocity*-sensors (identical, but oriented orthogonally, and collocated) plus an acoustic *pressure*-sensor — these four component-sensors together constitute one acoustic *vector*-sensor (a.k.a. a vector-hydrophone). This acoustic *vector*-sensor thus distinctly measures each Cartesian component of the particle-velocity vector plus the pressure scalar, **all at the same point in space**.

Mathematically, for an acoustic *vector*-sensor located at the Cartesian coordinates' origin, it would have the 4×1 array-manifold [26, 59, 135]

$$\mathbf{a}(\theta, \phi) \stackrel{\text{def}}{=} \begin{bmatrix} u(\theta, \phi) \\ v(\theta, \phi) \\ w(\theta) \\ 1 \end{bmatrix} \stackrel{\text{def}}{=} \begin{bmatrix} \sin\theta \cos\phi \\ \sin\theta \sin\phi \\ \cos\theta \\ 1 \end{bmatrix}, \tag{1.2}$$

in response to a unit-power incoming acoustic wave, that has traveled through an homogeneous isotropic medium. The array-manifold's fourth element corresponds to the acoustic *pressure*-sensor. The entire four-element array-manifold always gives a Frobenius norm of $\sqrt{2}$, regardless of ψ and ϕ.

For a literature survey of the acoustic vector-sensor's hardware implementations, sea/air trials and associated direction-finding algorithms, please see [122, 134, 154]. Acoustic vector-sensors are commercially available as the "Uniaxial P-U Probe" from Acoustech.[2]

1.1.4 The Acoustic *Vector*-Sensor's Advantages in Eigen-Based Direction-Finding

The acoustic *vector*-sensor's unique array-manifold is advantageous to eigen-based direction-finding algorithms. It has been exploited using the "Estimation of Signal Parameters via a Rotation Invariance Technique" (ESPRIT) [33, 34, 44, 53, 86, 99, 110, 120, 134], using the "MUltiple SIgnal Classification" (MUSIC) [44, 76, 110, 129, 139, 137], using the Root-MUSIC [40, 124, 140], using the beamspace-based DOA-estimation [35], [69], or using other subspace-based parameter-estimation methods [107, 111, 119, 130, 133, 137, 141, 149, 154]. The acoustic *vector*-sensor has also been used for source-tracking [51, 88, 109, 119, 139, 150].

The above eigen-based algorithms eigen-decompose the space-time data-correlation matrix, to estimate each incident source's steering vector $\mathbf{a}$ as $\hat{\mathbf{a}} = c\mathbf{a}$, to within an unknown complex-value scalar c. *Normalize* $\hat{\mathbf{a}}$ to give $\sqrt{2}\frac{\hat{\mathbf{a}}}{\|\hat{\mathbf{a}}\|}$, of which the top three elements will be *un*ambiguous estimates of the three Cartesian direction-cosines $u(\theta, \phi)$, $v(\theta, \phi)$, and $w(\theta)$. Direction finding is thereby achieved, despite the unknown complex-value c mentioned above.

It is important to recognize that the above "self normalization" approach of direction-finding is predicated on both

{i} a unity Frobenius norm for the first three components of the array manifold regardless of the arrival-angles of θ and ϕ, and

{ii} a unity value for the fourth component regardless of the arrival-angles of θ and ϕ.

This acoustic *vector*-sensor "self-normalization" direction-finding is advantageous in the following ways:

[2] http://www.acoustechcorporation.com (date last viewed 6/1/12)

{1} A four-component acoustic vector-sensor exploits information in the acoustic-particle-velocity vector-field, in addition to the information in the pressure scalar-field.

{2} Multiple incident sources' azimuth-angles and the elevation-angles may be estimated and automatically matched, using only one acoustic vector-sensor [53, 51, 134].

{3} This self-normalization direction-finding approach may be creatively synergized with the customary interferometry direction-finding approach (which estimates the spatial phase delay among the data sets collected at physically displaced antennas) to offer unusual capabilities:

(a) Direction-of-arrival estimation accuracy can be improved by orders of magnitude with*out* requiring additional microphones or hydrophones. [34]

(b) Direction-of-arrival estimation can be achieved with*out* prior knowledge/estimation of the nominal/actual geometric array-grid and without any calibration-source, thereby adding unprecedented "real-world" deployment. [33]

(c) No prior coarse estimates is needed to initiate the MUSIC (MUltiple SIgnal Classification) iterative parameter-estimation routine. Instead MUSIC can now self-initiates its iteration. [44]

(d) Blind geolocation, beamforming, and interference-rejection are possible for frequency-hopping sources of unknown and arbitrary hop-sequences and directions-of-arrival. [134]

Chapter 2

Closed-Form Direction-Finding Using Collocated but Orthogonally Oriented Higher-Order Acoustic Sensors

[1]

2.1 Literature Review of *Higher*-Order Acoustic Sensor

2.1.1 The Acoustic Velocity-Sensor – *First*-Order Spatial Derivative of the Acoustic Pressure-Field

Each Cartesian component of the acoustic *particle-velocity* field vector represents a *first*-order spatial derivative of the pressure-field along that Cartesian coordinate, and may be directly measured (with*out* computing any spatial derivative) by a velocity-sensor aligned in parallel to that Cartesian coordinate.

2.1.2 Directional Acoustic Sensors that Measure a *Higher*-Order Spatial Derivative of the Acoustic Pressure-Field

While the acoustic *velocity*-sensor measures a *first*-order spatial derivative of the incident pressure-field, the *second*-order and higher-order spatial derivatives of the pressure-field could likewise be defined. Second-order and higher-order acoustic sensors have in fact been implemented directly, with*out* computing any derivative of the data collected by lower-order sensors:

{i} The second-order dipole-mode (a.k.a cosine beampattern) acoustic sensors are implemented by piezoelectric rings in [43] and by piezoelectric hollow cylinders in [65].

[1] This chapter is taken from [158], jointly authored by the candidate and his chief supervisor.

{ii} The third-order quadrupole-mode (a.k.a cosine-squared beampattern) acoustic sensors are implemented by piezoelectric rings in [43], by piezoelectric hollow cylinders in [65], and by the wagon-wheel transducer in [74].

{iii} The fourth-order acoustic sensors are implemented by the wagon-wheel transducer in piezoelectric hollow cylinders in [65].

{iv} Arbitrarily higher-order acoustic sensors are implemented by a"piezoelectric ceramic spherical shell whose surface is sectionally electroded" in [4], and by the spherical radiator in [6].

Indeed, the directivity and the beam-patterns of higher-order directional sensors have been investigated in [1, 3, 5, 8, 9, 36, 42, 52, 60, 105, 100, 128]. Moreover, [106] derives the Cramér-Rao bounds (in open form) for direction finding using such higher-order directional sensors.

No closed-form direction-finding *algorithm* is yet available in the open literature for such higher-order acoustic sensors, however. The present work fills this literature gap. Subsequently listed are closed-form direction-finding formulas for various compositions of collocated higher-order acoustic vector-sensors. Their corresponding validity-regions are also identified for *unambiguous* estimation of the direction-of-arrival. These new results will allow high-order directional acoustic sensors to be straight-forwardly adopted in the direction-finding methods cited in [122, 134, 154]. For example, the subsequently derived (2.4)-(2.6) or (2.11)-(2.13) may directly substitute for the direction-cosine estimation equations (15)-(17) in [53]. These new results will retain the many advantages in those earlier direction-finding methods.

2.2 Measurement Model of the Generalized Acoustic Vector-Sensor Consisting of Higher-Order Directional Acoustic Sensors

The kth-order acoustical sensor has a gain-pattern[2] of $\cos^k \gamma$, where γ refers to the angle between the directional sensor's orientation and the incident source's direction-of-arrival. (Please see p. 1232 of [105].)

For a directional acoustical sensor aligned along the x-axis, its (θ, ϕ) directivity may be obtained by considering a position-vector of (θ, ϕ, r) in the spherical coordinates of Figure 2.1. A unit-length position-vector would give a length of $\sin(\theta)\cos(\phi) = \cos\gamma$, when projected along the x-axis. Hence, this x-axis aligned kth-order directional acoustical sensor has a directivity of $[\cos\gamma]^k = [\sin(\theta)\cos(\phi)]^k$. Likewise, a kth-order directional acoustical sensor has a directivity of $[\cos\eta]^k = [\sin(\theta)\sin(\phi)]^k$, if aligned along the y-axis. Similarly, a kth-order directional acoustical sensor, if aligned along the z-axis, has a

[2] The gain-pattern here refers to the sensor's registered voltage as a function of the incident source's γ.

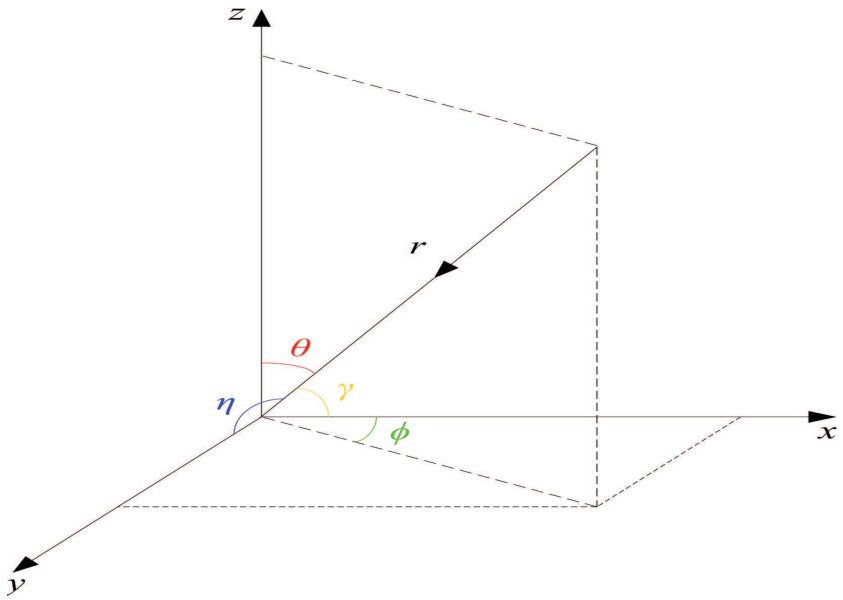

Figure 2.1: Inter-relation among the various spatial angles.

directivity of $[\cos\theta]^k$. These give the 3×1 generalized array manifold,

$$\mathbf{a}^{(k_x,k_y,k_z,\times)} = \begin{bmatrix} \{\sin(\theta)\cos(\phi)\}^{k_x} \\ \{\sin(\theta)\sin(\phi)\}^{k_y} \\ \{\cos(\theta)\}^{k_z} \end{bmatrix} = \begin{bmatrix} u^{k_x} \\ v^{k_y} \\ w^{k_z} \end{bmatrix}. \tag{2.1}$$

With the addition of a pressure-sensor, the generalized array manifold becomes 4×1:

$$\mathbf{a}^{(k_x,k_y,k_z,\surd)} = \begin{bmatrix} \{\sin(\theta)\cos(\phi)\}^{k_x} \\ \{\sin(\theta)\sin(\phi)\}^{k_y} \\ \{\cos(\theta)\}^{k_z} \\ 1 \end{bmatrix} = \begin{bmatrix} u^{k_x} \\ v^{k_y} \\ w^{k_z} \\ 1 \end{bmatrix}. \tag{2.2}$$

The $\times$ ($\surd$) symbol in the superscript refers to the absence (presence) of a pressure-sensor in the acoustic vector-sensor.

Numerous eigenstructure-based (i.e., subspace-based) direction-finding schemes exploit the unique array manifolds of directional acoustic sensors (i.e., acoustic particle-velocity sensors) that measure the *first*-order spatial derivative of the incident pressure-field. [3] This section will show that a general kth-order acoustic sensor can be used in all above-mentioned subspace-based direction-finding schemes, in replacement of *first*-order directional sensors.

All aforementioned eigenstructure-based parameter-estimation algorithm involve an intermediate step that estimates each incident source's steering vector, but correct to only within an *unknown* complex-value scalar c. That is, available from each algorithm is the

[3] For literature surveys, please see [122, 134, 154].

estimate,

$$\hat{\mathbf{a}} \stackrel{\text{def}}{=} \begin{cases} \begin{bmatrix} \hat{a}_x \\ \hat{a}_y \\ \hat{a}_z \\ \hat{a}_p \end{bmatrix} \approx c\, \mathbf{a}^{(k_x,k_y,k_z,\surd)}, & \text{if the pressure-sensor is present,} \\ \begin{bmatrix} \hat{a}_x \\ \hat{a}_y \\ \hat{a}_z \end{bmatrix} \approx c\, \mathbf{a}^{(k_x,k_y,k_z,\times)}, & \text{if the pressure-sensor is absent.} \end{cases} \tag{2.3}$$

The approximation becomes a straight equality in noiseless or asymptotic cases.

The issue here is whether $\hat{\mathbf{a}}$ suffices to unambiguously estimate the source's azimuth-elevation arrival-angles, despite that c is not prior known. The next two sections will answer in the affirmative.

2.3 Closed-Form Estimation-Formulas With a Pressure-Sensor

A key insight is that $\left[\mathbf{a}^{(k_x,k_y,k_z,\surd)}\right]_4 = 1, \forall\theta,\phi$ and $\forall k_x, k_y, k_z$. Further examination of (2.1) reveals that

$$\begin{aligned} |u| &= \left| \left[\mathbf{a}^{(k_x,k_y,k_z,\surd)}\right]_1^{\frac{1}{k_x}} \right| \\ |v| &= \left| \left[\mathbf{a}^{(k_x,k_y,k_z,\surd)}\right]_2^{\frac{1}{k_y}} \right| \\ |w| &= \left| \left[\mathbf{a}^{(k_x,k_y,k_z,\surd)}\right]_3^{\frac{1}{k_z}} \right|. \end{aligned}$$

All these lead to

$$\begin{aligned} |\hat{u}| &= \left| \frac{\hat{a}_x}{\hat{a}_p}^{\frac{1}{k_x}} \right| \\ |\hat{v}| &= \left| \frac{\hat{a}_y}{\hat{a}_p}^{\frac{1}{k_y}} \right| \\ |\hat{w}| &= \left| \frac{\hat{a}_z}{\hat{a}_p}^{\frac{1}{k_z}} \right|. \end{aligned}$$

The only remaining task is to determine the sign of these three direction-cosines. If a particular direction-cosine's order is odd, then its sign equals the sign of $\Re\left(\frac{\hat{a}_x}{\hat{a}_p}\right)$, where $\Re$ refers to the real part of the entity inside the parentheses. If a particular direction-cosine's order is even, needed will be a prior knowledge of the direction-cosine's sign.

In summary,

$$\hat{u} = \begin{cases} \left| \left(\frac{\hat{a}_x}{\hat{a}_p}\right)^{\frac{1}{k_x}} \right| \operatorname{sign}\left(\Re\left(\frac{\hat{a}_x}{\hat{a}_p}\right)\right), & \text{if } k_x \text{ is odd} \\ \left| \left(\frac{\hat{a}_x}{\hat{a}_p}\right)^{\frac{1}{k_x}} \right| \operatorname{sign}(u), & \text{if } k_x \text{ is even} \end{cases} \tag{2.4}$$

$$\hat{v} = \begin{cases} \left| \left(\frac{\hat{a}_y}{\hat{a}_p}\right)^{\frac{1}{k_y}} \right| \operatorname{sign}\left(\Re\left(\frac{\hat{a}_y}{\hat{a}_p}\right)\right), & \text{if } k_y \text{ is odd} \\ \left| \left(\frac{\hat{a}_y}{\hat{a}_p}\right)^{\frac{1}{k_y}} \right| \operatorname{sign}(v), & \text{if } k_y \text{ is even} \end{cases} \tag{2.5}$$

$$\hat{w} = \begin{cases} \left| \left(\frac{\hat{a}_z}{\hat{a}_p}\right)^{\frac{1}{k_z}} \right| \operatorname{sign}\left(\Re\left(\frac{\hat{a}_z}{\hat{a}_p}\right)\right), & \text{if } k_z \text{ is odd} \\ \left| \left(\frac{\hat{a}_z}{\hat{a}_p}\right)^{\frac{1}{k_z}} \right| \operatorname{sign}(w), & \text{if } k_z \text{ is even.} \end{cases} \tag{2.6}$$

Iff k_x is even, the above estimates would require prior knowledge of the sign of u. Iff k_y is even, the above estimates would require prior knowledge of the sign of v. Iff k_z is even, the above estimates would require prior knowledge of the sign of w.

Hence, *un*ambiguous would be the azimuth-elevation direction-of-arrival estimation, with a validity-region over the entire spherical coordinates, if and only if k_x, k_y, k_z are all odd. If exactly one of k_x, k_y, k_z is even, then the unambiguous estimation's validity-region would be halved to only an hemisphere round the vector-sensor. For each additional even entity among k_x, k_y, k_z, the unambiguous estimation's validity-region would be further halved.

Then, θ and ϕ may be estimated as

$$\hat{\theta} = \arccos \hat{w} \tag{2.7}$$

$$\hat{\phi} = \operatorname{sign}(\hat{v}) \arccos\left\{\frac{\hat{u}}{\sin(\hat{\theta})}\right\}. \tag{2.8}$$

2.4 Closed-Form Estimation-Formulas With*out* any Pressure-Sensor

Without any pressure-sensor in the acoustic vector-sensor, the unknown complex number c cannot be determined as in Section 2.3. However, as $u^2 + v^2 + w^2 = 1, \forall \theta, \phi$, it holds that

$$\left| \left(\frac{\hat{a}_x}{c}\right)^{\frac{2}{k_x}} \right| + \left| \left(\frac{\hat{a}_y}{c}\right)^{\frac{2}{k_y}} \right| + \left| \left(\frac{\hat{a}_z}{c}\right)^{\frac{2}{k_z}} \right| = 1. \tag{2.9}$$

Hence, $|c|$ may be estimated by solving the above polynomial in (2.9). Then,

$$\hat{\angle} c = \begin{cases} \angle \hat{a}_\xi, & \text{if } \zeta^{k_\xi} > 0 \\ -\angle \hat{a}_\xi, & \text{if } \zeta^{k_\xi} < 0, \end{cases} \tag{2.10}$$

where $\zeta = u$ if $\xi = x$, $\zeta = v$ if $\xi = y$, and $\zeta = w$ if $\xi = z$. The sign of ζ is a priori unknown. However, ζ^{k_ξ} may be set as positive, if k_ξ is even. Otherwise, a prior knowledge of the

sign of ζ would be required. Algebraic manipulations then give

$$\hat{c} \;=\; \begin{cases} |c|e^{j\angle \hat{a}_\xi}, & \text{if } k_\xi \text{ is even} \\ |c|e^{j\angle \hat{a}_\xi}, & \text{if } k_x, k_y, k_z \text{ are all odd and if } \zeta > 0 \\ |c|e^{j\angle(-\hat{a}_\xi)}, & \text{if } k_x, k_y, k_z \text{ are all odd and if } \zeta < 0 \end{cases}$$

Further algebraic manipulations give

$$\hat{u} \;=\; \begin{cases} \left|\left(\frac{\hat{a}_x}{\hat{c}}\right)^{\frac{1}{k_x}}\right| \operatorname{sign}\left(\Re\left(\frac{\hat{a}_x}{\hat{c}}\right)\right), & \text{if } k_x \text{ is odd} \\ \left|\left(\frac{\hat{a}_x}{\hat{c}}\right)^{\frac{1}{k_x}}\right| \operatorname{sign}(u), & \text{if } k_x \text{ is even} \end{cases} \tag{2.11}$$

$$\hat{v} \;=\; \begin{cases} \left|\left(\frac{\hat{a}_y}{\hat{c}}\right)^{\frac{1}{k_y}}\right| \operatorname{sign}\left(\Re\left(\frac{\hat{a}_y}{\hat{c}}\right)\right), & \text{if } k_y \text{ is odd} \\ \left|\left(\frac{\hat{a}_y}{\hat{c}}\right)^{\frac{1}{k_y}}\right| \operatorname{sign}(v), & \text{if } k_y \text{ is even} \end{cases} \tag{2.12}$$

$$\hat{w} \;=\; \begin{cases} \left|\left(\frac{\hat{a}_z}{\hat{c}}\right)^{\frac{1}{k_z}}\right| \operatorname{sign}\left(\Re\left(\frac{\hat{a}_z}{\hat{c}}\right)\right), & \text{if } k_z \text{ is odd} \\ \left|\left(\frac{\hat{a}_z}{\hat{c}}\right)^{\frac{1}{k_z}}\right| \operatorname{sign}(w), & \text{if } k_z \text{ is even.} \end{cases} \tag{2.13}$$

Unambiguous estimation for the azimuth-elevation angle-of-arrival, over the entire sphere around the vector-sensor, would be impossible without the pressure-sensor. Even if k_x, k_y, k_z are all odd, $\hat{\angle} c$ in (2.10) would still require prior information that reduces the unambiguous validity-region to an hemisphere. If exactly one of k_x, k_y, k_z is even, the unambiguous validity-region would remain at an hemisphere, because prior information would become necessary in (2.11)-(2.13) whereas $\hat{\angle} c$ in (2.10) would need no prior information. For each additional k_x, k_y, k_z is also even, the unambiguous validity-region would be further halved once again.

Then, θ and ϕ may be estimated as in (2.7) and (2.8) of Section 2.3.

2.5 How the Sensor-Order Affects Estimation Accuracy

Consider a k_zth-order sensor oriented along the z-axis. Its gain-pattern equals $\cos^{k_z}(\theta)$. Figure 2.2 shows the sensor's sensitivity to θ, at various θ values and for $k_z = 1, 3, 5, 7$. Where θ satisfies $\frac{d\cos^{k_z}(\theta)}{d\theta} \geq \frac{d\cos(\theta)}{d\theta}$ (i.e. $\cos^{k_z-1}(\theta) \geq \frac{1}{k_z}$, shown by solid curve-segments in Figure 2.2), the k_zth-order sensor is more sensitive to θ than a first-order sensor would. As k_z increases, the inequality would be satisfied by a narrower range of θ. Also,as k_z increases, $\frac{d\cos^{k_z}(\theta)}{d\theta}$ will increase within this θ-range, implying greater sensitivity to θ.

Similarly for the x-axis sensor, $\cos^{k_x-1}(\gamma) \geq \frac{1}{k_x}$, the resolution of $\gamma = \arccos(\sin\theta\cos\phi$ will be improved by $k_x > 1$.

Furthermore, for the y-axis sensor, if $\cos^{k_y-1}(\eta) \geq \frac{1}{k_y}$, the resolution of $\eta = \arccos(\sin\theta\sin\phi)$ will be improved by $k_y > 1$.

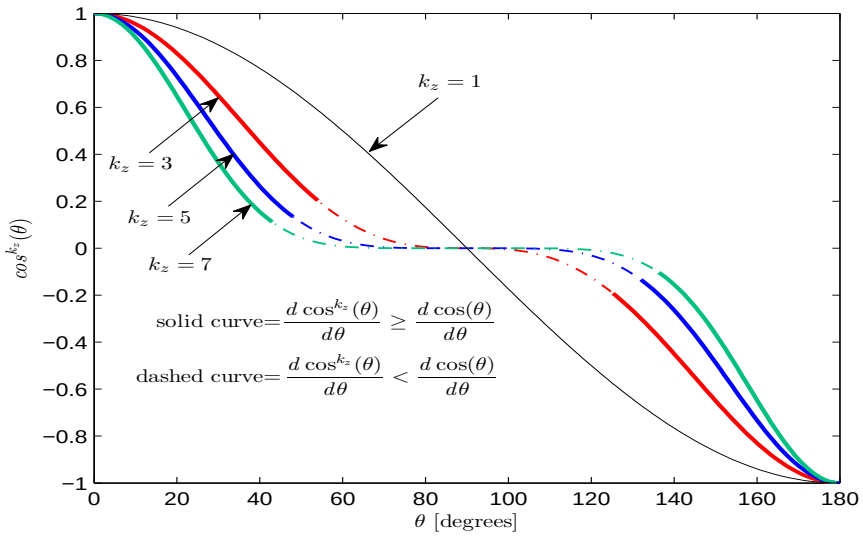

Figure 2.2: The range of θ where the k_zth-order sensor will be more sensitive to θ than the first-order sensor would be.

2.6 Summary

For three *higher-order* acoustic sensors orthogonally oriented in a collocated with an optional pressure-sensor, this chapter presents the azimuth-elevation direction-finding formulas in closed form. The three sensors may have arbitrarily different orders among themselves. Unambiguous azimuth-elevation angle-of-arrival over the entire sphere is possible iff the pressure-sensor is present and all higher-order sensors are of odd orders.

Chapter 3

Azimuth-Elevation Direction Finding Using a Microphone and Three Orthogonal Velocity Sensors as a Non-collocated Subarray

[1]

3.1 This Work's Contributions

The direction-of-arrival estimation precision of a sensor-array depends on the spatial extent of the array aperture. The larger the aperture is, the finer the sensor-array's resolution will be for the direction-of-arrival. Unfortunately, the acoustic vector-sensor's spatial *collocation* gives a point-like aperture in space. While this spatial collocation simplifies the mathematics governing the acoustic vector-sensor's array manifold, thereby making possible the "self-normalization" approach of direction finding, it would be useful if the aperture may be enlarged without increasing the number of component-sensors, while retaining the full advantages of $\{1\} - \{3\}$ in Section 1.1.4. Moreover, *hardware*-wise, it could be difficult and costly to physically collocate (or co-center) the four component-sensors all *exactly* at one point in space. This work will show how to displace the four component-sensors, while still retaining the aforementioned *algorithmic* advantages.

This contribution is nontrivial, as *spatially spread* particle-velocity sensors suffer phase-shifts among them, due to their displacements. Therefore, the array-manifold of (1.2) would become inapplicable, and the "self-normalization" direction-finding approach would apparently be inapplicable. Nonetheless, this chapter succeeds in advancing a class of new closed-form direction-finding algorithms applicable even when the four component-sensors spread out arbitrarily in the three-dimensional space.

Besides retaining advantages {1} - {3} in Section 1.1.4, the presently proposed new

[1] This chapter is taken from [162], jointly authored by the candidate and his chief supervisor.

class of algorithms *also* provide these additional advantages:

{4} The spatial resolution is enhanced over the azimuth/elevation, because the four component-sensors now extend over a larger spatial aperture (instead of co-centered at one point). That is, the present scheme spatially extends the geometric aperture, but requires *no* additional component-sensor.

{5} Hardware can be simplified, as the four component-sensors need no longer be collocated, thereby reducing the hardware cost.

The remainder of this chapter is as follows: The new approach will be developed first for a simple array-geometry in Section 3.2, as an illustrative case. For the general case of an *arbitrary* array-configuration of spatially spread particle-velocity sensors and pressure sensor, the new approach will be fully developed in Section 3.3. Section 3.4 will show how to adopt this new scheme to an eigen-based parameter-estimation algorithm, in the case of *one* acoustic vector-sensor, using [53] as a concrete example. Section 3.5 will do the same, but for the case of *multiple* acoustic vector-sensors, using [33] as a concrete example. Monte Carlo simulations there will verify the proposed scheme's efficacy in direction finding, despite the spatial non-collocation and the extended aperture of the acoustic vector-sensor. Section 4.6 will conclude the chapter.

3.2 The New Approach – for a Particularly Simple Array Configuration, as Illustration

The proposed algorithmic approach allows all four component-sensors to be *arbitrarily located and arbitrarily oriented*. Nonetheless for pedagogical reasons, a particularly simple array-configuration (shown in Figure 3.1) will first be discussed here in this section, to illustrate the proposed algorithmic philosophy. The arbitrarily general array-configuration will be discussed in details in Section 3.3.

3.2.1 The Array Manifold for a Particular Array-Configuration in Figure 3.1

Referring to the sample array-configuration in Figure 3.1: The pressure sensor lies at the Cartesian origin. The x-axis *oriented* particle-velocity sensor lies on the x-axis, at a distance of Δ_{px} from the Cartesian origin. The y-axis *oriented* particle-velocity sensor lies on the y-axis, at a distance of Δ_{py} from the Cartesian origin. The z-axis *oriented* particle-velocity sensor lies on the z-axis, at a distance of Δ_{pz} from the Cartesian origin. Here, Δ_{px}, Δ_{py}, or Δ_{pz} may each be positive or negative. Figure 3.1 illustrates one special case where $\Delta_{px} > 0$, $\Delta_{py} > 0$, and $\Delta_{pz} > 0$. There in the figure, the particle-velocity sensors oriented along the x-axis, y-axis, and z-axis are identified respectively as V_x, V_y, and V_z, and the pressure sensor as P.

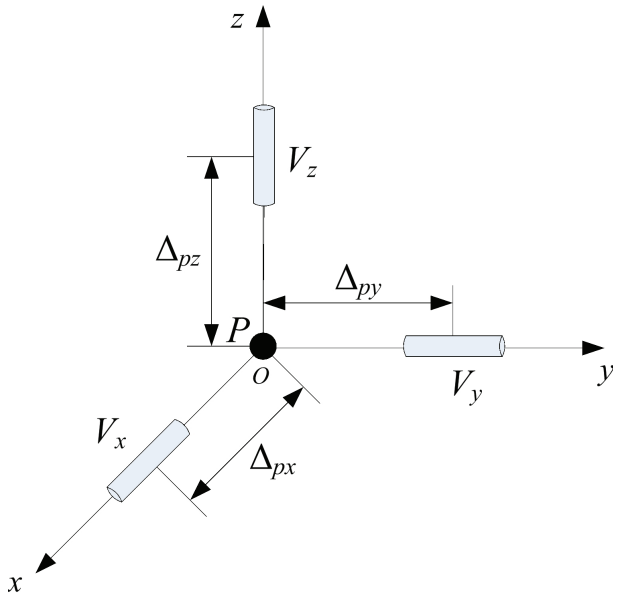

Figure 3.1: The "pyramid-like" array configuration with four component-sensors. Illustrated here is the special case of $\Delta_{px} > 0$, $\Delta_{py} > 0$, and $\Delta_{pz} > 0$.

This *spatially distributed* array-configuration's array-manifold differs from the *spatially collocated* array-manifold in (1.2), but equals

$$\mathbf{a}_{\text{pyramid}} \quad = \quad \begin{bmatrix} u\ e^{j\frac{2\pi}{\lambda}\Delta_{px}u} \\ v\ e^{j\frac{2\pi}{\lambda}\Delta_{py}v} \\ w\ e^{j\frac{2\pi}{\lambda}\Delta_{pz}w} \\ 1 \end{bmatrix}. \tag{3.1}$$

This new array-manifold in (3.1) now depends on the incident signal's frequency; and the Cartesian direction cosines now appear in the phases, in addition to the magnitudes in (1.2). The presence of $u(\theta, \phi)$, $v(\theta, \phi)$, $w(\theta)$ in the magnitudes (not in the phases) of this array manifold's entries allows *un*ambiguous direction finding over the entire spherical surface spanned by $\theta \in [0, \pi]$ and $\phi \in [0, 2\pi)$, as will be shown in Section 7.15. This array configuration is "simple" relative to the more general arbitrarily spaced configuration to be introduced in Section 3.3, in that the first three entries here in (3.1) each depends on only one of the three Cartesian direction cosines u, v, w.

3.2.2 A New Direction-Finding Algorithm for a Particular Array-Configuration in Figure 3.1

Eigen-decompose the space-time correlation matrix of the data collected by the four component-sensors. Then obtainable, for each incident source, is the steering-vector estimate[2]

$$\hat{\mathbf{a}} \quad \approx \quad [p_x, p_y, p_z, p_p]^T \quad \stackrel{\text{def}}{=} \quad c\ \mathbf{a}_{\text{pyramid}}. \tag{3.2}$$

[2]This would not limit this proposed scheme to only one incident source.

where the superscript ^{T} denotes transposition. This steering-vector estimate $\hat{\mathbf{a}}$ is correct with regard to the true value $\mathbf{a}_{\text{pyramid}}$ to within an unknown complex-value constant c. With a noiseless condition or with an infinite number of snapshots, the above approximation becomes equality. To simplify the subsequent exposition, the following development will write all such approximations as equalities.

Normalize the first component of (3.2) by the fourth component, thereby giving

$$\frac{p_x}{p_p} \;=\; u\, e^{j\frac{2\pi}{\lambda}(\Delta_{px}u)}. \tag{3.3}$$

From (3.3), two complementary estimators of u are obtainable:

{i} An one-to-many relationship exists between $e^{j2\pi\frac{\Delta_{px}}{\lambda}u}$ and $u \in [-1,1]$, for the extended aperture case of $\frac{\Delta_{px}}{\lambda} > \frac{1}{2}$. Hence,

$$\hat{u}_{\text{phs}} \;=\; \frac{1}{2\pi}\frac{\lambda}{\Delta_{px}}\angle\frac{p_x}{p_p} \;=\; m\frac{\lambda}{\Delta_{px}} + u \tag{3.4}$$

can estimate u, but ambiguously to within some (unknown) integer multiple ($m\times$) of the frequency-*dependent* entity of $\pm\frac{\lambda}{\Delta_{px}}$, where m refers to a to-be-determined integer.

{ii} The frequency-*in*dependent entity

$$\hat{u}_{\text{mag}} \;=\; \left|\frac{p_x}{p_p}\right| \;=\; \pm u \tag{3.5}$$

can estimate u, but also ambiguously, to within a $\pm$ sign.

These two estimates, $\hat{u}_{\text{phs}}$ and $\hat{u}_{\text{mag}}$, can disambiguate each other as follows:

{a} If $\hat{u}_{\text{mag}} = u$, the cyclic ambiguity may be resolved by

$$\hat{m}_u^+ \;\stackrel{\text{def}}{=}\; \arg\min_m \underbrace{\left|\left\{\left(m\frac{\lambda}{\Delta_{px}} + \overbrace{\frac{1}{2\pi}\frac{\lambda}{\Delta_{px}}\angle\frac{p_x}{p_p}}^{=\hat{u}_{\text{phs}}}\right) - \overbrace{\left|\frac{p_x}{p_p}\right|}^{=\hat{u}_{\text{mag}}}\right\}\right|}_{\stackrel{\text{def}}{=}\epsilon_u^+(m)} \tag{3.6}$$

{b} If $\hat{u}_{mag} = -u$, the cyclic ambiguity may then be resolved by

$$\hat{m}_u^- \;\stackrel{\text{def}}{=}\; \arg\min_m \underbrace{\left|\left\{\left(m\frac{\lambda}{\Delta_{px}} + \overbrace{\frac{1}{2\pi}\frac{\lambda}{\Delta_{px}}\angle\frac{-p_x}{p_p}}^{=\hat{u}_{\text{phs}}}\right) - \overbrace{-\left|\frac{p_x}{p_p}\right|}^{=\hat{u}_{\text{mag}}}\right\}\right|}_{\stackrel{\text{def}}{=}\epsilon_u^-(m)} \tag{3.7}$$

{c} To decide between $\hat{u}_{mag} = u$ versus $\hat{u}_{mag} = -u$: Choose $\hat{u}_{mag} = u$, if $\epsilon_u^+(\hat{m}_u^+) < \epsilon_u^-(\hat{m}_u^-)$. Choose $\hat{u}_{mag} = -u$, if $\epsilon_u^+(\hat{m}_u^+) \geq \epsilon_u^-(\hat{m}_u^-)$.

{d} Hence, u can now be *un*ambiguously estimated as

$$\hat{u} \;=\; \begin{cases} \left(\hat{m}_u^+ + \frac{1}{2\pi}\angle\frac{p_x}{p_p}\right)\frac{\lambda}{\Delta_{px}}, & \text{if } \epsilon_u^+(\hat{m}_u^+) < \epsilon_u^-(\hat{m}_u^-). \\ \left(\hat{m}_u^- - \frac{1}{2\pi}\angle\frac{p_x}{p_p}\right)\frac{\lambda}{\Delta_{px}}, & \text{if } \epsilon_u^+(\hat{m}_u^+) \geq \epsilon_u^-(\hat{m}_u^-). \end{cases} \tag{3.8}$$

The estimates, $\hat{v}$ and $\hat{w}$, may be obtained similarly as for $\hat{u}$ via (3.3)-(3.8).

Finally, $\hat{u}$, $\hat{v}$, $\hat{w}$ together give the angle-of-arrival estimates,

$$\hat{\theta} \;=\; \arccos\hat{w}, \tag{3.9}$$

$$\hat{\phi} \;=\; \begin{cases} -\arccos\left(\frac{\hat{u}}{\sin(\hat{\theta})}\right), & \text{if } \frac{\hat{v}}{\sin(\hat{\theta})} < 0 \\ \arccos\left(\frac{\hat{u}}{\sin(\hat{\theta})}\right), & \text{if } \frac{\hat{v}}{\sin(\hat{\theta})} \geq 0. \end{cases} \tag{3.10}$$

This arrival-angle estimates enjoy a support-region over the entire spherical space spanning $\theta \in [0, \pi)$ and $\phi \in (-\pi, \pi]$. Hence, direction finding is achieved *un*ambiguously, despite the four component-sensors' non-collocation and despite their sparse spacings.

Because this "simple" array-configuration in (3.1) has its first three entries each dependent on only one of the three Cartesian direction cosines u, v, w, only one sign-ambiguity needs be disambiguated above for each velocity-sensor. In contrast, an arbitrarily spaced array-configuration (to be introduced in Section 3.3) would be shown to require all three sign-ambiguities be handled for each velocity-sensor.

3.3 The New Scheme for the General *Arbitrary* Array-Configuration

This section will show how the algorithmic philosophy in Section 3.2 can apply to the arbitrarily *general* array-configuration of Figure 3.2.

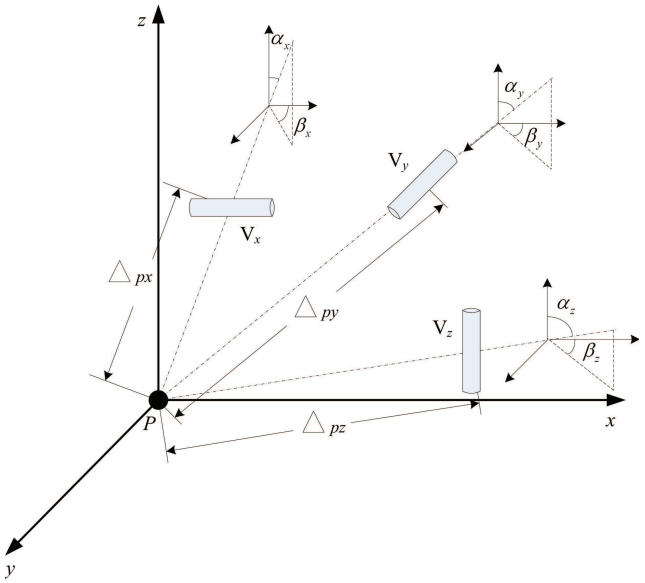

Figure 3.2: The acoustic vector-sensor's four component-sensors spaced arbitrarily in the three-dimensional space.

3.3.1 The Array Manifold for the General Array-Configuration in Figure 3.2

Let the pressure sensor be located again at the origin of the spherical coordinates, without loss of generality. However, allow the three orthogonally oriented particle-velocity sensors be placed *arbitrarily* in three-dimensional space.

For this general configuration of a spatially distributed acoustic vector-sensor, its 4×1 array-manifold equals

$$\mathbf{a}_{\text{gen}}(\theta, \phi) \quad = \quad \begin{bmatrix} u\ e^{j\frac{2\pi}{\lambda}[\Delta_{px}\sin\alpha_x\cos\beta_x u + \Delta_{px}\sin\alpha_x\sin\beta_x v + \Delta_{px}\cos\alpha_x w]} \\ v\ e^{j\frac{2\pi}{\lambda}[\Delta_{py}\sin\alpha_y\cos\beta_y u + \Delta_{py}\sin\alpha_y\sin\beta_y v + \Delta_{py}\cos\alpha_y w]} \\ w\ e^{j\frac{2\pi}{\lambda}[\Delta_{pz}\sin\alpha_z\cos\beta_z u + \Delta_{pz}\sin\alpha_z\sin\beta_z v + \Delta_{pz}\cos\alpha_z w]} \\ 1 \end{bmatrix}. \qquad (3.11)$$

For the new symbols introduced in (3.12), please refer to Figure 3.2 for their definitions.

3.3.2 A New Direction-Finding Algorithm for the General Array-Configuration in Figure 3.2

Eigen-decompose the space-time data-correlation matrix of the data collected by the four component-sensors. Then, obtainable is the steering-vector estimate $\hat{\mathbf{a}}$ for each incident source, where

$$\hat{\mathbf{a}} \quad \approx \quad [p_x, p_y, p_z, p_p]^T \quad \stackrel{\text{def}}{=} \quad c\ \mathbf{a}_{\text{gen}}. \qquad (3.12)$$

Normalize each of the first three components of (3.12) by the fourth component, thereby producing

$$\frac{p_x}{p_p} \quad = \quad u\ e^{j\frac{2\pi}{\lambda}\Delta_{px}h_x}, \qquad (3.13)$$

$$\frac{p_y}{p_p} \quad = \quad v\ e^{j\frac{2\pi}{\lambda}\Delta_{py}h_y}, \qquad (3.14)$$

$$\frac{p_z}{p_p} \quad = \quad w\ e^{j\frac{2\pi}{\lambda}\Delta_{pz}h_z}, \qquad (3.15)$$

where

$$h_x \quad = \quad u\sin(\alpha_x)\cos(\beta_x) + v\sin(\alpha_x)\sin(\beta_x) + w\cos(\alpha_x), \qquad (3.16)$$

$$h_y \quad = \quad u\sin(\alpha_y)\cos(\beta_y) + v\sin(\alpha_y)\sin(\beta_y) + w\cos(\alpha_y), \qquad (3.17)$$

$$h_z \quad = \quad u\sin(\alpha_z)\cos(\beta_z) + v\sin(\alpha_z)\sin(\beta_z) + w\cos(\alpha_z) \qquad (3.18)$$

represent the direction-cosines obtained by projecting the propagation directional vector onto the axes on which Δ_{px}, Δ_{py}, Δ_{pz} respectively lie. These non-Cartesian direction-cosines (h_x, h_y, h_z) are counterpart to the Cartesian direction-cosines (u, v, w) in the earlier Section 3.2, where the three particle-velocity sensors are located on the three Cartesian axes.

The next Section 3.3.2) will explain how to estimate h_x, h_y, h_z, from which Section 3.3.2) will show how to estimate u, v, w.

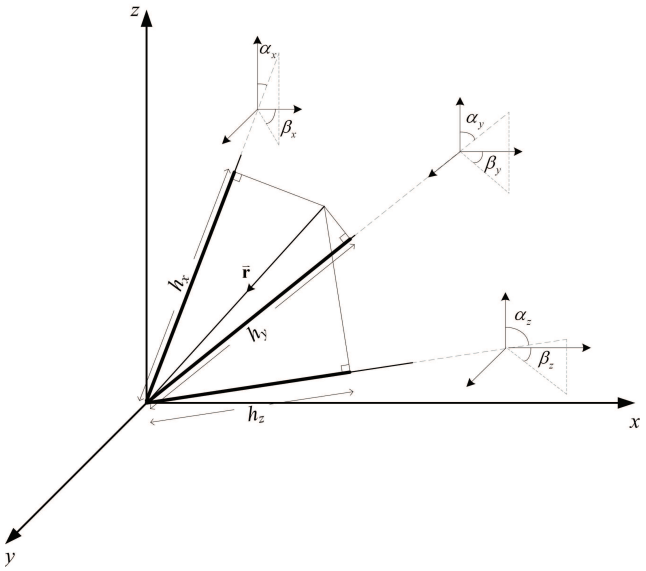

Figure 3.3: Geometric illustration of h_x, h_y and h_z.

To Estimate the Non-Cartesian Direction-Cosines, h_x, h_y, h_z

Consider first the estimation of h_x.

From (3.13), two complementary estimators of h_x can be obtained (somewhat like the case in Section 3.2):

{i} A many-to-one relationship exists between h_x and $e^{j2\pi\frac{\Delta_{px}}{\lambda}h_x}$, for a sparse spacing of $\frac{\Delta_{px}}{\lambda} > \frac{1}{2}$. In other words,

$$\hat{h}_{x,\text{phs}} \quad = \quad \frac{1}{2\pi}\frac{\lambda}{\Delta_{px}}\angle\frac{p_x}{p_p} \quad = \quad m\frac{\lambda}{\Delta_{px}} + h_x \tag{3.19}$$

would estimate h_x to ambiguously to within some integer multiple ($m\times$) of the frequency-*dependent* entity of $\pm\frac{\lambda}{\Delta_{px}}$, where m represents a to-be-determined integer.

{ii} The magnitude $\hat{u}_{\text{mag}} = \left|\frac{p_x}{p_p}\right|$, $\hat{v}_{\text{mag}} = \left|\frac{p_y}{p_p}\right|$ and $\hat{w}_{\text{mag}} = \left|\frac{p_z}{p_p}\right|$ (all of which are frequency-*in*dependent) could estimate h_x to within a $\pm$ sign ambiguity. That is,

$$\hat{h}_{x,\text{mag}}^{(s_u,s_v,s_w)} \quad = \quad s_u\hat{u}_{\text{mag}}\sin(\alpha_x)\cos(\beta_x) + s_v\hat{v}_{\text{mag}}\sin(\alpha_x)\sin(\beta_x) + s_w\hat{w}_{\text{mag}}\cos(\alpha_x), \tag{3.20}$$

with $s_u, s_v, s_w \in \{+1, -1\}$.

Next, define

$$\hat{m}^{(s_u,s_v,s_w)} \quad \stackrel{\text{def}}{=} \quad \arg\min_m \underbrace{\left|\left\{\left(m\frac{\lambda}{\Delta_{px}} + \overbrace{\frac{1}{2\pi}\frac{\lambda}{\Delta_{px}}\angle\left(s_u\frac{p_x}{p_p}\right)}^{=\hat{h}_{x,\text{phs}}}\right) - \hat{h}_{x,\text{mag}}^{(s_u,s_v,s_w)}\right\}\right|}_{\stackrel{\text{def}}{=}\epsilon_x(m)}. \tag{3.21}$$

The sign ambiguity in each of s_u, s_v, s_w implies that there exist altogether eight possible candidates for $\hat{m}^{(s_u,s_v,s_w)}$.

The above procedure in (3.19)-(3.21) for h_x can be analogously applied for h_y and for h_z.

To choose among the eight candidates of $\hat{m}^{(s_u,s_v,s_w)}$, [3] choose

$$(s_u^o, s_v^o, s_w^o) \stackrel{\text{def}}{=} \underset{(s_u,s_v,s_w)}{\arg\min} \sum_{\xi=x,y,z} \epsilon_\xi^2(\hat{m}^{(s_u,s_v,s_w)}). \tag{3.22}$$

This allows h_x, h_y and h_z to be *un*ambiguously estimated as

$$\hat{h}_x = \left(\hat{m}^{(s_u^o,s_v^o,s_w^o)} + \frac{1}{2\pi}\angle\frac{s_u^o p_x}{p_p}\right)\frac{\lambda}{\Delta_{px}}, \tag{3.23}$$

$$\hat{h}_y = \left(\hat{m}^{(s_u^o,s_v^o,s_w^o)} + \frac{1}{2\pi}\angle\frac{s_v^o p_y}{p_p}\right)\frac{\lambda}{\Delta_{py}}, \tag{3.24}$$

$$\hat{h}_z = \left(\hat{m}^{(s_u^o,s_v^o,s_w^o)} + \frac{1}{2\pi}\angle\frac{s_w^o p_z}{p_p}\right)\frac{\lambda}{\Delta_{pz}}. \tag{3.25}$$

To Estimate the Cartesian Direction-Cosines u, v, w

To estimate the Cartesian direction-cosines u, v, w,

If $\mathrm{r}(\mathbf{A}) = 3$ where $\mathrm{r}(\cdot)$ denotes the rank of matrix,[4]then

$$\begin{bmatrix} \hat{u} \\ \hat{v} \\ \hat{w} \end{bmatrix} = \begin{bmatrix} \sin(\alpha_x)\cos(\beta_x) & \sin(\alpha_x)\sin(\beta_x) & \cos(\alpha_x) \\ \sin(\alpha_y)\cos(\beta_y) & \sin(\alpha_y)\sin(\beta_y) & \cos(\alpha_y) \\ \sin(\alpha_z)\cos(\beta_z) & \sin(\alpha_z)\sin(\beta_z) & \cos(\alpha_z) \end{bmatrix}^{-1} \begin{bmatrix} \hat{h}_x \\ \hat{h}_y \\ \hat{h}_z \end{bmatrix} \tag{3.26}$$

The arrival-angles may thus be estimated as

$$\hat{\theta} = \arccos\hat{w}, \tag{3.27}$$

$$\hat{\phi} = \begin{cases} -\arccos\left(\frac{\hat{u}}{\sin(\hat{\theta})}\right), & \text{if } \frac{\hat{v}}{\sin(\hat{\theta})} < 0 \\ \arccos\left(\frac{\hat{u}}{\sin(\hat{\theta})}\right), & \text{if } \frac{\hat{v}}{\sin(\hat{\theta})} \geq 0. \end{cases} \tag{3.28}$$

Hence, a spatially spread acoustic vector-sensor can be used with *any* eigen-based parameter-estimation algorithm to perform direction finding. This technique may be applied to a *single* spatially spread acoustic vector-sensor alone (as will be demonstrated in Section 3.4), or to an array of *multiple* spatially spread acoustic vector-sensors (as will be demonstrated in Section 3.5).

[3] The above number of candidates may be reduced, if prior knowledge exists of the specific hemisphere or quadrant from which the incident source impinges. For example, suppose a source is prior known to impinge from the upper hemisphere: Then $w > 0$, i.e. $s_{x,w} = s_{y,w} = s_{z,w} = +1$, thereby $s_w^o = +1$. The number of possible candidates in (3.21) and (3.22) would then reduce from eight to four. Only $\{s_u^o, s_v^o\}$ needs to be determined in step {b}.

[4] The following square matrix is invertible, iff $(\alpha_\xi, \beta_\xi) \neq (\alpha_\nu, \beta_\nu)$ and $(\alpha_\xi, \beta_\xi) \neq (\pi - \alpha_\nu, \beta_\nu \pm \pi)$, $\forall \xi \neq \nu$ where $\xi, \nu \in \{x, y, z\}$. In terms of the array-configuration in Figure 3.2, this represents a mild condition that no two particle-velocity sensors may lie on a same radial line emanating from the Cartesian coordinates' origin.

3.4 A Complete Algorithm to Demonstrate Section 3.3's Proposed Scheme for a *Single* Acoustic Vector-Sensor that is Spatially *Distributed*

This section will demonstrate how the technique developed in Section 3.3 may be applied to a *single* spatially spread acoustic vector-sensor alone. This demonstration will be via adopting the "Uni-Vector-Hydrophone ESPRIT" algorithm of [53] (originally developed for an acoustic vector-sensor of *collocated* component-sensors) to accommodate a spatially *distributed* acoustic vector-sensor, via the technique in Section 3.3.

3.4.1 A Review of [53], Which is for One Acoustic Vector-Sensor Consisting of Only Collocated Component-Sensors

Suppose that K number of acoustic waves have traveled through an isotropic homogeneous medium, and impinge on an acoustic vector-sensor of spatially *collocated* component-sensors placed at the origin of the Cartesian coordinates. Suppose that the kth incoming signal $s_k(t)$ has power $\mathcal{P}_k$, a temporally monochromatic frequency f_k (which is distinct from all other incident signals' frequencies), and an initial phase φ_k. [5]

The 4×1 data-vector (observed at time t) equals

$$\mathbf{z}(t) \;=\; \sum_{k=1}^{K} \sqrt{\mathcal{P}_k}\mathbf{a}_k e^{j2\pi f_k t+\varphi_k} + \mathbf{n}(t), \tag{3.29}$$

where $\mathbf{a}_k = \mathbf{a}(\theta_k, \phi_k)$ symbolizes the kth incident source's steering vector from (1.2), and $\mathbf{n}(t)$ denotes the additive noise.

The *Uni-Vector-Hydrophone ESPRIT* algorithm [53] would form two time-delayed data-subsets, $\{\mathbf{z}(t_n),\, \forall n = 1, \ldots, N\}$ and $\{\mathbf{z}(t_n + \Delta_T), \forall\, n = 1, \ldots, N\}$, out of the observed data. In the above, Δ_T represents the time-delay between the two data-subsets.

The *Uni-Vector-Hydrophone ESPRIT* algorithmic steps are highlighted below. Their underlying motivations are explained in the detailed exposition in [53] itself.

{1} Form two $M \times N$ data-matrices $\mathbf{Z}_1 = [\mathbf{z}(t_1), \mathbf{z}(t_2), \cdots, \mathbf{z}(t_N)]$ and $\mathbf{Z}_2 = [\mathbf{z}(t_1 + \Delta_T), \mathbf{z}(t_2 + \Delta_T), \cdots, \mathbf{z}(t_N + \Delta_T)]$. Form a $2M \times N$ data-matrix $\mathbf{Z} = [\mathbf{Z}_1^T, \mathbf{Z}_2^T]^T$

{2} Eigen-decompose $\mathbf{Z}\mathbf{Z}^H$ to give a $2M \times K$ signal-subspace eigenvector matrix $\mathbf{E}_s = [\mathbf{E}_1^T, \mathbf{E}_2^T]^T$, whose K columns contain the K principal eigenvectors corresponding to the K largest-magnitude eigenvalues.

{3} Compute a $K \times K$ matrix,

$$\mathbf{\Psi} \;\stackrel{\text{def}}{=}\; \left(\mathbf{E}_1^H \mathbf{E}_1\right)^{-1} \left(\mathbf{E}_1^H \mathbf{E}_2\right) \;=\; \mathbf{T}^{-1}\mathbf{\Phi}\mathbf{T},$$

[5] The technique proposed in Section 3.3 may be readily applied to other data models, and is not restricted to the one reviewed here of [53]. This present data model serves only as an illustrative example. For example, wideband signals could be handled, by first applying the discrete Fourier transform (DFT) to the time-domain data, then each DFT-component can be subsequently processed individually.

whose kth eigenvalue may be denoted as $\mathbf{\Psi}$ equals $[\mathbf{\Phi}]_{k,k} = e^{j2\pi f_k \triangle_T}$, with the kth column of $\mathbf{T}$ being the corresponding right-eigenvector, for all $k = 1, \ldots, K$.

{4} These K impinging sources' steering-vectors are estimated as

$$[\hat{\mathbf{a}}_1, \cdots, \hat{\mathbf{a}}_K] \;=\; \frac{1}{2}\left\{\mathbf{E}_1\mathbf{T}^{-1} + \mathbf{E}_2\mathbf{T}^{-1}\mathbf{\Phi}^{-1}\right\},$$

each to within an *unknown* complex-value multiplicative scalar, which arises from the eigen-decomposition of $\mathbf{\Psi}$.

{5} From $\hat{\mathbf{a}}_k$, the direction cosines may be estimated as

$$\hat{u}_k \;\stackrel{\text{def}}{=}\; \frac{[\hat{\mathbf{a}}_k]_1}{[\hat{\mathbf{a}}_k]_4}, \tag{3.30}$$

$$\hat{v}_k \;\stackrel{\text{def}}{=}\; \frac{[\hat{\mathbf{a}}_k]_2}{[\hat{\mathbf{a}}_k]_4}, \tag{3.31}$$

$$\hat{w}_k \;\stackrel{\text{def}}{=}\; \frac{[\hat{\mathbf{a}}_k]_3}{[\hat{\mathbf{a}}_k]_4}, \tag{3.32}$$

where $[\mathbf{v}]_j$ symbolizes the jth entry if the vector $\mathbf{v}$. The kth source's two-dimensional direction-of-arrival may finally be estimated as

$$\hat{\theta}_k \;=\; \arcsin\left(\sqrt{\hat{u}_k^2 + \hat{v}_k^2}\right) \;=\; \arccos(\hat{w}_k), \tag{3.33}$$

$$\hat{\phi}_k \;=\; \arctan\left(\hat{v}_k/\hat{u}_k\right). \tag{3.34}$$

3.4.2 Applying Section 3.3's Proposed Scheme to [53] for *One* Acoustic Vector-Sensor with *Spatially Spread* Component-Sensors

Consider the spatially *spread* acoustic vector-sensor of Section 3.3, instead of the spatially *collocated* acoustic vector-sensor in [53]. The only change in the data-model of (3.29) is that now $\mathbf{a}_k = \mathbf{a}_{\text{gen}}(\theta_k, \phi_k)$ of (3.12). Then, Section 3.4.1's algorithmic steps {1} - {4} remain valid with no change, step {5} of Section 3.4.1 now needs be replaced by the procedure in Section 3.3.

Monte Carlo simulations below will demonstrate the proposed scheme's direction-finding efficacy and extended-aperture capability, despite the irregular array-configuration. The following settings are used for the array-configuration in Figure 3.2: $\{\alpha_x = 80^\circ, \beta_x = 15^\circ\}$, $\{\alpha_y = 85^\circ, \beta_y = 70^\circ\}$, $\{\alpha_z = 10^\circ, \beta_z = 40^\circ\}$, $\Delta = \Delta_{px} = \frac{20}{7}\Delta_{py} = \frac{20}{9}\Delta_{pz}$. Two pure-tone signals at digital frequencies (i.e. the actual frequencies divided by the time-sampling frequency) $f_1' = 0.45$ and $f_2' = 0.3$, impinge respectively from $(\theta_1, \phi_1) = (60^\circ, 140^\circ)$ and $(\theta_2, \phi_2) = (125^\circ, -40^\circ)$. All incident signals have unity power. The complex-phases φ_1 and φ_2 are deterministic. The additive noise is zero-mean, Gaussian, white spatio-temporally, with a known power of $\sigma^2 = 20$dB.

Figure 3.4(a) plots a "composite root-mean-square-error" (CRMSE) [6]of the first source's three Cartesian direction-cosine estimates, versus the inter-antenna spacing parameter $\frac{\Delta}{\lambda}$,

[6]The estimation bias is about an order-of-magnitude smaller than the corresponding estimation standard deviation, and hence not shown.

with λ referring to the shortest wavelength among all incident sources' wavelengths. Figure 3.4(b) does the same for the second source. This "composite root-mean-square-error" (CRMSE) is defined as $\frac{1}{I}\sum_{i=1}^{I}\sqrt{\frac{\delta_{u,k,i}^2+\delta_{v,k,i}^2}{2}}$, where $\delta_{u,k,i}$ ($\delta_{v,k,i}$) symbolizes the error in estimating the kth source's x-axis (y-axis) direction-cosine during the ith Monte Carlo experiment. Each data-point thereon consists of $I = 500$ statistically independent Monte Carlo experiments, each of which involves 200 temporal snapshots.

Figures 3.4(a) and 3.4(b) clearly demonstrate the proposed scheme's success in resolving the incident sources, even if the acoustic vector-sensor's four component-sensors are non-collocated and indeed very sparsely distributed in space. The collocated case (i.e. $\Delta = 0$) has its estimation error indicated in these figures by a dash-dot line, to ease comparison with the proposed scheme's performance. Note that the proposed scheme's estimation-error variance drops by about 1.5 orders-of-magnitude, as Δ increases (for the proposed scheme) by 2 orders-of-magnitude. Incidentally, this *ESPRIT*-based estimation approximates the Cramér-Rao lower bound, to the extent that *ESPRIT* does so.

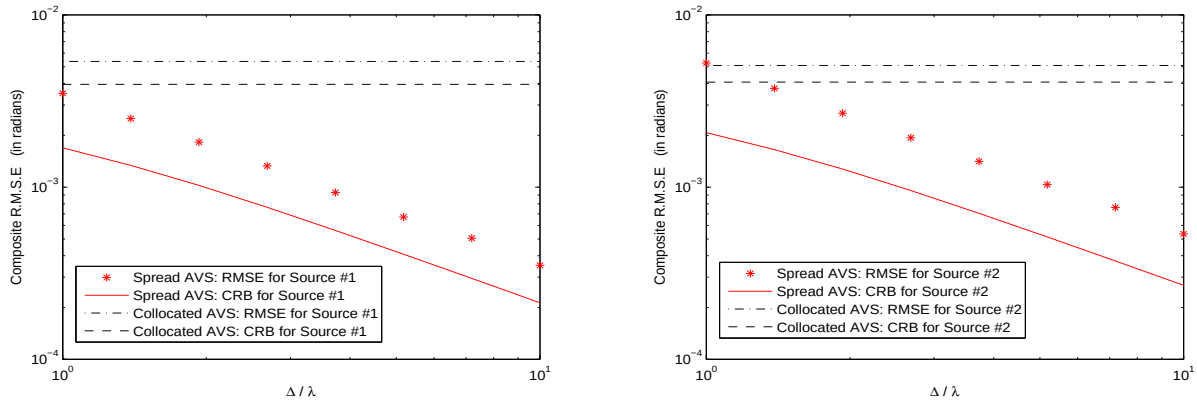

Figure 3.4: Monte Carlo simulations verifying the efficacy of the proposed scheme for a *single* acoustic vector-sensor alone.

3.5 A Complete Algorithm to Demonstrate Section 3.3's Proposed Scheme for *Several* Acoustic Vector-Sensors, Each of Which is Spatially *Distributed*.

This section will demonstrate how the technique developed in Section 3.3 may be applied to a *several* spatially spread acoustic vector-sensors. This demonstration will be via adopting the algorithm of [33] (originally developed for acoustic vector-sensors each consisting of *collocated* component-sensors) to accommodate a spatially *distributed* acoustic vector-sensor, via the technique in Section 3.3.

3.5.1 A Review of [33], Which is for Several Acoustic Vector-Sensors Each Consisting of *Collocated* Component-Sensors

Suppose that there exist L acoustic vector-sensors (with $L > K$) at arbitrary and possibly unknown locations. Let the ℓth acoustic vector-sensor's unknown location be (x_ℓ, y_ℓ, z_ℓ). All else remains the same as in Section 3.4.1.

The $4L\times 1$ array manifold for the entire L-element acoustic vector-sensor array is $\mathbf{a}_k \stackrel{\text{def}}{=} \mathbf{a}(\theta_k,\phi_k)\otimes\mathbf{q}(\theta_k,\phi_k)$, where the spatial phase factor $\mathbf{q}(\theta_k,\phi_k) \stackrel{\text{def}}{=} \left[e^{j2\pi\frac{x_1u_k+y_1v_k+z_1w_k}{\lambda_k}},\ldots,e^{j2\pi\frac{x_Lu_k+y_Lv_k+z_Lw_k}{\lambda_k}}\right]^T$, and $\otimes$ symbolizes the Kronecker-product operator.

The $4L\times 1$ data-vector (observed at time t) equals

$$\mathbf{z}(t) \;=\; \sum_{k=1}^{K}\sqrt{\mathcal{P}_k}\mathbf{a}_k e^{j2\pi f_k t+\varphi_k} + \mathbf{n}(t), \tag{3.35}$$

Define a $4L\times K$ array matrix $\mathbf{A} \stackrel{\text{def}}{=} [\mathbf{a}_1,\ldots,\mathbf{a}_K]$ which may be partitioned into four $L\times 4$ subarray data blocks $\{\mathbf{A}_1,\ldots,\mathbf{A}_4\}$. $\mathbf{A}_j \stackrel{\text{def}}{=} \mathbf{J}_j\mathbf{A}$, and $\mathbf{J}_j \stackrel{\text{def}}{=} \left[\mathbf{0}_{L,L\times(j-1)},\mathbf{I}_L,\mathbf{0}_{L,L\times(J-j)}\right]$ is a $L\times JL$ subarray-selection matrix, where $\mathbf{0}_{M,N}$ denotes a $M\times N$ zero matrix and $\mathbf{I}_M$ denotes an $M\times M$ identity matrix. Thus, the subarray data blocks $\{\mathbf{A}_1,\ldots,\mathbf{A}_4\}$ are interrelated as

$$\mathbf{A}_1 = \underbrace{\begin{bmatrix} u_1 & & \\ & \ddots & \\ & & u_K \end{bmatrix}}_{\stackrel{\text{def}}{=}\mathbf{\Phi}^{(u)}}\mathbf{A}_4, \quad \mathbf{A}_2 = \underbrace{\begin{bmatrix} v_1 & & \\ & \ddots & \\ & & v_K \end{bmatrix}}_{\stackrel{\text{def}}{=}\mathbf{\Phi}^{(v)}}\mathbf{A}_4, \quad \mathbf{A}_3 = \underbrace{\begin{bmatrix} w_1 & & \\ & \ddots & \\ & & w_K \end{bmatrix}}_{\stackrel{\text{def}}{=}\mathbf{\Phi}^{(w)}}\mathbf{A}_4$$

The algorithmic steps of [33] are highlighted below. Their underlying motivations are explained in the detailed exposition in [33] itself.

{1} Form two $M\times N$ data-matrices $\mathbf{Z} = [\mathbf{z}(t_1),\mathbf{z}(t_2),\cdots,\mathbf{z}(t_N)]$. Eigen-decompose $\mathbf{Z}\mathbf{Z}^H$ to give a $4L\times K$ signal-subspace eigenvector matrix $\mathbf{E}_s$, whose K columns contain the K principal eigenvectors corresponding to the K largest-magnitude eigenvalues.

{2} Construct the signal-subspace matrix pencil $\{\mathbf{E}_{s1},\mathbf{E}_{s4}\}$, $\{\mathbf{E}_{s2},\mathbf{E}_{s4}\}$, and $\{\mathbf{E}_{s3},\mathbf{E}_{s4}\}$, where $\mathbf{E}_{s1} = \mathbf{J}_1\mathbf{E}_s$, $\mathbf{E}_{s2} = \mathbf{J}_2\mathbf{E}_s$, $\mathbf{E}_{s3} = \mathbf{J}_3\mathbf{E}_s$, and $\mathbf{E}_{s4} = \mathbf{J}_4\mathbf{E}_s$. Compute a $K\times K$ matrix,

$$\begin{aligned}
\mathbf{\Psi}^{(u)} &\stackrel{\text{def}}{=} \left(\mathbf{E}_{s1}^H\mathbf{E}_{s1}\right)^{-1}\left(\mathbf{E}_{s1}^H\mathbf{E}_{s4}\right) &= \left(\mathbf{T}^{(u)}\right)^{-1}\mathbf{\Phi}^{(u)}\mathbf{T}^{(u)},\\
\mathbf{\Psi}^{(v)} &\stackrel{\text{def}}{=} \left(\mathbf{E}_{s2}^H\mathbf{E}_{s2}\right)^{-1}\left(\mathbf{E}_{s2}^H\mathbf{E}_{s4}\right) &= \left(\mathbf{T}^{(v)}\right)^{-1}\mathbf{\Phi}^{(v)}\mathbf{T}^{(v)},\\
\mathbf{\Psi}^{(w)} &\stackrel{\text{def}}{=} \left(\mathbf{E}_{s3}^H\mathbf{E}_{s3}\right)^{-1}\left(\mathbf{E}_{s3}^H\mathbf{E}_{s4}\right) &= \left(\mathbf{T}^{(w)}\right)^{-1}\mathbf{\Phi}^{(w)}\mathbf{T}^{(w)},
\end{aligned}$$

where $\mathbf{T}^{(u)}$, $\mathbf{T}^{(v)}$ and $\mathbf{T}^{(w)}$ are nonsingular matrices.

{3} These K impinging sources' steering-vectors are estimated as

$$\begin{aligned}
[\hat{\mathbf{a}}_k]_1 &\approx \left[\mathbf{\Phi}^{(u)}\right]_{k,k},\\
[\hat{\mathbf{a}}_k]_2 &\approx \left[\mathbf{\Phi}^{(v)}\right]_{k,k},\\
[\hat{\mathbf{a}}_k]_3 &\approx \left[\mathbf{\Phi}^{(w)}\right]_{k,k},
\end{aligned}$$

for $k = 1, \ldots, K$, where $[\mathbf{M}]_{i,j}$ symbolizes the (i,j)th entry of the matrix $\mathbf{M}$.

{4} From $\hat{\mathbf{a}}_k$, the direction cosines may be estimated as

$$\hat{u}_k \stackrel{\text{def}}{=} [\hat{\mathbf{a}}_k]_1 , \tag{3.36}$$

$$\hat{v}_k \stackrel{\text{def}}{=} [\hat{\mathbf{a}}_k]_2 , \tag{3.37}$$

$$\hat{w}_k \stackrel{\text{def}}{=} [\hat{\mathbf{a}}_k]_3 . \tag{3.38}$$

The kth source's two-dimensional direction-of-arrival may finally be estimated as

$$\hat{\theta}_k = \arcsin\left(\sqrt{\hat{u}_k^2 + \hat{v}_k^2}\right) = \arccos(\hat{w}_k), \tag{3.39}$$

$$\hat{\phi}_k = \arctan\left(\hat{v}_k / \hat{u}_k\right). \tag{3.40}$$

3.5.2 Applying Section 3.3's Proposed Scheme to [33] for *Multiple* Acoustic Vector-Sensors Each with *Spatially Spread* Component-Sensors

Consider an array of several spatially *spread* acoustic vector-sensor, instead of the spatially *collocated* acoustic vector-sensor in [33]. The only change in the data-model of (3.35) is that now $\mathbf{a}_k = \mathbf{a}_{\text{gen}}(\theta_k, \phi_k) \otimes \mathbf{q}(\theta_k, \phi_k)$. Then, Section 3.5.1's algorithmic steps {1} - {3} remain valid with no change, step {4} of Section 3.5.1 now needs be replaced by the procedure in Section 3.3. Monte Carlo simulations below will verify the efficacy of this synergy.

Here, $L = 5$, at the locations of $(3.9\lambda, 2.1\lambda, 1.8\lambda)$, $(2.1\lambda, 0.9\lambda, 1.5\lambda)$, $(4.5\lambda, 3.6\lambda, 5.7\lambda)$, $(2.1\lambda, 3.3\lambda, 1.5\lambda)$, $(6.0\lambda, 5.4\lambda, 3.3\lambda)$. Each acoustic vector-sensor follows the spatial distribution array-configuration in Figure 3.2, with $\{\alpha_x = 15^\circ, \beta_x = 75^\circ\}$, $\{\alpha_y = 40^\circ, \beta_y = 45^\circ\}$, $\{\alpha_z = 35^\circ, \beta_z = 85^\circ\}$, $\Delta = \Delta_{px} = \frac{20}{7}\Delta_{py} = \frac{20}{9}\Delta_{pz}$.

Two pure-tone signals at digital frequencies $f_1' = 0.4$ and $f_2' = 0.3$, impinge respectively from $(\theta_1, \phi_1) = (60^\circ, 135^\circ)$ and $(\theta_2, \phi_2) = (150^\circ, -40^\circ)$. All incident signals have unity power. The complex-phases φ_1 and φ_2 are deterministic.

Figure 3.5(a) plots a "composite root-mean-square-error" (CRMSE) of the first source's three Cartesian direction-cosine estimates, versus the signal-to-noise ratio SNR when $\frac{\Delta}{\lambda} = 3$. Figure 3.5(b) does the same for the second source. Each data-point thereon consists of $I = 500$ statistically independent Monte Carlo experiments, each of which involves 100 snapshots. Noticeably lower estimation errors are offered by the spatially spread constitution of each acoustic vector-sensor, relative to the case of collocated component-sensors within each acoustic vector-sensor.

3.6 Overview of the Proposed Algorithm

The main steps of the algorithm can be summarized as follows:

1. estimate sources' steering vectors

   a) for one acoustic vector-sensor with spatially spread component-sensors, refer to

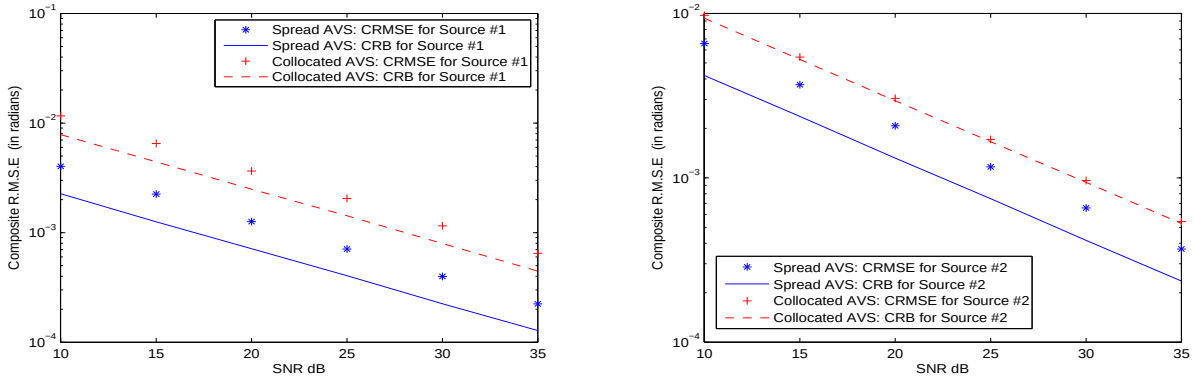

Figure 3.5: Monte Carlo simulations verifying the efficacy of the proposed scheme for *multiple* acoustic vector-sensors.

Section 3.4.1's algorithmic steps {1} - {4},

b) for several acoustic vector-sensors, each of which is spatially distributed, refer to Section 3.5.1's algorithmic steps {1} - {3}.

2. estimate the non-cartesian direction-cosines, h_x, h_y, h_z

   {i} low-variance estimate of h_x, but with 2π cyclic ambiguity, is obtain by (3.19),

   {ii} high-variance estimate of h_x, but with *no* 2π cyclic ambiguity, is obtain by (3.20),

   {iii} use {ii} to resolve 2π cyclic ambiguity in {i} by (3.21),

   {iv} resolve sign ambiguity by (3.22),

   {v} apply (3.19)-(3.22) for h_y, h_z,

   {vi} h_x, h_y, h_z are estimated by (3.23)-(3.25),

3. estimate the Cartesian direction-cosines, u, v, w, by (3.26)

4. estimate elevation-angle θ andazimuth-angle ϕ, by (3.27)-(3.28)

3.7 Summary

Many advantages are advanced by the recent synergy between customary interferometry-based direction finding and the new self-normalization approach of direction finding. This chapter further generalizes this synergy, by proposing a new direction-finding algorithm to allow the acoustic vector-sensor's four component-sensors may be spatially displaced over a general array-grid, perhaps with a much extended spatial aperture, thereby improving direction-finding accuracy by *orders of magnitude*, while mitigating hardware-implementation difficulties in spatially collocating the four component-sensors at one point in space.

An electromagnetic counterpart exists in [156] for this proposed acoustic vector-sensor scheme. Both the electromagnetic and the acoustic schemes are predicated on how each component-sensor's magnitude relates to the incident sources' unknown but to-be-estimated parameters. Due to the fundamental differences between acoustics and electromagnetics,

these magnitudes take on entirely different mathematical forms. Hence, the proposed algorithmic steps (and the applicable array configurations) are fundamentally different here from [156].

Chapter 4

Acoustic Direction Finding Using a Spatially Spread Tri-Axial Velocity Sensor

[1]

4.1 This Work's Contribution

The literature on tri-axial velocity sensor direction finding mostly presumes that the three uni-axial velocity sensors are spatially collocated. This imposes a non-trivial complication in hardware implementation and can be achieved only approximately at best. This demanding requirement of spatial collocation requirement is relaxed for the four-component acoustic vector sensor (i.e. the three uni-axial velocity sensors plus one mandatory pressure sensor) in Chapter 3, to allow the four component-sensors to be located separately, thereby realizing an extended spatial aperture, consequentially improving the azimuth/elevation resolution of incident emitters. Despite the spatial separation among these "component sensors", the scheme in Chapter 3 allows closed-form localization using eigen-based parameter estimation algorithms, with*out* open-ended iterative searches. Furthermore, the new spatially spread configuration in Chapter 3 would also avoid the considerable difficulties/costs in hardware implementation to collocate the four "component sensors".

One shortcoming of the scheme in Chapter 3, however, is its requirement of a pressure sensor, to be deployed along with the three uni-axial velocity sensors. This would be problematic for *near*field localization, to estimate the emitter's radial distance from the four-component "acoustic vector sensor" (in addition to the emitter's azimuth/elevation angle of arrival), because the pressure sensor's data differ from the tri-axial velocity sensor's data by a *magnitude*-scaling factor and a complex *phase* [135], both of which vary with the emitter-sensor distance and the signal frequency. Please see [135] for the details.

This work will propose a new algorithm to estimate the incident emitters' azimuth-elevation direction of arrival via eigen-based parameter-estimation algorithms, based on

[1] This chapter is taken from [165], jointly authored by the candidate and his chief supervisor.

data collected from only a tri-axial velocity sensor which is spatially separated to spread over a large spatial aperture (thereby improving resolution in three-dimensional space), even without the pressure sensor (to avoid the aforementioned complex phase and magnitude scaling factor that vary with signal frequency and with the emitter-sensor distance).

4.2 The New Scheme's Underlying Philosophy – Illustrated by a Simple Array Configuration

To motivate the proposed scheme, this section will focus on one particularly simple array configuration to spatially spread the three uni-axial velocity sensors. The proposed scheme will later be developed in Section 4.3 to any arbitrary array configuration.

4.2.1 The New Array Manifold for the Illustrative Example of Figure 4.1

In the simple array configuration of Figure 4.1, a z-axis *oriented* velocity sensor is placed at the Cartesian origin, whereas an x-axis (y-axis) *oriented* velocity sensor lies on the x-axis (y-axis), at a distance Δ_x (Δ_y) from the Cartesian origin. The displacements, Δ_x and Δ_y, may each be positive or negative, though the special case of $\Delta_x > 0$ and $\Delta_y > 0$ is illustrated Figure 4.1, which labels the uni-axial velocity sensor oriented along the x-axis (y-axis, z-axis) as V_x (V_y, V_z).

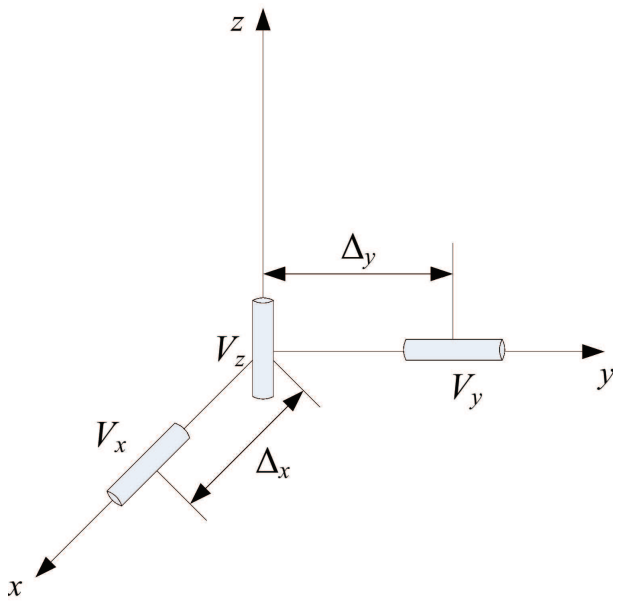

Figure 4.1: The tri-axial velocity sensor has its three component-sensors spatially spread over three-dimensional space in a "triangle-like" array configuration. Illustrated here is the special case of $\Delta_x > 0$ and $\Delta_y > 0$.

This spatially *distributed* tri-axial velocity sensor has an array manifold different from the spatially *collocated* array manifold of (1.2), because the two off-origin uni-axial velocity sensors introduce the "spatial phase factors" of $e^{j\frac{2\pi}{\lambda}\Delta_x u}$ and $e^{j\frac{2\pi}{\lambda}\Delta_y v}$. Hence, Figure 4.1

has the array manifold,

$$\mathbf{a}_{\text{triangle}} \;=\; \begin{bmatrix} u\ e^{j\frac{2\pi}{\lambda}\Delta_x u} \\ v\ e^{j\frac{2\pi}{\lambda}\Delta_y v} \\ w \end{bmatrix}. \tag{4.1}$$

This new array-manifold in (4.1) now depends on the incident signal's wavelength, λ. However, its Frobenius norm nonetheless equals unity $\forall\theta,\phi,\lambda$ (or equivalently $\forall u,v,w,\lambda$).

4.2.2 The Proposed Self-Normalization Direction Finding Algorithm for the Illustrative Example of Figure 4.1

In eigen-based approaches of direction finding, the uni-axial velocity sensor's observed data would be formed into a 3×3 spatial correlation matrix. Then, eigen-decompose this 3×3 matrix (plus any additional processing to decorrelate any cross-correlated incident signals, and/or to decouple simultaneous sources' steering vectors). Thereby obtainable would be the steering vector estimate for each incident source:

$$\hat{\mathbf{a}} \;\approx\; \begin{bmatrix} p_x \\ p_y \\ p_z \end{bmatrix} \;\stackrel{\text{def}}{=}\; c\ \mathbf{a}_{\text{triangle}}, \tag{4.2}$$

which is correct with respect to the true value $\mathbf{a}_{\text{triangle}}$, to within an unknown complex-value scalar of c. The unknown c arises from the eigen-decomposition, but may be estimated as

$$\hat{c} \;=\; \sqrt{|p_x|^2+|p_y|^2+|p_z|^2}\ e^{j\angle(s_w p_z)}, \tag{4.3}$$

if prior knowledge is available on the sign (s_w) of w. If there were no noise and/or if there were an infinite number of snapshots, the approximation in (4.2) would become a equality. The subsequent exposition will write all such approximations as equalities, for simplicity.

Next, normalize the first component in (4.2) by $\hat{c}$ to give

$$\frac{p_x\ e^{-j\angle(s_w p_z)}}{\sqrt{|p_x|^2+|p_y|^2+|p_z|^2}} \;=\; u\ e^{j\frac{2\pi}{\lambda}(\Delta_x u)}. \tag{4.4}$$

From (4.4), two complementary estimators of u may be obtained, simultaneously, in parallel:

{i} An one-to-many relationship links the complex phase factor $e^{j2\pi\frac{\Delta_x}{\lambda}u}$ and $u\in[-1,1]$, for the extended aperture case of $\frac{\Delta_x}{\lambda}>\frac{1}{2}$. Hence, exploiting the complex phase of only the first element of $\hat{\mathbf{a}}$,

$$\hat{u}_{\text{phs}} \;=\; \frac{1}{2\pi}\frac{\lambda}{\Delta_x}\angle\frac{s_u p_x\ e^{-j\angle(s_w p_z)}}{\sqrt{|p_x|^2+|p_y|^2+|p_z|^2}} \;=\; m\frac{\lambda}{\Delta_x}+u \tag{4.5}$$

can be obtained as an estimate u, but only ambiguously to within some (to-be-determined) integer multiple ($m\times$) of $\pm\frac{\lambda}{\Delta_x}$, where m denotes a to-be-determined integer in $\left\{\lceil\frac{1}{2}-\frac{\Delta_x}{\lambda}\rceil,\cdots,\lfloor\frac{1}{2}+\frac{\Delta_x}{\lambda}\rfloor\right\}$.

{ii} An one-to-two relationship connects the magnitude $|u|$ and $u \in [-1,1]$. Hence, exploiting the relative magnitude of p_x,

$$\hat{u}_{\text{mag}} \;=\; \left| \frac{p_x}{\sqrt{|p_x|^2+|p_y|^2+|p_z|^2}} \right| \;=\; \pm u \tag{4.6}$$

can be obtained as an estimate u, but only ambiguously to within some to-be-determined $\pm$ sign.

These two estimates, $\hat{u}_{\text{phs}}$ and $\hat{u}_{\text{mag}}$, can disambiguate each other, as below:

{a} If $\hat{u}_{\text{mag}} = u$, resolve the cyclic ambiguity via

$$\hat{m}_u^+ \stackrel{\text{def}}{=} \arg\min_m \underbrace{\left| \left\{ \left(m\frac{\lambda}{\Delta_x} + \overbrace{\frac{1}{2\pi}\frac{\lambda}{\Delta_x}\angle\frac{p_x\; e^{-j\angle(s_w p_z)}}{\sqrt{|p_x|^2+|p_y|^2+|p_z|^2}}}^{=\hat{u}_{\text{phs}}} \right) - \overbrace{\left| \frac{p_x}{\sqrt{|p_x|^2+|p_y|^2+|p_z|^2}} \right|}^{=\hat{u}_{\text{mag}}} \right\} \right|}_{\stackrel{\text{def}}{=}\epsilon_u^+(m)}. \tag{4.7}$$

{b} If $\hat{u}_{\text{mag}} = -u$, resolve the cyclic ambiguity through

$$\hat{m}_u^- \stackrel{\text{def}}{=} \arg\min_m \underbrace{\left| \left\{ \left(m\frac{\lambda}{\Delta_x} + \overbrace{\frac{1}{2\pi}\frac{\lambda}{\Delta_x}\angle\frac{-p_x\; e^{-j\angle(s_w p_z)}}{\sqrt{|p_x|^2+|p_y|^2+|p_z|^2}}}^{=\hat{u}_{\text{phs}}} \right) - - \overbrace{\left| \frac{p_x}{\sqrt{|p_x|^2+|p_y|^2+|p_z|^2}} \right|}^{=\hat{u}_{\text{mag}}} \right\} \right|}_{\stackrel{\text{def}}{=}\epsilon_u^-(m)}. \tag{4.8}$$

{c} How to decide between $\hat{u}_{\text{mag}} = u$ versus $\hat{u}_{\text{mag}} = -u$? Decide in favor of $\hat{u}_{\text{mag}} = u$, if $\epsilon_u^+(\hat{m}_u^+) < \epsilon_u^-(\hat{m}_u^-)$. Choose $\hat{u}_{\text{mag}} = -u$, if $\epsilon_u^+(\hat{m}_u^+) \geq \epsilon_u^-(\hat{m}_u^-)$.

{d} Hence, u is *un*ambiguously estimated from the phase factor as

$$\acute{u} \;=\; \begin{cases} \left(\hat{m}_u^+ + \frac{1}{2\pi}\angle\frac{p_x\; e^{-j\angle(s_w p_z)}}{\sqrt{|p_x|^2+|p_y|^2+|p_z|^2}} \right)\frac{\lambda}{\Delta_x}, & \text{if } \epsilon_u^+(\hat{m}_u^+) < \epsilon_u^-(\hat{m}_u^-); \\ \left(\hat{m}_u^- + \frac{1}{2\pi}\angle\frac{-p_x\; e^{-j\angle(s_w p_z)}}{\sqrt{|p_x|^2+|p_y|^2+|p_z|^2}} \right)\frac{\lambda}{\Delta_x}, & \text{if } \epsilon_u^+(\hat{m}_u^+) \geq \epsilon_u^-(\hat{m}_u^-). \end{cases} \tag{4.9}$$

The y-axis Cartesian direction cosine estimate, $\acute{v}$, may be obtained analogously via (4.4)-(4.9).

{e} Items {c} and {d} indicate that both the magnitude and the phase of the first two entries of $\mathbf{a}_{\text{triangle}}$ can offer information on u, v. Between $\hat{u}_{\text{mag}}$ and $\acute{u}$, which should be used? It makes intuitive sense that the choice should result in a steering vector closest to orthogonality to the data's noise subspace. Using this philosophy, proceed as follows: Let $\mathbf{E}_n$ denote $3\times(3-K)$ noise subspace eigenvector matrix that contains the $3-K$ number of eigenvectors spanning the noise subspace of the data correlation

matrix, where K is the number of incident sources. Then, (u, v) may be estimated as

$$(\hat{u}, \hat{v}) \;=\; \begin{cases} (\mathrm{s}_u^o \hat{u}_{\mathrm{mag}}, \mathrm{s}_v^o \hat{v}_{\mathrm{mag}}), & \text{if } \left\| \mathbf{a}\left(\mathrm{s}_u^o \hat{u}_{\mathrm{mag}}, \mathrm{s}_v^o \hat{v}_{\mathrm{mag}}\right)^H \mathbf{E}_n \right\|_2 < \left\| \mathbf{a}\left(\acute{u}, \acute{v}\right)^H \mathbf{E}_n \right\|_2, \\ (\acute{u}, \acute{v}), & \text{if } \left\| \mathbf{a}\left(\mathrm{s}_u^o \hat{u}_{\mathrm{mag}}, \mathrm{s}_v^o \hat{v}_{\mathrm{mag}}\right)^H \mathbf{E}_n \right\|_2 > \left\| \mathbf{a}\left(\acute{u}, \acute{v}\right)^H \mathbf{E}_n \right\|_2, \end{cases} \tag{4.10}$$

where $\mathrm{s}_u^o(\mathrm{s}_v^o)$ is the estimate of the sign $\mathrm{s}_u(\mathrm{s}_v)$ of $u(v)$), $\|\cdot\|$ denotes the Frobenius norm of the vector inside, and ^{H} symbolizes the Hermitian operator.

Finally, $\hat{u}$ and $\hat{v}$ together give azimuth/elevation arrival angle estimates,

$$\hat{\phi} \;=\; \begin{cases} \arctan\left(\frac{\hat{v}}{\hat{u}}\right), & \text{if } s_u^o = +1 \\ \pi + \arctan\left(\frac{\hat{v}}{\hat{u}}\right), & \text{if } s_u^o = -1 \text{ and } s_v^o = +1 \\ -\pi + \arctan\left(\frac{\hat{v}}{\hat{u}}\right), & \text{if } s_u^o = -1 \text{ and } s_v^o = -1, \end{cases} \tag{4.11}$$

$$\hat{\theta} \;=\; \begin{cases} \arcsin\left(\frac{\hat{u}}{\cos(\hat{\phi})}\right), & \text{if } s_w^o = +1 \\ \pi - \arcsin\left(\frac{\hat{u}}{\cos(\hat{\phi})}\right), & \text{if } s_w^o = -1. \end{cases} \tag{4.12}$$

These angle-of-arrival estimates enjoy a validity region over an hemisphere defined over $\theta \in [0, \pi/2)$ and $\phi \in (-\pi, \pi]$. The $\pm\pi$ terms appear above, because of the following considerations: If $s_u^\circ = -1$ and $s_v^\circ = -1$), then $\hat{\phi} \in \left(-\pi, -\frac{\pi}{2}\right)$. If $s_u^\circ = +1$, then $\hat{\phi} \in \left(\frac{-\pi}{2}, \frac{\pi}{2}\right)$. If $s_u^\circ = -1$ and $s_v^\circ = +1$), then $\hat{\phi} \in \left(\frac{\pi}{2}, \pi\right)$ If $s_w = +1$, then $\hat{\theta} \in \left[0, \frac{\pi}{2}\right]$. If $s_w = -1$, then $\hat{\theta} \in \left(\frac{\pi}{2}, \pi\right]$.

To summarize: With prior knowledge of the sign of w, the azimuth/elevation angle of arrival has been estimated *un*ambiguously, despite any sparse non-collocation among the three uni-axial velocity sensors. [2]

This array configuration is simpler than the arbitrary configuration to be introduced in Section 4.3, in that the first two elements here in (4.1) each depends on only one of the three Cartesian direction cosines (i.e. u, v, w). Hence, only one sign ambiguity requires disambiguation at each uni-axial velocity sensor, whereas all three sign ambiguities need to be resolved for each uni-axial velocity sensor of the arbitrarily spaced configuration to be introduced in Section 4.3.

4.3 The New Scheme for Any *Arbitrarily Spread* Tri-Axial Velocity Sensor

This section will show how the algorithmic philosophy in Section 4.2 can apply to the arbitrarily *general* array configuration of Figure 4.2, so long as the three uni-axial velocity sensors remain orthogonal among themselves. The algorithm's basic philosophy here remains as in Section 4.2: To resolve the one-to-many cyclic ambiguity in $\hat{u}_{\mathrm{phs}}$, by the one-to-two sign ambiguity in $\hat{u}_{\mathrm{mag}}$.

[2] This prior knowledge of the sign of w may be replaced by a prior knowledge of the sign of u (v), if the x-axis (y-axis) oriented uni-axial velocity sensor is placed at the Cartesian origin and if the z-axis oriented uni-axial velocity sensor is relocated somewhere on the z-axis.

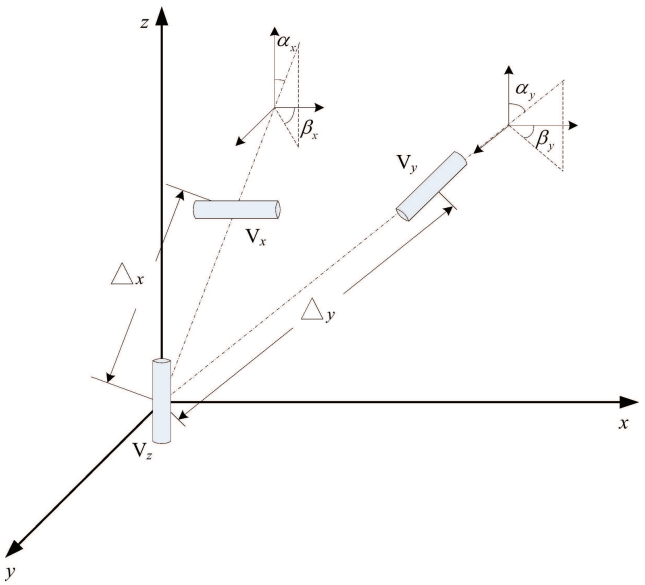

Figure 4.2: The tri-axial velocity sensor is spread *arbitrarily* over three-dimensional space, while retaining orthogonal orientations among its three component-sensors.

4.3.1 The Array Manifold for an *Arbitrarily Spread* Tri-Axial Velocity Sensor

Let the z-axis *oriented* uni-axial velocity sensor lies again at the origin of the spherical coordinates, *without loss of generality*.[3] However, allow the other two uni-axial velocity sensors be located *arbitrarily* in three-dimensional space.

For such general spacing, the corresponding 3×1 array manifold equals

$$\mathbf{a}_{\text{gen}}(\theta,\phi) \;=\; \begin{bmatrix} u\; e^{j\frac{2\pi}{\lambda}[u\Delta_x \sin(\alpha_x)\cos(\beta_x)+v\Delta_x \sin(\alpha_x)\sin(\beta_x)+w\Delta_x \cos(\alpha_x)]} \\ v\; e^{j\frac{2\pi}{\lambda}[u\Delta_y \sin(\alpha_y)\cos(\beta_y)+v\Delta_y \sin(\alpha_y)\sin(\beta_y)+w\Delta_y \cos(\alpha_y)]} \\ w \end{bmatrix}. \quad (4.13)$$

The symbols α_x, α_y, β_x, β_y are graphically defined in (4.13). Unlike the simple array manifold (4.1) in Section 4.2, each complex phase in (4.13) now depends on all three Cartesian direction cosines (u,v,w). Consequentially, the subsequent disambiguation would become more complicated, but the approach remains as before in Section 4.2.

4.3.2 The Proposed Algorithm for an *Arbitrarily Spread* Tri-Axial Velocity Sensor

By eigen-decomposition of the spatial correlation matrix of the collected data, the following steering vector estimate will be obtained, instead of the estimate in (4.14):

[3] If it is another uni-axial velocity sensor that lies at the origin, or if none of the uni-axial velocity sensors lie at the origin, the entire array manifold in (4.13) would simply be multiplied by a common spatial phase factor, which will not materially affect the subsequent development.

$$\hat{\mathbf{a}} \approx \begin{bmatrix} p_x \\ p_y \\ p_z \end{bmatrix} \stackrel{\text{def}}{=} c\, \mathbf{a}_{\text{gen}}, \tag{4.14}$$

With prior knowledge of s_w (defined earlier above (4.4)), normalize each of the first three components of (4.13) by the same $\hat{c}$ as defined in Section 4.2, thereby yielding

$$\frac{p_x\ e^{-j\angle(s_w p_z)}}{\sqrt{|p_x|^2+|p_y|^2+|p_z|^2}} = u\, e^{j\frac{2\pi}{\lambda}\Delta_x h_x}, \tag{4.15}$$

$$\frac{p_y\ e^{-j\angle(s_w p_z)}}{\sqrt{|p_x|^2+|p_y|^2+|p_z|^2}} = v\, e^{j\frac{2\pi}{\lambda}\Delta_y h_y}, \tag{4.16}$$

where

$$h_x = u\sin(\alpha_x)\cos(\beta_x) + v\sin(\alpha_x)\sin(\beta_x) + w\cos(\alpha_x), \tag{4.17}$$

$$h_y = u\sin(\alpha_y)\cos(\beta_y) + v\sin(\alpha_y)\sin(\beta_y) + w\cos(\alpha_y) \tag{4.18}$$

symbolize the non-Cartesian direction cosines obtained by projecting the gradient vector onto the respective axes on which Δ_x and Δ_y, respectively, lie. These non-Cartesian direction cosines (h_x, h_y) are counterpart to the Cartesian direction cosines (u, v) in the Section 4.2 where all uni-axial velocity sensors lie on some Cartesian axis.

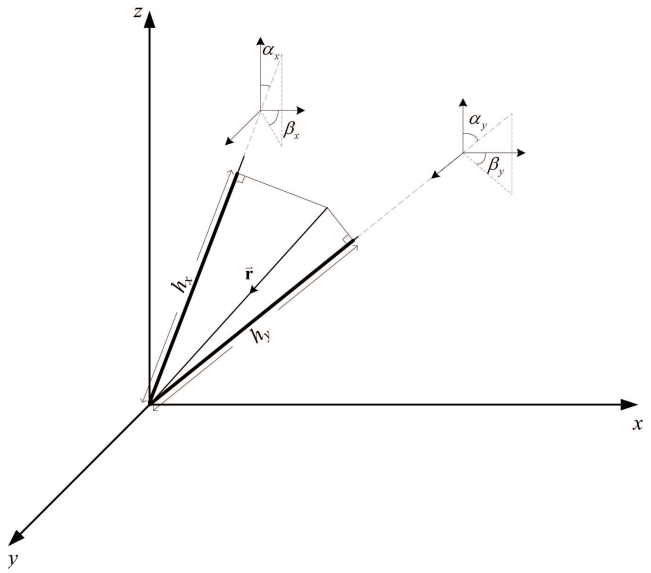

Figure 4.3: A geometric illustration of the *non*-Cartesian direction cosines, h_x and h_y, in three-dimensional space.

Next, Section 4.3.2) will explain how to estimate the *non-Cartesian* direction cosines (h_x, h_y), from which Section 4.3.2) will show how to estimate the *Cartesian* direction cosines (u, v, w).

To Estimate the Non-Cartesian Direction Cosines (h_x, h_y)

Consider first the estimation of h_x.

From (4.15), two complementary estimators of h_x can be computed simultaneously in parallel (somewhat like the case in Section 4.2):

{i} A many-to-one relationship connects h_x and $e^{j2\pi\frac{\Delta_x}{\lambda}h_x}$, for a sparse spacing of $\frac{\Delta_x}{\lambda} > \frac{1}{2}$. Thus,

$$\hat{h}_{x,\text{phs}} \;=\; \frac{1}{2\pi}\frac{\lambda}{\Delta_x}\angle\left(\frac{s_u p_x e^{-j\angle(s_w p_z)}}{\sqrt{|p_x|^2+|p_y|^2+|p_z|^2}}\right) \;=\; m\frac{\lambda}{\Delta_x}+h_x \tag{4.19}$$

would estimate h_x, ambiguously to within some integer multiple ($m\times$) of $\pm\frac{\lambda}{\Delta_x}$, where m represents a to-be-determined integer.

{ii} The magnitudes

$$\begin{aligned}\hat{u}_{\text{mag}} &= \left|\frac{p_x}{\sqrt{|p_x|^2+|p_y|^2+|p_z|^2}}\right|,\\ \hat{v}_{\text{mag}} &= \left|\frac{p_y}{\sqrt{|p_x|^2+|p_y|^2+|p_z|^2}}\right|,\\ \hat{w}_{\text{mag}} &= \left|\frac{p_z}{\sqrt{|p_x|^2+|p_y|^2+|p_z|^2}}\right|\end{aligned}$$

together can estimate h_x to within a $\pm$ sign ambiguity:

$$\hat{h}_{x,\text{mag}}^{(s_u,s_v)} \;=\; s_u\hat{u}_{\text{mag}}\sin(\alpha_x)\cos(\beta_x)+s_v\hat{v}_{\text{mag}}\sin(\alpha_x)\sin(\beta_x)+s_w\hat{w}_{\text{mag}}\cos(\alpha_x), \tag{4.20}$$

with $s_u, s_v, s_w \in \{+1,-1\}$, s_w known, but s_u and s_v yet to be determined.

Next, estimate $m \in \left\{\lceil\frac{1}{2}-\frac{\Delta_x}{\lambda}\rceil,\cdots,\lfloor\frac{1}{2}+\frac{\Delta_x}{\lambda}\rfloor\right\}$, in terms of any s_u and s_v:

$$\hat{m}^{(s_u,s_v)} \;\stackrel{\text{def}}{=}\; \arg\min_m \underbrace{\left|\left\{\left(m\frac{\lambda}{\Delta_x}+\overbrace{\frac{1}{2\pi}\frac{\lambda}{\Delta_x}\angle\left(\frac{s_u p_x e^{-j\angle(s_w p_z)}}{\sqrt{|p_x|^2+|p_y|^2+|p_z|^2}}\right)}^{=\hat{h}_{x,\text{phs}}}\right)-\hat{h}_{x,\text{mag}}^{(s_u,s_v)}\right\}\right|}_{\stackrel{\text{def}}{=}\epsilon_x(m)}. \tag{4.21}$$

The sign ambiguity in s_u and the sign ambiguity in s_v together imply four possible candidates for $\hat{m}^{(s_u,s_v)}$.

The above procedure in (4.19)-(4.21) for h_x can be applied analogously for h_y.

To choose among the four candidates of $\hat{m}^{(s_u,s_v)}$, choose

$$(s_u^o, s_v^o) \;\stackrel{\text{def}}{=}\; \arg\min_{(s_u,s_v)} \left[\epsilon_x^2\left(\hat{m}^{(s_u,s_v)}\right)+\epsilon_y^2\left(\hat{m}^{(s_u,s_v)}\right)\right]. \tag{4.22}$$

The above facilitates h_x and h_y to be *un*ambiguously estimated as

$$\hat{h}_x \;=\; \left(\hat{m}^{(s_u^o,s_v^o)}+\frac{1}{2\pi}\angle\frac{s_u^o p_x e^{-j\angle(s_w p_z)}}{\sqrt{|p_x|^2+|p_y|^2+|p_z|^2}}\right)\frac{\lambda}{\Delta_x}, \tag{4.23}$$

$$\hat{h}_y \;=\; \left(\hat{m}^{(s_u^o,s_v^o)}+\frac{1}{2\pi}\angle\frac{s_v^o p_y e^{-j\angle(s_w p_z)}}{\sqrt{|p_x|^2+|p_y|^2+|p_z|^2}}\right)\frac{\lambda}{\Delta_y}. \tag{4.24}$$

The disadvantage of omitting the pressure sensor (which is required in Chapter 3) is that the emitter may now be localized to only within an hemisphere. This is because only two constraints are available:

$\{1\}$ $m\frac{\lambda}{\Delta_x} + \hat{h}_{x,\text{phs}} = \hat{h}_{x,\text{mag}}$ from (4.19), and

$\{2\}$ $m\frac{\lambda}{\Delta_y} + \hat{h}_{y,\text{phs}} = \hat{h}_{y,\text{mag}}$, which is a counterpart of (4.19) for h_y.

To Estimate the Cartesian Direction Cosines (u, v)

From (4.17)-(4.18),

$$\begin{bmatrix} \hat{h}_x \\ \hat{h}_y \end{bmatrix} = \underbrace{\begin{bmatrix} \sin(\alpha_x)\cos(\beta_x) & \sin(\alpha_x)\sin(\beta_x) & \cos(\alpha_x) \\ \sin(\alpha_y)\cos(\beta_y) & \sin(\alpha_y)\sin(\beta_y) & \cos(\alpha_y) \end{bmatrix}}_{=\mathbf{M}} \begin{bmatrix} \acute{u} \\ \acute{v} \\ s_w\sqrt{1-\acute{u}^2-\acute{v}^2} \end{bmatrix} \quad (4.25)$$

The above defined matrix $\mathbf{M}$ would have a full rank of two, if and only if the two *non-Cartesian* direction cosines h_x and h_y are non-parallel. Therefore, the *Cartesian* direction cosines may be estimated from the phase factor as $(\acute{u}, \acute{v})$

$$= \begin{cases} \left(\frac{\chi_1+([\mathbf{b}]_2[\mathbf{a}]_3-[\mathbf{a}]_2[\mathbf{b}]_3)\chi_2}{\chi_3}, \frac{\chi_4-\chi_2}{\chi_5}\right), & \text{if } \left(\hat{u}_{\text{mag}} - \left|\frac{\chi_1+([\mathbf{b}]_2[\mathbf{a}]_3-[\mathbf{a}]_2[\mathbf{b}]_3)\chi_2}{\chi_3}\right|\right)^2 + \left(\hat{v}_{\text{mag}} - \left|\frac{\chi_4-\chi_2}{\chi_5}\right|\right)^2 \\ & \quad < \left(\hat{u}_{\text{mag}} - \left|\frac{\chi_1-([\mathbf{b}]_2[\mathbf{a}]_3-[\mathbf{a}]_2[\mathbf{b}]_3)\chi_2}{\chi_3}\right|\right)^2 + \left(\hat{v}_{\text{mag}} - \left|\frac{\chi_4+\chi_2}{\chi_5}\right|\right)^2, \\ \left(\frac{\chi_1-([\mathbf{b}]_2[\mathbf{a}]_3-[\mathbf{a}]_2[\mathbf{b}]_3)\chi_2}{\chi_3}, \frac{\chi_4+\chi_2}{\chi_5}\right), & \text{if } \left(\hat{u}_{\text{mag}} - \left|\frac{\chi_1+([\mathbf{b}]_2[\mathbf{a}]_3-[\mathbf{a}]_2[\mathbf{b}]_3)\chi_2}{\chi_3}\right|\right)^2 + \left(\hat{v}_{\text{mag}} - \left|\frac{\chi_4-\chi_2}{\chi_5}\right|\right)^2 \\ & \quad > \left(\hat{u}_{\text{mag}} - \left|\frac{\chi_1-([\mathbf{b}]_2[\mathbf{a}]_3-[\mathbf{a}]_2[\mathbf{b}]_3)\chi_2}{\chi_3}\right|\right)^2 + \left(\hat{v}_{\text{mag}} - \left|\frac{\chi_4+\chi_2}{\chi_5}\right|\right)^2, \end{cases} \quad (4.26)$$

where

$$\begin{aligned}
\chi_1 &= [\mathbf{b}]_1^2[\mathbf{a}]_3\left\{-([\mathbf{a}]_2[\mathbf{b}]_2+[\mathbf{a}]_3[\mathbf{b}]_3)\hat{h}_x + ([\mathbf{a}]_2^2+[\mathbf{a}]_3^2)\hat{h}_y\right\} \\
&\quad +[\mathbf{a}]_1^2[\mathbf{b}]_3\left\{-([\mathbf{b}]_2^2+[\mathbf{b}]_3^2)\hat{h}_x + ([\mathbf{a}]_2[\mathbf{b}]_2+[\mathbf{a}]_3[\mathbf{b}]_3)\hat{h}_y\right\} \\
&\quad +[\mathbf{a}]_1[\mathbf{b}]_1\left\{([\mathbf{b}]_2^2[\mathbf{a}]_3+[\mathbf{a}]_2[\mathbf{b}]_2[\mathbf{b}]_3+2[\mathbf{a}]_3[\mathbf{b}]_3^2)\hat{h}_x - ([\mathbf{a}]_2[\mathbf{b}]_2[\mathbf{a}]_3+[\mathbf{a}]_2^2[\mathbf{b}]_3+2[\mathbf{a}]_3^2[\mathbf{b}]_3)\hat{h}_y\right\}, \\
\chi_2 &= |[\mathbf{b}]_1[\mathbf{a}]_3 - [\mathbf{a}]_1[\mathbf{b}]_3| \\
&\quad \cdot\Big\{\Big([\mathbf{a}]_1^2[\mathbf{b}]_2^2+[\mathbf{b}]_2^2[\mathbf{a}]_3^2-2[\mathbf{a}]_2[\mathbf{b}]_2[\mathbf{a}]_3[\mathbf{b}]_3+[\mathbf{a}]_1^2[\mathbf{b}]_3^2+[\mathbf{a}]_2^2[\mathbf{b}]_3^2-[\mathbf{b}]_2^2\hat{h}_x^2-[\mathbf{b}]_3^2\hat{h}_x^2 \\
&\quad +[\mathbf{b}]_1^2\left([\mathbf{a}]_2^2+[\mathbf{a}]_3^2-\hat{h}_x^2\right) \\
&\quad +2([\mathbf{a}]_2[\mathbf{b}]_2+[\mathbf{a}]_3[\mathbf{b}]_3)\hat{h}_x\hat{h}_y - ([\mathbf{a}]_1^2+[\mathbf{a}]_2^2+[\mathbf{a}]_3^2)\hat{h}_y^2 \\
&\quad -2[\mathbf{a}]_1[\mathbf{b}]_1\left([\mathbf{a}]_2[\mathbf{b}]_2+[\mathbf{a}]_3[\mathbf{b}]_3-\hat{h}_x\hat{h}_y\right)\Big)\Big\}^{\frac{1}{2}}, \\
\chi_3 &= \left\{[\mathbf{b}]_1^2([\mathbf{a}]_2^2+[\mathbf{a}]_3^2)+([\mathbf{b}]_2[\mathbf{a}]_3-[\mathbf{a}]_2[\mathbf{b}]_3)^2-2[\mathbf{a}]_1[\mathbf{b}]_1([\mathbf{a}]_2[\mathbf{b}]_2+[\mathbf{a}]_3[\mathbf{b}]_3)+[\mathbf{a}]_1^2([\mathbf{b}]_2^2+[\mathbf{b}]_3^2)\right\} \\
&\quad \cdot([\mathbf{b}]_1[\mathbf{a}]_3-[\mathbf{a}]_1[\mathbf{b}]_3), \\
\chi_4 &= [\mathbf{b}]_1^2[\mathbf{a}]_2\hat{h}_x + [\mathbf{a}]_2[\mathbf{b}]_3^2\hat{h}_x + [\mathbf{b}]_2([\mathbf{a}]_1^2+[\mathbf{a}]_3^2)\hat{h}_y - [\mathbf{a}]_1[\mathbf{b}]_1\left([\mathbf{b}]_2\hat{h}_x+[\mathbf{a}]_2\hat{h}_y\right) - [\mathbf{a}]_3[\mathbf{b}]_3\left([\mathbf{b}]_2\hat{h}_x+[\mathbf{a}]_2\hat{h}_y\right), \\
\chi_5 &= [\mathbf{b}]_1^2([\mathbf{a}]_2^2+[\mathbf{a}]_3^2)+([\mathbf{b}]_2[\mathbf{a}]_3-[\mathbf{a}]_2[\mathbf{b}]_3)^2-2[\mathbf{a}]_1[\mathbf{b}]_1([\mathbf{a}]_2[\mathbf{b}]_2+[\mathbf{a}]_3[\mathbf{b}]_3)+[\mathbf{a}]_1^2([\mathbf{b}]_2^2+[\mathbf{b}]_3^2), \\
\mathbf{a} &= [\sin(\alpha_x)\cos(\beta_x),\ \sin(\alpha_x)\sin(\beta_x),\ \cos(\alpha_x)], \\
\mathbf{b} &= [\sin(\alpha_y)\cos(\beta_y),\ \sin(\alpha_y)\sin(\beta_y),\ \cos(\alpha_y)].
\end{aligned}$$

Both the magnitude and the phase of the first two entries of $\mathbf{a}_{\text{gen}}$ offer information on u and v. Analogous to $\{e\}$ in Section 4.2.2,

$$(\hat{u}, \hat{v}) = \begin{cases} (\mathrm{s}_u^o\hat{u}_{\text{mag}}, \mathrm{s}_v^o\hat{v}_{\text{mag}}), & \text{if } \left\|\mathbf{a}\left(\mathrm{s}_u^o\hat{u}_{\text{mag}}, \mathrm{s}_v^o\hat{v}_{\text{mag}}\right)^H\mathbf{E}_n\right\|_2 < \left\|\mathbf{a}\left(\acute{u}, \acute{v}\right)^H\mathbf{E}_n\right\|_2^2 \\ (\acute{u}, \acute{v}), & \text{if } \left\|\mathbf{a}\left(\mathrm{s}_u^o\hat{u}_{\text{mag}}, \mathrm{s}_v^o\hat{v}_{\text{mag}}\right)^H\mathbf{E}_n\right\|_2 > \left\|\mathbf{a}\left(\acute{u}, \acute{v}\right)^H\mathbf{E}_n\right\|_2^2 \end{cases}. \quad (4.27)$$

The azimuth/elevation arrival angles may then be estimated as in (4.11) and (4.12).

Hence, the arbitrarily spread (but still orthogonal) tri-axial velocity sensor may be used with any eigen-based parameter-estimation algorithm for two-dimensional direction finding. This proposed scheme may apply to a single tri-axial velocity sensor, or to an array consisting of multiple tri-axial velocity sensors. [4] [5]

4.4 Monte Carlo Simulations to Verify the Proposed Scheme's Efficacy

The proposed scheme may be used with *any* eigen-based parameter estimation algorithm, to estimate the emitters' azimuth/elevation angles of arrival. To illustrate how, this section will adopt the "Uni-Vector-Hydrophone ESPRIT" algorithm of [53], which was originally developed for a four-component acoustic vector sensor with all its component sensors collocating in a point-like geometry. To adopt [53] to the spatially spread tri-axial velocity sensor, simply replace equations (15)-(17) of [53] by the procedure proposed in Section 4.3 of the present work. [6]

Monte Carlo simulations are conducted to verify the proposed scheme's efficacy and aperture extension, despite its irregular array configuration. The following settings are used: $\alpha_x = 85^\circ$, $\beta_x = 5^\circ$, $\alpha_y = 95^\circ$, $\beta_y = 80^\circ$, $\Delta = \Delta_x = \frac{5}{6}\Delta_y$. There exist two pure tone signals, at digital frequencies $f_1' = 0.46$ and $f_2' = 0.36$, respectively with deterministic complex phases φ_1 and φ_2 that are randomly generated for each Monte Carlo experiment from a uniform distribution over $[0, 2\pi)$. These two signals impinge respectively from $(\theta_1, \phi_1) = (130^\circ, 50^\circ)$ and $(\theta_2, \phi_2) = (45^\circ, -135^\circ)$. All incident signals have unity power. The additive noise is Gaussian, zero mean, white spatio-temporally, with a known power of $\sigma^2 = 25$dB.

Figure 4.4(a) plots the "composite root mean square error" (CRMSE) [7]of the first source's three Cartesian direction cosine estimates, versus the spacing parameter $\frac{\Delta}{\lambda_{\min}}$, with $\lambda_{\min}$ referring to the shortest wavelength among all incident sources' wavelengths. This "composite root mean square error" is defined as $\frac{1}{I}\sum_{i=1}^{I}\sqrt{\frac{\delta_{u,k,i}^2+\delta_{v,k,i}^2}{2}}$, where $\delta_{u,k,i}$ ($\delta_{v,k,i}$) denotes the error in estimating the kth source's x-axis (y-axis) direction cosine at the ith Monte Carlo experiment. Each figure's every icon represents $I = 1000$ statistically independent Monte Carlo experiments, each of which involves 80 temporal snapshots.

[4] This arbitrarily spread case would degenerate to the simple case in Section 3.2 if $\alpha_x = \pi/2$ and $\beta_x = 0$. Then, (4.19) would degenerate to (4.5), and (4.20) would degenerate to (4.6).

[5] If $\Delta_x = \Delta_y = 0$ in (4.13), this arbitrarily spread case will degenerate to the case where the three uni-variate velocity sensors are all collocated. Then, (4.19)-(4.27) would no longer hold. Instead, ϕ and θ may estimated simply via (4.11)-(4.12) with $\hat{u}$ ($\hat{v}$) replaced by p_x (p_y).

[6] The proposed scheme can handle data models other than that in [53]. This section's simulations serve only as an illustrative example. For instance, wideband data could first be segmented via a sliding time-domain window, then processed by a "short time discrete Fourier transform" (ST-DFT), before each DFT-component is individually processed.

[7] The estimation bias is roughly an order of magnitude below the corresponding estimation standard deviation, hence not shown.

Figure 4.4(b) does the same for the second source.

Figures 4.4(a) and 4.4(b) together demonstrate that the proposed scheme successfully resolves the two incident emitters, even if the three uni-axial velocity sensors are not collocated, but spaced apart, sparsely. The collocated case (i.e. $\Delta = 0$) has its estimation error indicated in these figures by a horizontal dotted line, to ease comparison with the proposed scheme's performance. The proposed scheme's CRMSE drops by about an order-of-magnitude, as Δ increases (for the proposed scheme) by an order-of-magnitude from $\frac{\Delta}{\lambda_{\min}} = 10^0$ to $\frac{\Delta}{\lambda_{\min}} = 10^1$. Incidentally, this *ESPRIT*-based estimation approximates the Cramér-Rao lower bound, to the extent that the parameter estimation algorithm of *ESPRIT* can do so.

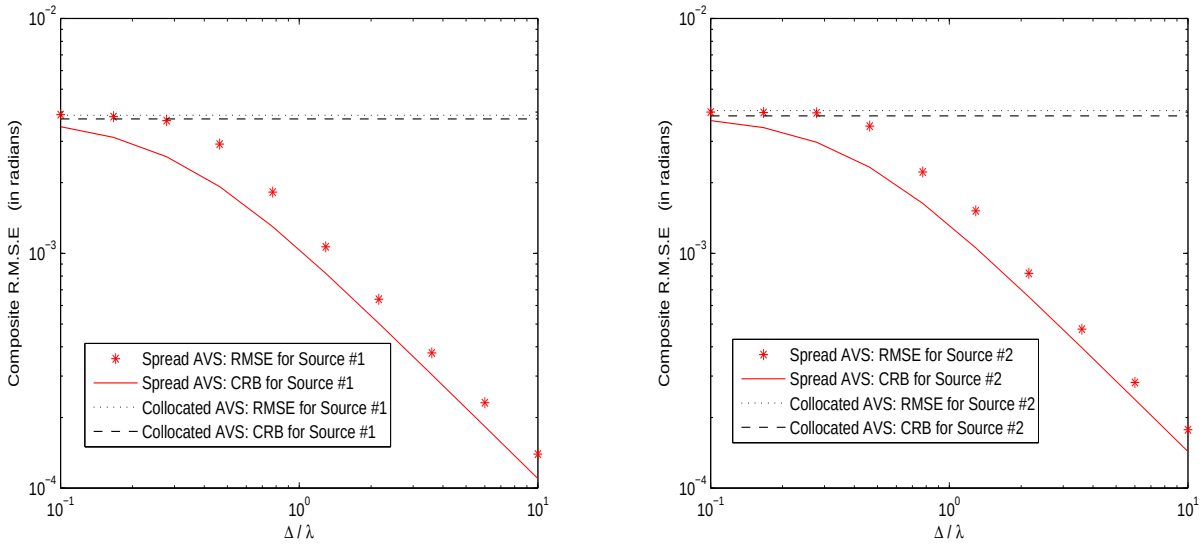

Figure 4.4: Monte Carlo simulations verifying the aperture extension efficacy of the proposed scheme for an arbitrarily spread tri-axial velocity sensor.

4.5 Overview of the Proposed Algorithm

The main steps of the algorithm can be summarized as follows:

1. adopt "Uni-Vector-Hydrophone ESPRIT" algorithm of [53] to estimate sources' steering vectors

2. estimate the non-cartesian direction-cosines, h_x, h_y
   {i} low-variance estimate of h_x, but with 2π cyclic ambiguity, is obtain by (4.19),
   {ii} high-variance estimate of h_x, but with *no* 2π cyclic ambiguity, is obtain by (4.20),
   {iii} use {ii} to resolve 2π cyclic ambiguity in {i} by (4.21),
   {iv} resolve sign ambiguity by (4.22),
   {v} apply (4.19)-(4.22) for h_y,
   {vi} h_x, h_y are estimated by (4.23)-(4.24),

3. the estimates of the Cartesian direction-cosines (u, v) from phase factors h_x, h_y, can be obtained from (4.26), denoted as $(\acute{u}, \acute{v})$.

4. the estimates of the Cartesian direction-cosines (u, v) are also available from magnitudes of (4.15)-(4.16), denoted as $(\hat{u}_{\text{mag}}, \hat{v}_{\text{mag}})$.

5. determine between $(\acute{u}, \acute{v})$ and $(\hat{u}_{\text{mag}}, \hat{v}_{\text{mag}})$, which should be used by (4.27)

6. estimate azimuth-angle ϕ and elevation-angle θ, by (4.11)-(4.12)

4.6 Summary

The *collocating* tri-axial velocity sensor has been used in many eigen-based closed-form algorithms to estimate the azimuth/elevation direction of arrival. This work shows how those earlier eigen-based closed-form algorithms can be modified to apply to any *arbitrarily spread* tri-axial velocity sensor, even if the three uni-axial velocity sensors are placed anywhere in three-dimensional space, thereby extending their spatial aperture from a point to span a large aperture, refining the tri-axial velocity sensor's azimuth/elevation resolution.

If this tri-axial velocity sensor is accompanied by a pressure sensor, the scheme in Chapter 3 can be used instead. There, the isotropic pressure sensor can serve as a phase reference, facilitating the three uni-axial velocity sensors' relative complex phases be estimated. However, the above approach is not viable in the present work with*out* any pressure sensor. Instead, the presently proposed algorithm exploits the fact that a tri-axial velocity sensor's data must have a Frobenius norm that is *in*dependent of the incident emitter's azimuth/elevation direction of arrival and that is *in*dependent of the incident signal's frequency.

There exists an electromagnetic counterpart [156], which is predicated on an electric dipole's and a magnetic loop's magnitude responses and phase responses, which differ principally from those in (4.1) and (4.13) for the acoustic tri-axial velocity sensor presently under study. On account of the fundamental disparity between acoustics and electromagnetics, the algorithmic steps and the allowable array configurations are basically different between the present work and [156].

Chapter 5

"Blind" Calibration of an Array of Acoustic Vector-Sensors Suffering Gain Errors / Mis-Location / Mis-Orientation

[1]

5.1 Literature Review of Relevant Calibration Algorithms

While the open literature contains many array-calibration algorithms, they are not tailored to the acoustic vector-sensor, in *not* exploiting any uniqueness of the acoustic vector-sensor's distinctive array manifold.

This presently proposed "blind calibration" algorithm relates to (but advances beyond) a class of array-calibration/direction-finding algorithms [57, 64, 95, 96, 152] for an array of **ideal** subarrays suffering from *non*-ideal inter-subarray relationships. [2]

1. [57, 152] assume these subarrays to have perfectly known gain response, phase response, linear geometry, and identical orientation; only the inter-subarray spacings need calibration.

2. [64] relaxes the assumptions in [57] to allow uncertainties in gain/phase between different subarrays (but not within any subarray), as well as an arbitrary (but a priori known) orientation for each subarray.

3. [95] further relaxes the assumptions in [64] to allow inter-subarray mis-orientations, which (unlike the present work) is nonetheless limited to one dimensional rotation

[1] This chapter is taken from [163], jointly authored by the candidate, his chief supervisor, and Dr. Fangjiong CHEN.

[2] [75] allows gain/phase uncertainties within any subarray, but no mis-orientation and no dislocation across subarrays.

on the azimuthal plane, but not the full trivariate Euler angles for three-dimensional mis-orientation allowed in the present work. [3]

In contrast to the above limited set of non-idealities, this present work explicitly calibrates the *intra*-subarray idealities – i.e., each vector-sensor's non-ideal gain-responses – in addition to the *inter*-subarray mis-locations and *inter*-subarray mis-orientation. In sea/field deployment, it could be difficult to place/keep every vector-sensor at its nominal orientation and location. GPS could correct gross errors, but fine deviations may remain, and could significantly degrade the overall array's performance. That is, *inter*-vector-sensor mis-orientations and dislocations likely occur in the sea/field deployment and require calibration. On the other hand, during the manufacturing/assembly process in the factory, *intra*-vector-sensor non-idealities could be more easily avoided and corrected. The vector-sensor's component-sensors (namely, the three uni-axial velocity-sensors and one pressure-sensor) are physically fused together and are fixated to a supporting frame, during the manufacturing/assembly process. Hence, *intra*-vector-sensor mis-orientation and dislocation could be reduced in the design/manufacturing process to within specified precision, or at least be calibrated in the factory during the quality-assurance inspection stage.

A few algorithms [129, 144, 145, 151] are devised for the acoustic vector-sensor, but they all (unlike the present work)

1) perform *aided* calibration (as opposed to "blind" calibration"), necessitating cooperative emitters to impinge from prior known directions-of-arrival (and perhaps with prior known magnitudes).

2) neglect any *inter*-vector-sensor dislocation.

Furthermore, [144, 145, 151] (also unlike the present work) can*not* handle three-dimensional mis-orientation.

For "blind" calibration[4] of acoustic vector-sensors, the present work is first to the open literature (to the best of the present authors' knowledge),

a) to "blindly" calibrate acoustic vector-sensors.

b) to calibrate ("blindly" or otherwise) the *intra*-vector-sensor gain-uncertainties.

c) to require no iterative search and no exhaustive search, in calibrating the acoustic vector-sensors.

d) to be computationally very efficient in calibrating acoustic vector-sensors - computationally *orders-of-magnitude* more efficient than by maximum-likelihood estimation. The presently proposed algorithm breaks the original non-linear optimization problem, from a high dimension into several optimization problems, that are of much

[3] On the other hand, [96] generalizes [57] by allowing intra-subarray mutual coupling but not the relaxed assumptions in [64] and [95]. This mutual coupling consideration is irrelevant to the present investigation, as *acoustic* sensors suffer no mutual coupling.

[4] "Blind" calibration means the unavailability of any calibrating source of prior known arrival direction.

lower dimensions and that can each be solved as a set of linear equations, thereby facilitating much faster and more likely convergence to the global optimum.

The above are achieved via an interplay between two distinct but complementary approaches of direction finding:

(A) The (customary) interferometry approach: The spatial phase delay between two spatially displaced vector-sensors encapsulates the information on the directions-of-arrival of the incident sources.

(B) The approach via "particle-velocity-field vector normalization"[26]: A vector-sensor's constituent particle-velocity-sensors and/or pressure-sensor give the incident particle-velocity vector, whose normalization (to unity Frobenius norm) produces the incident source's three Cartesian direction-cosines and thus the azimuth-elevation arrival-angles. Both the azimuth-angles and the elevation-angles may thus be estimated and automatically matched with only one vector-sensor.

5.2 Mathematical Modeling of Gain / Mis-Location / Mis-Orientation Non-Idealities in an Acoustic Vector-Sensor

The array manifold in (1.2) is ideal, in presuming perfect gain-responses as well as in presuming perfect conformity to the nominal locations and the nominal orientations. If such hypothetical ideality is violated by the ℓth vector sensor,[5] its array-manifold would become

$$\mathbf{a}_k^{(\ell)} = \mathbf{J}^{(\ell)}\ \mathbf{G}\left(\mathcal{G}^{(\ell)}\right)\ \tilde{\mathbf{R}}\left(\tilde{\theta}^{(\ell)},\tilde{\gamma}^{(\ell)},\tilde{\phi}^{(\ell)}\right)\begin{bmatrix} u_k \\ v_k \\ w_k \\ 1 \end{bmatrix} q_k^{(\ell)} e^{j\frac{2\pi f_k}{c}\left\{u_k\Delta_x^{(\ell)}+v_k\Delta_y^{(\ell)}+w_k\Delta_z^{(\ell)}\right\}} \tag{5.1}$$

$$\mathbf{J}^{(\ell)} = \begin{cases} \mathrm{diag}\{1,1,1,1\}, & \text{for a four-component "complete" vector-sensor} \\ \mathrm{diag}\{1,1,1,0\}, & \text{if the pressure-sensor is absent.} \end{cases} \tag{5.2}$$

In the above,

1. the *intra*-vector-sensor gain deviation is represented by a 4×4 diagonal matrix,

$$\mathbf{G}\left(\mathcal{G}^{(\ell)}\right) = \mathrm{diag}\left\{g_x^{(\ell)},g_y^{(\ell)},g_z^{(\ell)},g_p^{(\ell)}\right\}. \tag{5.3}$$

2. the mis-orientation is represented by a 4×4 diagonal matrix,

$$\tilde{\mathbf{R}}\left(\tilde{\theta}^{(\ell)},\tilde{\gamma}^{(\ell)},\tilde{\phi}^{(\ell)}\right) = \mathrm{diag}\left\{\mathbf{R}\left(\tilde{\theta}^{(\ell)},\tilde{\gamma}^{(\ell)},\tilde{\phi}^{(\ell)}\right),1\right\}, \tag{5.4}$$

[5]Inter-vector-sensor mis-location and mis-orientation may more likely occur, if the acoustic vector-sensors are deployed far apart, as on a sparse array-grid.

where

$$\mathbf{R}\left(\tilde{\theta}^{(\ell)},\tilde{\gamma}^{(\ell)},\tilde{\phi}^{(\ell)}\right) = \begin{bmatrix} \cos\tilde{\phi}^{(\ell)} & \sin\tilde{\phi}^{(\ell)} & 0 \\ -\sin\tilde{\phi}^{(\ell)} & \cos\tilde{\phi}^{(\ell)} & 0 \\ 0 & 0 & 1 \end{bmatrix} \begin{bmatrix} 1 & 0 & 0 \\ 0 & \cos\tilde{\gamma}^{(\ell)} & \sin\tilde{\gamma}^{(\ell)} \\ 0 & -\sin\tilde{\gamma}^{(\ell)} & \cos\tilde{\gamma}^{(\ell)} \end{bmatrix} \begin{bmatrix} \cos\tilde{\theta}^{(\ell)} & 0 & -\sin\tilde{\theta}^{(\ell)} \\ 0 & 1 & 0 \\ -\sin\tilde{\theta}^{(\ell)} & 0 & \cos\tilde{\theta}^{(\ell)} \end{bmatrix}. \tag{5.5}$$

Any mis-orientation in three-dimensional space may be represented by (5.5), which involves three sequential rotations: 1) a rotation by an angle of $\tilde{\theta}^{(\ell)}$ on the x-z plane, 2) then a second rotation by an angle of $\tilde{\gamma}^{(\ell)}$ on the y-z plane, and 3) lastly a third rotation by an angle of $\tilde{\phi}^{(\ell)}$ on the x-y plane.

3. $q_k^{(\ell)} = e^{j\frac{2\pi f_k}{c}(x^{(\ell)}u_k+y^{(\ell)}v_k+z^{(\ell)}w_k)}$ represents the kth source's *spatial* phase factor, relating the ℓth vector-sensor's *nominal* location $\left(x^{(\ell)},y^{(\ell)},z^{(\ell)}\right)$ to the reference-location of $(0,0,0)$, with f_k denoting the kth narrowband source's center-frequency, and c symbolizing the propagation speed.

4. $e^{j\frac{2\pi f_k}{c}\left\{u_k\Delta_x^{(\ell)}+v_k\Delta_y^{(\ell)}+w_k\Delta_z^{(\ell)}\right\}}$ corresponds to the kth source's spatial phase-factor relating the ℓth vector-sensor's *nominal* location $\left(x^{(\ell)},y^{(\ell)},z^{(\ell)}\right)$ and *actual* location $\left(x^{(\ell)}+\Delta_x^{(\ell)},y^{(\ell)}+\Delta_y^{(\ell)},z^{(\ell)}+\Delta_z^{(\ell)}\right)$. Each acoustic vector-sensor may be arbitrarily mis-located as a unit. However, within each acoustic vector-sensor, individual component-sensors suffer no *intra*-vector-sensor dislocation, but remain collocated within each acoustic vector-sensor. This assumption is reasonable, because the *intra*-vector-sensor collocation can be readily assured during the manufacturing process in a factory, than any precise *inter*-vector-sensor spacing-grid during deployment in the field.

To ease subsequent exposition, define $\mathcal{G}^{(\ell)}=\left\{g_x^{(\ell)},g_y^{(\ell)},g_z^{(\ell)},g_p^{(\ell)}\right\}$, and $\mathit{\Delta}^{(\ell)}=\left\{\Delta_x^{(\ell)},\Delta_y^{(\ell)},\Delta_z^{(\ell)}\right\}$. These, along with $\tilde{\theta}^{(\ell)}$, $\tilde{\gamma}^{(\ell)}$ and $\tilde{\phi}^{(\ell)}$, constitute the ℓth vector-sensor's deterministic, unknown, to-be-calibrated non-ideality parameters.

If $g_x^{(\ell)}=g_y^{(\ell)}=g_z^{(\ell)}=g_p^{(\ell)}=1$ and $\tilde{\theta}^{(\ell)}=\tilde{\gamma}^{(\ell)}=\tilde{\phi}^{(\ell)}=\Delta_x^{(\ell)}=\Delta_y^{(\ell)}=\Delta_z^{(\ell)}=0$, then the ℓth non-ideal array manifold (5.1) would degenerate to the ideal array manifold of (1.2).

Of the L vector-sensors deployed, one must serve as a reference unit, to be indexed at $\ell=1$ and to be located exactly at $\left(x^{(1)},y^{(1)},z^{(1)}\right)=(0,0,0)$, without loss of generality. This first vector-sensor, by definition, is to suffer no mis-location and no mis-orientation (i.e., $\mathit{\Delta}^{(1)}$ has all zero entries), with $g_p^{(1)}$ prior known, but $g_x^{(1)},g_y^{(1)},g_z^{(1)}$ may remain arbitrary and unknown. If this reference acoustic vector-sensor has no pressure-sensor, then prior knowledge is needed of g_x,g_y,g_z and of which hemisphere each source impinges from. (Regarding this presumed existence of a *reference*-vector-sensor with a priori known orientation and location: This amounts to only a prior known coordinate system for the overall array. This requirement is common to all measurement systems.)

Stacking all L vector-sensors' individual steering vectors, the entire array may be characterized by the $4L \times 1$ steering vector,

$$\mathbf{a}_k \;=\; \left[\left(\mathbf{a}_k^{(1)}\right)^T, \cdots, \left(\mathbf{a}_k^{(L)}\right)^T\right]^T.$$

The subsequently proposed vector-sensor array "blind" calibration algorithm will consist of these five steps, to be developed in details in Sections 5.4 to 5.8 below.

Step #1 Section 5.4 will estimate the K incident sources' individual steering-vectors, in order to allow subsequent steps to exploit the vector-sensor array-manifold's unique characteristics.

Step #2 Section 5.5 will "blindly" calibrate each $3L$ *velocity*-sensor's gain-uncertainty, by exploiting each velocity-sensor's correspondence to a Cartesian direction-cosine of an incident source.

Step #3 Section 5.6 will estimate each incident source's azimuth-elevation direction-of-arrival, by exploiting the vector-sensor's array-manifold as the incident pressure-wavefield's spatial gradient.

Step #4 Section 5.7 will "blindly" calibrate all $L-1$ (non-reference) vector-sensors' individual mis-orientation, by again exploiting the vector-sensor's array-manifold as the incident pressure-wavefield's spatial gradient.

Step #5 Section 5.8 will calibrate all $L-1$ (non-reference) vector-sensors' individual displacements from their nominal grids.

5.3 Measurement Data Model

Let there be $K \geq 3$ number of incident signals. [6] At the ℓth vector-sensor, the following $M_\ell \times 1$ data-vector is received at time t:

$$\mathbf{z}^{(\ell)}(t) \;=\; \sum_{k=1}^{K} \mathbf{a}_k^{(\ell)} s_k(t) + \mathbf{n}(t). \tag{5.6}$$

The proposed "blind" calibration method could be applied to wide classes of incident signals. As illustration, the following three special cases will be explain in details subsequently:

1. Pure-tone signals: The kth signal is a pure tone $s_k(t) = \sqrt{\mathcal{P}_k} e^{j(2\pi f_k t + \varphi_k)}$, at frequency f_k, distinct from the other $K-1$ frequencies, and at a uniformly distributed random phase of φ_k statistically independent from all $\varphi_\ell \neq \varphi_k$. Please see the details in Sections 5.4.1 and 5.9.1.

[6] If f_k is a priori unknown $\forall k$, then it is required that $K \leq \min\{M_\ell, \forall \ell\}$. If all prior known, then no upper limit needs be imposed on K, because a bandpass filter could then be constructed to separate each pure tone from all other pure tones.
For each step, minimum required/allowed number of sources is 3. No limits for the maximum required/allowed number of sources.

2. Narrowband (not pure-tone) random signals that each has a subband unoccupied overlapped by all other incident signals: The kth incident signal's aforementioned non-overlapping subband is centered at f_k. The kth incident signal is $s_k(t) = \sqrt{\mathcal{P}_k}a_k(t)e^{j(2\pi f_k t+\varphi_k)}$, where $a_k(t)$ represent the subbanded signal's envelope, which changes only slowly with respect to the carrier period $1/f_k$. Please see the details in Sections 5.4.2 and 5.9.1.

3. Narrowband (not pure-tone) random signals, all occupying the same spectrum over the same duration: The kth incident signal is given by $s_k(t) = \sqrt{\mathcal{P}_k}a_k(t)e^{j(2\pi f_o t+\varphi_k)}$, where $a_k(t)$ represents the kth source's signal envelope, which changes only slowly with respect to the carrier period $1/f_o = 1/f_k, \forall k$. Please see the details in Sections 5.4.3 and 5.9.1.

Moreover, $\mathcal{P}_k$ denotes the signal power (a priori unknown to the receiver); φ_k signifies a random phase (uncorrelated to all other random entities). It is further assumed that $(\theta_k, \phi_k) \neq (\theta_j, \phi_j), \forall k \neq j \in \{1, \cdots, K\}$. The additive noise $\mathbf{n}(t)$ is modeled as zero mean, spatio-temporally uncorrelated, with (a priori unknown) power $\mathcal{P}_N$.

The present calibration problem aims to estimate all aforementioned array-manifold non-ideality parameters plus the sources' arrival-angles, given the $M \times N$ collected data $\mathbf{Z} = [\mathbf{z}(T_s), \mathbf{z}(2T_s), \cdots, \mathbf{z}(NT_s)]$, where $M = \sum_{\ell=1}^{L} M_\ell$, $N > 2M + 1$ [7] and T_s symbolizes the a priori known time-sampling period. [8]

The above data model is parameterized by $2K+10L-7$ number of unknown real-value scalars:

a) $2K$ number of unknown direction-of-arrival scalars,

b) $3(L-1)$ number of unknown mis-orientation scalars,

c) $3(L-1)$ number of unknown mis-location scalars, and

d) $4L-1$ number of unknown gain-uncertainty scalars.

On the other hand, there exist $4KL$ number of constraints from the $4KL$ real-value scalar measurements at any time instant. For a unique estimation of the directions-of-arrival and the non-ideality parameters, it is necessary that

$$K \;\geq\; \frac{1}{2}\left(\frac{10L-7}{2L-1}\right) \qquad \Leftrightarrow \qquad \begin{cases} K \geq 2, & \text{if } L = 1, \\ K \geq 3, & \text{if } L > 1. \end{cases} \tag{5.7}$$

The above inequality compares the number of nonlinear constraints versus the number of unknown scalars, by considering all L acoustic vector-sensors as a whole. [9] [10]

[7] For a justification of this inequality, please refer to [53].

[8] The proposed algorithm also works for narrowband signals having nonzero bandwidths, if each signal has a prior known subband wherein only that signal exists

[9] The presently proposed approach, however, would need at least three sources, (i.e. $K \geq 3$), even if $L = 1$. Otherwise, these subsequent equations cannot be solved: (5.19), (5.20), (5.21), (5.26), and (5.33).

[10] The proposed algorithm allows the reference-unit to have either all 4 component-sensors or only the 3 velocity-sensors; the latter case would require prior knowledge of g_x, g_y, g_z and would require (for the algorithmic step in (5.18)) a prior knowledge of which hemisphere in which each incident source lies.

With more separable sources, the data could yield more (nonlinear) constraints to estimate each acoustic vector-sensor's non-ideal parameters and direction-of-arrival.

5.4 Proposed Algorithm's Step #1: Estimation of Each Source's Steering-Vector

This step estimates, for all L vector-sensors, each incident source's $M \times 1$ steering vector $\{\mathbf{a}_k, \forall k = 1, 2, \cdots, K\}$, to within an (unknown) complex-value constant. These steering-vector estimates (though ambiguous), would allow the subsequent steps to exploit the salient attributes of the vector-sensor array-manifold for "blind" array calibration. This steering-vector estimation is achieved by computing the principal eigenvector of a data correlation matrix (to be formed suitably as explained below).

This step may be realized by various approaches, in order to fit the incident sources' spectra and statistics. As illustrations, three common cases will be considered below: Section 5.4.1 will handle pure-tone signals. Section 5.4.2 will deal with narrowband signals, each with a subband unoccupied by all other incident signals. Section 5.4.3 will investigate narrowband signals, all of which occupy the same band during the same time period. In any case, this algorithmic step #1 is unaffected by the presence/absence of any pressure-sensor in any of the L vector-sensors.

5.4.1 For the special case of pure-tone signals

The "multiple pure tones" signal model may be handled by the "Uni-Vector-Hydrophone ESPRIT" method [53], which exploits each pure-tone's temporal "invariance" over the sampling instants $\{T_s, 2T_s, \cdots, NT_s\}$. The following will summarize the algorithmic steps of this *Uni-Vector-Hydrophone ESPRIT* algorithm. For the motivations underlying these algorithmic steps, please refer to the lengthy exposition in [53] itself.

{1} Form an $M \times N$ data-matrices $\mathbf{Z}_1 = [\mathbf{z}(T_s), \mathbf{z}(2T_s), \cdots, \mathbf{z}((N-1)T_s)]$ and $\mathbf{Z}_2 = [\mathbf{z}(2T_s), \mathbf{z}(3T_s), \cdots, \mathbf{z}(NT_s)]$. Then, form a $2M \times N$ data-matrix $\mathbf{Z} = [\mathbf{Z}_1^T, \mathbf{Z}_2^T]^T$

{2} Eigen-decompose $\mathbf{Z}\mathbf{Z}^H$, such that $\mathbf{E}_s = [\mathbf{E}_1^T, \mathbf{E}_2^T]^T$ is a $2M \times K$ matrix (the signal-subspace eigenvector matrix), whose K columns are the K principal eigenvectors associated with the K largest-magnitude eigenvalues.

{3} Define the $K \times K$ matrix,

$$\mathbf{\Psi} \stackrel{\text{def}}{=} \left(\mathbf{E}_1^H \mathbf{E}_1\right)^{-1} \left(\mathbf{E}_1^H \mathbf{E}_2\right) = \mathbf{T}^{-1} \mathbf{\Phi} \mathbf{T},$$

where the kth eigenvalue of $\mathbf{\Psi}$ equals $\left\{[\mathbf{\Phi}]_{k,k} = e^{j2\pi f_k \triangle_T}, \ \ \forall k = 1, \ldots, K\right\}$, and the corresponding right-eigenvector constitutes the kth column of $\mathbf{T}$.

{4} The K impinging sources' steering-vectors may be estimated, each to within a

complex-value multiplicative scalar, as

$$\begin{aligned}[\hat{\mathbf{a}}_1, \cdots, \hat{\mathbf{a}}_K] &= \frac{1}{2}\left\{\mathbf{E}_1\mathbf{T}^{-1} + \mathbf{E}_2\mathbf{T}^{-1}\mathbf{\Phi}^{-1}\right\} \\ &= [c_1\mathbf{a}_1, \cdots, c_K\mathbf{a}_K]\,. \end{aligned} \tag{5.8}$$

These K *unknown* complex-value multiplicative scalars $c_1, \ldots, c_K$ arise from the eigen-decomposition of $\mathbf{\Psi}$.

5.4.2 For the special case of narrowband random signals, each with a subband unoccupied by any other incident signal

Suppose that the kth signal's non-overlapping sub-spectrum is centered at f_k. Comb-filter the $M \times N$ received data matrix $\mathbf{Z} = [\mathbf{z}(T_s), \mathbf{z}(2T_s), \cdots, \mathbf{z}(NT_s)]$ around f_k, to isolate the kth narrowband spectrum, to produce an $M \times N$ data matrix $\mathbf{Z}_k$. Then, eigen-decompose $\mathbf{Z}_k\mathbf{Z}_k^H$, such that $\mathbf{E}_{s_k}$ is the $M \times 1$ eigenvector associated with the largest-magnitude eigenvalue. The kth impinging source's steering-vector may then be estimated, to within a complex-value multiplicative scalar, as $\hat{\mathbf{a}}_k = \mathbf{E}_{s_k}, \forall k = 1, \ldots, K$.

5.4.3 For the special case of narrowband random signals, all occupying the same band during the same period

Suppose all K incident narrowband signals are centered f_o. These signals then are not isolated at any subband, as for the cases in Sections 5.4.1 and 5.4.2. Instead, a spatial invariance is to be constructed, by presuming two reference vector-sensors sharing an identical orientation that is prior known. Without loss of generality, assume these reference vector-sensors as indexed at $\ell = 1, J$.[11]

The first algorithmic step is to eigen-decompose the data-correlation matrix $\mathbf{Z}\mathbf{Z}^H$, producing an $M \times K$ signal-subspace eigenvector matrix $\mathbf{E}_s$, whose K columns are the K principal eigenvectors associated with the K largest-magnitude eigenvalues. That is,

$$\mathbf{E}_s \approx \mathbf{A}\mathbf{T} = [\mathbf{a}_1, \cdots, \mathbf{a}_K]\,\mathbf{T}, \tag{5.9}$$

where $\mathbf{T}$ is an tentatively unknown but nonsingular $K \times K$ coupling matrix. If noiseless or if an infinite number of snapshots exist, the above approximation would become exact.

The Jth subarray may be defined as $\mathbf{A}_J \overset{\text{def}}{=} \mathbf{J}_J\mathbf{A}$, where $\mathbf{J}_J \overset{\text{def}}{=} \left[\mathbf{0}_{M_J,\sum_{i=1}^{J-1} M_i}, \mathbf{I}_{M_J}, \mathbf{0}_{M_J,\sum_{i=J+1}^{L} M_i}\right]$ symbolizes an $M_J \times M$ subarray-selection matrix, $\mathbf{0}_{m,n}$ signifies an $m \times n$ zero matrix, and $\mathbf{I}_m$ denotes an $m \times m$ identity matrix. The first subarray and the Jth subarray are

[11] As in Sections 5.4.1 and 5.4.2, the $\ell = 1$st vector-sensor serves as a reference in location, orientation, and in the gain of its pressure sensor (if present). Moreover for this signal model in Section 5.4.3, this $\ell = 1$st vector-sensor 's $g_x^{(1)}, g_y^{(1)}, g_z^{(1)}$ are also assumed as prior known; and the Jth vector-sensor's orientation, $g_p^{(J)}$, $g_x^{(J)}$, $g_y^{(J)}$, $g_z^{(J)}$ also need to be prior known. These additional assumptions are needed, in order to subsequently form the "spatial invariance" matrix of $\mathbf{\Psi}^{(J)}$.

interrelated through a "spatial invariance" matrix of $\mathbf{\Psi}^{(J)}$:

$$\begin{aligned}
&\left(\mathbf{G}\left(\mathcal{G}^{(J)}\right)\tilde{\mathbf{R}}\left(\tilde{\theta}^{(J)},\tilde{\gamma}^{(J)},\tilde{\phi}^{(J)}\right)\right)^{-1}\mathbf{A}_J \\
= &\left(\mathbf{G}\left(\mathcal{G}^{(1)}\right)\tilde{\mathbf{R}}\left(\tilde{\theta}^{(1)},\tilde{\gamma}^{(1)},\tilde{\phi}^{(1)}\right)\right)^{-1}\mathbf{A}_1 \\
&\underbrace{\begin{bmatrix} q_k^{(J)}e^{j\frac{2\pi f_k}{c}\left\{u_k\Delta_x^{(J)}+v_k\Delta_y^{(J)}+w_k\Delta_z^{(J)}\right\}} & & \\ & \ddots & \\ & & q_K^{(J)}e^{j\frac{2\pi f_K}{c}\left\{u_K\Delta_x^{(J)}+v_K\Delta_y^{(J)}+w_K\Delta_z^{(J)}\right\}} \end{bmatrix}}_{\stackrel{\text{def}}{=}\mathbf{\Phi}^{(J)}},
\end{aligned} \tag{5.10}$$

where $\left(\mathbf{G}\left(\mathcal{G}^{(J)}\right)\tilde{\mathbf{R}}\left(\tilde{\theta}^{(J)},\tilde{\gamma}^{(J)},\tilde{\phi}^{(J)}\right)\right)^{-1}$ aligns the Jth vector-sensor's orientation to the Cartesian axes and $\left(\mathbf{G}\left(\mathcal{G}^{(1)}\right)\tilde{\mathbf{R}}\left(\tilde{\theta}^{(1)},\tilde{\gamma}^{(1)},\tilde{\phi}^{(1)}\right)\right)^{-1}$ achieves the same for the first vector-sensor.

Construct the signal-subspace matrix pencil $\{\tilde{\mathbf{E}}_{s_1},\tilde{\mathbf{E}}_{s_J}\}$, where

$$\begin{aligned}
\tilde{\mathbf{E}}_{s_1} &\stackrel{\text{def}}{=} \left(\mathbf{G}\left(\mathcal{G}^{(1)}\right)\tilde{\mathbf{R}}\left(\tilde{\theta}^{(1)},\tilde{\gamma}^{(1)},\tilde{\phi}^{(1)}\right)\right)^{-1}\underbrace{\mathbf{J}_1\mathbf{E}_s}_{\approx\mathbf{A}_1\mathbf{T}}, \\
\tilde{\mathbf{E}}_{s_J} &\stackrel{\text{def}}{=} \left(\mathbf{G}\left(\mathcal{G}^{(J)}\right)\tilde{\mathbf{R}}\left(\tilde{\theta}^{(J)},\tilde{\gamma}^{(J)},\tilde{\phi}^{(J)}\right)\right)^{-1}\underbrace{\mathbf{J}_J\mathbf{E}_s}_{\approx\mathbf{A}_J\mathbf{T}}.
\end{aligned}$$

There exists a $K\times K$ nonsingular matrix $\mathbf{\Psi}^{(J)}$ relating $\tilde{\mathbf{E}}_{s_1}$ and $\tilde{\mathbf{E}}_{s_J}$, where

$$\mathbf{\Psi}^{(J)} \stackrel{\text{def}}{=} \left(\tilde{\mathbf{E}}_{s_1}^H\tilde{\mathbf{E}}_{s_1}\right)^{-1}\left(\tilde{\mathbf{E}}_{s_1}\tilde{\mathbf{E}}_{s_J}\right) = \mathbf{T}^{-1}\mathbf{\Phi}^{(J)}\mathbf{T}. \tag{5.11}$$

Therefore, $\mathbf{T}$ may be computed by eigen-decomposing $\mathbf{\Psi}^{(J)}$.

The K impinging sources' steering-vectors may be estimated, each to within a complex-value multiplicative scalar, as follows:

$$[\hat{\mathbf{a}}_1,\cdots,\hat{\mathbf{a}}_K] = \mathbf{E}_s\mathbf{T}^{-1}.$$

Again, $\mathbf{T}$ denotes a non-singular matrix containing the right-eigenvectors of $\mathbf{\Psi}^{(J)}$.

In addition to the reference (i.e. the first) vector-sensor whose array manifold is fully calibrated, the ℓth vector-sensor whose intra-vector-sensor gain deviation.

5.5 Proposed Algorithm's Step #2: "Blind" Calibration of Each Vector-Sensor's Gain-Uncertainties

Step #1 of the last section has isolated each source's steering vector, to allow the present step and the subsequent steps to exploit the vector-sensor array-manifold's unique characteristics.

Step #2 will now exploit each *velocity*-sensor's direct measurement of each Cartesian

direction-cosine. Drawing upon (5.8),

$$\left[\hat{\mathbf{a}}_k^{(\ell)}\right]_1 \approx c_k \underbrace{g_x^{(\ell)}\ u_k^{(\ell)}\ q_k^{(\ell)}\ e^{j\frac{2\pi f_k}{c}\left\{u_k\Delta_x^{(\ell)}+v_k\Delta_y^{(\ell)}+w_k\Delta_z^{(\ell)}\right\}}}_{=\left[\mathbf{a}_k^{(\ell)}\right]_1}, \tag{5.12}$$

$$\left[\hat{\mathbf{a}}_k^{(\ell)}\right]_2 \approx c_k \underbrace{g_y^{(\ell)}\ v_k^{(\ell)}\ q_k^{(\ell)}\ e^{j\frac{2\pi f_k}{c}\left\{u_k\Delta_x^{(\ell)}+v_k\Delta_y^{(\ell)}+w_k\Delta_z^{(\ell)}\right\}}}_{=\left[\mathbf{a}_k^{(\ell)}\right]_2}, \tag{5.13}$$

$$\left[\hat{\mathbf{a}}_k^{(\ell)}\right]_3 \approx c_k \underbrace{g_z^{(\ell)}\ w_k^{(\ell)}\ q_k^{(\ell)}\ e^{j\frac{2\pi f_k}{c}\left\{u_k\Delta_x^{(\ell)}+v_k\Delta_y^{(\ell)}+w_k\Delta_z^{(\ell)}\right\}}}_{=\left[\mathbf{a}_k^{(\ell)}\right]_3}, \tag{5.14}$$

$$\left[\hat{\mathbf{a}}_k^{(\ell)}\right]_4 \approx c_k \underbrace{g_p^{(\ell)}\ q_k^{(\ell)}\ e^{j\frac{2\pi f_k}{c}\left\{u_k\Delta_x^{(\ell)}+v_k\Delta_y^{(\ell)}+w_k\Delta_z^{(\ell)}\right\}}}_{=\left[\mathbf{a}_k^{(\ell)}\right]_4}, \tag{5.15}$$

[12] where the approximations are due to noises in the data model.

Each equation above represents a one-to-one correspondence between (i) an element in the ℓth vector-sensor's kth steering-vector estimate $\hat{\mathbf{a}}_k^{(\ell)}$, and (ii) a direction-cosine of the kth source amplitude-scaled by the ℓth vector-sensor's gain uncertainty. Such one-to-one correspondences would be *un*available for an array of displaced microphones, wherein the direction-cosines are embedded **between two sensors'** data, but not wholly with*in* any one sensor's individual data. That inter-sensor embedment of the direction-cosines would require more complicated signal processing in direction finding, than if via (5.12)-(5.15) above.

There remains the elimination of the unknown complex-value scalar c_k from (5.12)-(5.15). The following will first evaluate c_k.

1. If the reference vector-sensor has a pressure-sensor, (5.15) gives $\left[\hat{\mathbf{a}}_k^{(1)}\right]_4 \approx c_k \left[\mathbf{a}_k^{(1)}\right]_4$. Then, the corresponding $g_p^{(1)} = \left[\mathbf{a}_k^{(1)}\right]_4$ would need to be prior known, in order to give

$$c_k \approx \frac{\left[\hat{\mathbf{a}}_k^{(1)}\right]_4}{g_p^{(1)}}, \qquad \forall k. \tag{5.16}$$

2. If the reference vector-sensor has *no* pressure-sensor, proceed as follows:

   (i) Its velocity-sensors' $g_x^{(1)}, g_y^{(1)}, g_z^{(1)}$ would need to be prior known. From (5.12)-(5.14),

$$\begin{aligned}
\left|\left[\hat{\mathbf{a}}_k^{(1)}\right]_1\right| &\approx |c_k| g_x^{(1)} \left|u_k^{(1)}\right|, \\
\left|\left[\hat{\mathbf{a}}_k^{(1)}\right]_2\right| &\approx |c_k| g_y^{(1)} \left|v_k^{(1)}\right|, \\
\left|\left[\hat{\mathbf{a}}_k^{(1)}\right]_3\right| &\approx |c_k| g_z^{(1)} \left|w_k^{(1)}\right|.
\end{aligned}$$

[12] (5.12)-(5.15) are based on (5.1).

The above three lines have used the fact that $g_x^{(1)}$ and $g_y^{(1)}$ and $g_z^{(1)}$ are non-negative. Next, recall that $\left|u_k^{(1)}\right|^2 + \left|v_k^{(1)}\right|^2 + \left|w_k^{(1)}\right|^2 = 1$, consequentially

$$|c_k| \approx \left(\left| \frac{\left[\hat{\mathbf{a}}_k^{(1)}\right]_1}{g_x^{(1)}} \right|^2 + \left| \frac{\left[\hat{\mathbf{a}}_k^{(1)}\right]_2}{g_y^{(1)}} \right|^2 + \left| \frac{\left[\hat{\mathbf{a}}_k^{(1)}\right]_3}{g_z^{(1)}} \right|^2 \right)^{-1/2}. \tag{5.17}$$

(ii) As the reference vector-sensor is located at origin, it suffers no mis-location. From (5.12)-(5.14),

$$\begin{aligned} \left[\hat{\mathbf{a}}_k^{(1)}\right]_1 &\approx |c_k| g_x^{(1)} u_k^{(1)} e^{j\angle c_k}, \\ \left[\hat{\mathbf{a}}_k^{(1)}\right]_2 &\approx |c_k| g_y^{(1)} v_k^{(1)} e^{j\angle c_k}, \\ \left[\hat{\mathbf{a}}_k^{(1)}\right]_3 &\approx |c_k| g_z^{(1)} w_k^{(1)} e^{j\angle c_k}. \end{aligned}$$

The above three lines have exploited the fact that $\angle g_x^{(1)} = \angle g_y^{(1)} = \angle g_z^{(1)} = 0$. At least one of $\text{sign}\left(u_k^{(1)}\right)$ or $\text{sign}\left(v_k^{(1)}\right)$ or $\text{sign}\left(w_k^{(1)}\right)$ would also need to be prior known, in order to evaluate

$$\angle c_k = \begin{cases} \angle \text{sign}\left(u_k^{(1)}\right) \left[\hat{\mathbf{a}}_k^{(1)}\right]_1, & \text{if sgn}\left(u_k^{(1)}\right) \text{ is prior known;} \\ \angle \text{sign}\left(v_k^{(1)}\right) \left[\hat{\mathbf{a}}_k^{(1)}\right]_2, & \text{if sgn}\left(v_k^{(1)}\right) \text{ is prior known;} \\ \angle \text{sign}\left(w_k^{(1)}\right) \left[\hat{\mathbf{a}}_k^{(1)}\right]_3, & \text{if sgn}\left(w_k^{(1)}\right) \text{ is prior known.} \end{cases} \tag{5.18}$$

Here, sign$(\cdot)$ signifies the sign of the real-value number inside the parentheses. The above (5.17) and (5.18) together give the complex-value scalar c_k.

With $\{c_k,\ k = 1, \cdots, K\}$ thus evaluated, the gain uncertainties may be calibrated for the ℓth vector-sensor as follows: With (5.12)-(5.14),

$$\begin{aligned} \left|\left[\hat{\mathbf{a}}_k^{(\ell)}\right]_1\right| &\approx |c_k|\ g_x^{(\ell)}\ \left|u_k^{(\ell)}\right|, \\ \left|\left[\hat{\mathbf{a}}_k^{(\ell)}\right]_2\right| &\approx |c_k|\ g_y^{(\ell)}\ \left|v_k^{(\ell)}\right|, \\ \left|\left[\hat{\mathbf{a}}_k^{(\ell)}\right]_3\right| &\approx |c_k|\ g_z^{(\ell)}\ \left|w_k^{(\ell)}\right|. \end{aligned}$$

Recall that $u_k^2 + v_k^2 + w_k^2 = 1, \forall \theta_k, \phi_k$. Hence,

$$\frac{1}{|c_k|^2} \left(\left| \frac{\left[\hat{\mathbf{a}}_k^{(\ell)}\right]_1}{g_x^{(\ell)}} \right|^2 + \left| \frac{\left[\hat{\mathbf{a}}_k^{(\ell)}\right]_2}{g_y^{(\ell)}} \right|^2 + \left| \frac{\left[\hat{\mathbf{a}}_k^{(\ell)}\right]_3}{g_z^{(\ell)}} \right|^2 \right) = 1, \qquad \forall k,\ \forall \ell.$$

Note that the same c_k affects all L steering-vector estimates in $\left\{\hat{\mathbf{a}}_k^{(\ell)},\ \forall \ell\right\}$. Hence, rewrite the above in matrix form as

$$\underbrace{\begin{bmatrix} \left|\left[\hat{\mathbf{a}}_1^{(\ell)}\right]_1 / c_1\right|^2 & \left|\left[\hat{\mathbf{a}}_1^{(\ell)}\right]_2 / c_1\right|^2 & \left|\left[\hat{\mathbf{a}}_1^{(\ell)}\right]_3 / c_1\right|^2 \\ \vdots & \vdots & \vdots \\ \left|\left[\hat{\mathbf{a}}_K^{(\ell)}\right]_1 / c_K\right|^2 & \left|\left[\hat{\mathbf{a}}_K^{(\ell)}\right]_2 / c_K\right|^2 & \left|\left[\hat{\mathbf{a}}_K^{(\ell)}\right]_3 / c_K\right|^2 \end{bmatrix}}_{\stackrel{\text{def}}{=}\ \mathbf{\Psi}^{(\ell)}} \begin{bmatrix} \left(g_x^{(\ell)}\right)^{-2} \\ \left(g_y^{(\ell)}\right)^{-2} \\ \left(g_z^{(\ell)}\right)^{-2} \end{bmatrix} = \underbrace{\begin{bmatrix} 1 \\ \vdots \\ 1 \end{bmatrix}}_{\stackrel{\text{def}}{=}\mathbf{1}_K}.$$

The above $\mathbf{\Psi}^{(\ell)}$ would be full ranked for any $K \geq 3$, except at a few discrete parametric values, that would occur with probability 0 due to noises in the data model. Hence,

$$\hat{g}_x^{(\ell)} = \left[\left[\left(\mathbf{\Psi}^{(\ell)} \right)^H \mathbf{\Psi}^{(\ell)} \right]^{-1} \left(\mathbf{\Psi}^{(\ell)} \right)^H \mathbf{1}_K \right]_1^{-1/2}, \tag{5.19}$$

$$\hat{g}_y^{(\ell)} = \left[\left[\left(\mathbf{\Psi}^{(\ell)} \right)^H \mathbf{\Psi}^{(\ell)} \right]^{-1} \left(\mathbf{\Psi}^{(\ell)} \right)^H \mathbf{1}_K \right]_2^{-1/2}, \tag{5.20}$$

$$\hat{g}_z^{(\ell)} = \left[\left[\left(\mathbf{\Psi}^{(\ell)} \right)^H \mathbf{\Psi}^{(\ell)} \right]^{-1} \left(\mathbf{\Psi}^{(\ell)} \right)^H \mathbf{1}_K \right]_3^{-1/2}. \tag{5.21}$$

Specifically at $K = 3$, the simplification of $\left[\left(\mathbf{\Psi}^{(\ell)} \right)^H \mathbf{\Psi}^{(\ell)} \right]^{-1} \left(\mathbf{\Psi}^{(\ell)} \right)^H = \left(\mathbf{\Psi}^{(\ell)} \right)^{-1}$ holds.

Furthermore, if a pressure-sensor exists at the ℓth vector-sensor, (5.15) gives $\left| \left[\hat{\mathbf{a}}_k^{(\ell)} \right]_4 \right| \approx c_k \; g_p^{(\ell)}$, then

$$\hat{g}_p^{(\ell)} = \left| \frac{\left[\hat{\mathbf{a}}_k^{(\ell)} \right]_4}{c_k} \right|. \tag{5.22}$$

This step does *not* require the "reference vector-sensor" (indexed at $\ell = 1$) to be free of gain uncertainty.

5.6 Proposed Algorithm's Step #3: Estimation of Each Incident Source's Azimuth-Elevation Direction-of-Arrival

Recall that the reference vector-sensor (indexed at $\ell = 1$) suffers no mis-orientation. Taking the absolute value of the both sides of each of (5.12)-(5.14),

$$\begin{aligned} \left| u_k^{(1)} \right| &= \frac{\left| \left[\hat{\mathbf{a}}_k^{(1)} \right]_1 \right|}{|c_k| \; g_x^{(1)}}, \\ \left| v_k^{(1)} \right| &= \frac{\left| \left[\hat{\mathbf{a}}_k^{(1)} \right]_2 \right|}{|c_k| \; g_y^{(1)}}, \\ \left| w_k^{(1)} \right| &= \frac{\left| \left[\hat{\mathbf{a}}_k^{(1)} \right]_3 \right|}{|c_k| \; g_z^{(1)}}. \end{aligned}$$

On the other hand, the signs of $u_k^{(1)}$ and $v_k^{(1)}$ and $w_k^{(1)}$ may be respectively obtained as

$$\begin{aligned} \mathrm{sgn}\left(u_k^{(1)} \right) &= \mathrm{sgn}\left(\Re\left(\frac{\left[\hat{\mathbf{a}}_k^{(1)} \right]_1}{c_k} \right) \right), \\ \mathrm{sgn}\left(v_k^{(1)} \right) &= \mathrm{sgn}\left(\Re\left(\frac{\left[\hat{\mathbf{a}}_k^{(1)} \right]_2}{c_k} \right) \right), \\ \mathrm{sgn}\left(w_k^{(1)} \right) &= \mathrm{sgn}\left(\Re\left(\frac{\left[\hat{\mathbf{a}}_k^{(1)} \right]_3}{c_k} \right) \right). \end{aligned}$$

The Cartesian direction-cosines may thus be estimated as

$$\begin{bmatrix} \hat{u}_k \\ \hat{v}_k \\ \hat{w}_k \end{bmatrix} = \frac{1}{|c_k|} \begin{bmatrix} \mathrm{sgn}\left(\Re\left\{ \frac{\left[\hat{\mathbf{a}}_k^{(1)}\right]_1}{c_k} \right\} \right) & \left| \left[\hat{\mathbf{a}}_k^{(1)}\right]_1 \right| \; / \; \hat{g}_x^{(1)} \\ \mathrm{sgn}\left(\Re\left\{ \frac{\left[\hat{\mathbf{a}}_k^{(1)}\right]_2}{c_k} \right\} \right) & \left| \left[\hat{\mathbf{a}}_k^{(1)}\right]_2 \right| \; / \; \hat{g}_y^{(1)} \\ \mathrm{sgn}\left(\Re\left\{ \frac{\left[\hat{\mathbf{a}}_k^{(1)}\right]_3}{c_k} \right\} \right) & \left| \left[\hat{\mathbf{a}}_k^{(1)}\right]_3 \right| \; / \; \hat{g}_z^{(1)} \end{bmatrix}, \qquad \forall k. \quad (5.23)$$

Hence, the kth incident source's azimuth-angle and elevation-angle, respectively, may be estimated as

$$\hat{\theta}_k = \arccos \hat{w}_k, \quad (5.24)$$

$$\hat{\phi}_k = \begin{cases} \arccos \frac{\hat{u}_k}{\sin \hat{\theta}}, & \text{if } \hat{v}_k > 0, \\ -\arccos \frac{\hat{u}_k}{\sin \hat{\theta}}, & \text{if } \hat{v}_k < 0. \end{cases} \quad (5.25)$$

The presence or the absence of the pressure-sensor would make no difference to this algorithmic step #3. However, if the "reference vector-sensor" (indexed at $\ell = 1$) has no pressure-sensor, then the direction estimates in (5.24)-(5.25) would have their validity region restricted to an hemisphere.

5.7 Proposed Algorithm's Step #4: "Blind" Calibration of Each Vector-Sensor's Mis-Orientation

Given any mis-orientation at the ℓth vector-sensor, $\{u_k, v_k, w_k\}$ would appear as $\left\{u_k^{(\ell)}, v_k^{(\ell)}, w_k^{(\ell)}\right\}$, with

$$\begin{bmatrix} u_k^{(\ell)} \\ v_k^{(\ell)} \\ w_k^{(\ell)} \end{bmatrix} = \mathbf{R}\left(\tilde{\theta}^{(\ell)}, \tilde{\gamma}^{(\ell)}, \tilde{\phi}^{(\ell)}\right) \begin{bmatrix} u_k \\ v_k \\ w_k \end{bmatrix}, \qquad \forall k, \ell,$$

where the 3×3 matrix $\mathbf{R}\left(\tilde{\theta}^{(\ell)}, \tilde{\gamma}^{(\ell)}, \tilde{\phi}^{(\ell)}\right)$ has been defined in (5.5).

With K sources,

$$\underbrace{\begin{bmatrix} \hat{u}_1 & \hat{v}_1 & \hat{w}_1 \\ \vdots & \vdots & \vdots \\ \hat{u}_K & \hat{v}_K & \hat{w}_K \end{bmatrix}}_{\stackrel{\mathrm{def}}{=} \mathbf{\Gamma}^{(1)}} \left[\mathbf{R}\left(\tilde{\theta}^{(\ell)}, \tilde{\gamma}^{(\ell)}, \tilde{\phi}^{(\ell)}\right)\right]^T \approx \underbrace{\begin{bmatrix} \hat{u}_1^{(\ell)} & \hat{v}_1^{(\ell)} & \hat{w}_1^{(\ell)} \\ \vdots & \vdots & \vdots \\ \hat{u}_K^{(\ell)} & \hat{v}_K^{(\ell)} & \hat{w}_K^{(\ell)} \end{bmatrix}}_{\stackrel{\mathrm{def}}{=} \mathbf{\Gamma}^{(\ell)}},$$

where the superscript ^{T} symbolizes transposition.

If the ℓth vector-sensor contains a pressure-sensor, (5.23) holds with its superscript $^{(1)}$

substituted by $^{(\ell)}, \forall \ell$, and c_k substituted by $\left[\hat{\mathbf{a}}_k^{(\ell)}\right]_4$. Hence,

$$\begin{bmatrix} \hat{u}_k^{(\ell)} \\ \hat{v}_k^{(\ell)} \\ \hat{w}_k^{(\ell)} \end{bmatrix} = \frac{1}{|c_k|} \begin{bmatrix} \operatorname{sgn}\left(\Re\left\{\frac{\left[\hat{\mathbf{a}}_k^{(\ell)}\right]_1}{\left[\hat{\mathbf{a}}_k^{(\ell)}\right]_4}\right\}\right) & \left|\left[\hat{\mathbf{a}}_k^{(\ell)}\right]_1\right| \ / \ \hat{g}_x^{(\ell)} \\ \operatorname{sgn}\left(\Re\left\{\frac{\left[\hat{\mathbf{a}}_k^{(\ell)}\right]_2}{\left[\hat{\mathbf{a}}_k^{(\ell)}\right]_4}\right\}\right) & \left|\left[\hat{\mathbf{a}}_k^{(\ell)}\right]_2\right| \ / \ \hat{g}_y^{(\ell)} \\ \operatorname{sgn}\left(\Re\left\{\frac{\left[\hat{\mathbf{a}}_k^{(\ell)}\right]_3}{\left[\hat{\mathbf{a}}_k^{(\ell)}\right]_4}\right\}\right) & \left|\left[\hat{\mathbf{a}}_k^{(\ell)}\right]_3\right| \ / \ \hat{g}_z^{(\ell)} \end{bmatrix}, \quad \forall k, \ell.$$

If ℓth vector-sensor contains no pressure-sensor, $\left[\hat{\mathbf{a}}_k^{(\ell)}\right]_4$ would not exist; hence, $\operatorname{sgn}\left(\Re\left\{\frac{\left[\hat{\mathbf{a}}_k^{(\ell)}\right]_1}{\left[\hat{\mathbf{a}}_k^{(\ell)}\right]_4}\right\}\right)$, $\operatorname{sgn}\left(\Re\left\{\frac{\left[\hat{\mathbf{a}}_k^{(\ell)}\right]_2}{\left[\hat{\mathbf{a}}_k^{(\ell)}\right]_4}\right\}\right)$, $\operatorname{sgn}\left(\Re\left\{\frac{\left[\hat{\mathbf{a}}_k^{(\ell)}\right]_3}{\left[\hat{\mathbf{a}}_k^{(\ell)}\right]_4}\right\}\right)$ would need to be substituted by $\operatorname{sgn}(\hat{u}_k), \operatorname{sgn}(\hat{v}_k), \operatorname{sgn}(\hat{w}_k)$, respectively. Therefore,

$$\begin{bmatrix} \hat{u}_k^{(\ell)} \\ \hat{v}_k^{(\ell)} \\ \hat{w}_k^{(\ell)} \end{bmatrix} = \frac{1}{|c_k|} \begin{bmatrix} \operatorname{sgn}(\hat{u}_k) & \left|\left[\hat{\mathbf{a}}_k^{(\ell)}\right]_1\right| \ / \ \hat{g}_x^{(\ell)} \\ \operatorname{sgn}(\hat{v}_k) & \left|\left[\hat{\mathbf{a}}_k^{(\ell)}\right]_2\right| \ / \ \hat{g}_y^{(\ell)} \\ \operatorname{sgn}(\hat{w}_k) & \left|\left[\hat{\mathbf{a}}_k^{(\ell)}\right]_3\right| \ / \ \hat{g}_z^{(\ell)} \end{bmatrix}, \quad \forall k, \ell.$$

On the other hand,

$$\hat{\mathbf{R}}^{(\ell)} = \left[\left(\left(\mathbf{\Gamma}^{(1)}\right)^H \mathbf{\Gamma}^{(1)}\right)^{-1} \left(\mathbf{\Gamma}^{(1)}\right)^H \mathbf{\Gamma}^{(\ell)}\right]^T, \quad \forall \ell. \tag{5.26}$$

The above $\hat{\mathbf{R}}^{(\ell)}$ would be full ranked for any $K \geq 3$, except for parameters at a few discrete values, that would occur with probability 0 due to noises in the data model. Specifically at $K = 3$, the following simplifications hold: $\left(\left(\mathbf{\Gamma}^{(1)}\right)^H \mathbf{\Gamma}^{(1)}\right)^{-1} \left(\mathbf{\Gamma}^{(1)}\right)^H = \left(\mathbf{\Gamma}^{(1)}\right)^{-1}$, and $\hat{\mathbf{R}}^{(\ell)} = \left(\left[\mathbf{\Gamma}^{(1)}\right]^{-1} \mathbf{\Gamma}^{(\ell)}\right)^T$. However, (5.5) may be written as

$$\begin{aligned}
\left[\mathbf{R}\left(\tilde{\theta}^{(\ell)}, \tilde{\gamma}^{(\ell)}, \tilde{\phi}^{(\ell)}\right)\right]_{1,1} &= \cos\tilde{\theta}^{(\ell)} \cos\tilde{\phi}^{(\ell)} - \sin\tilde{\gamma}^{(\ell)} \sin\tilde{\theta}^{(\ell)} \sin\tilde{\phi}^{(\ell)}, \\
\left[\mathbf{R}\left(\tilde{\theta}^{(\ell)}, \tilde{\gamma}^{(\ell)}, \tilde{\phi}^{(\ell)}\right)\right]_{1,2} &= \cos\tilde{\gamma}^{(\ell)} \sin\tilde{\phi}^{(\ell)}, \\
\left[\mathbf{R}\left(\tilde{\theta}^{(\ell)}, \tilde{\gamma}^{(\ell)}, \tilde{\phi}^{(\ell)}\right)\right]_{1,3} &= \cos\tilde{\phi}^{(\ell)} \sin\tilde{\theta}^{(\ell)} + \cos\tilde{\theta}^{(\ell)} \sin\tilde{\gamma}^{(\ell)} \sin\tilde{\phi}^{(\ell)}, \\
\left[\mathbf{R}\left(\tilde{\theta}^{(\ell)}, \tilde{\gamma}^{(\ell)}, \tilde{\phi}^{(\ell)}\right)\right]_{2,1} &= -\cos\tilde{\phi}^{(\ell)} \sin\tilde{\gamma}^{(\ell)} \sin\tilde{\theta}^{(\ell)} - \cos\tilde{\theta}^{(\ell)} \sin\tilde{\phi}^{(\ell)}, \\
\left[\mathbf{R}\left(\tilde{\theta}^{(\ell)}, \tilde{\gamma}^{(\ell)}, \tilde{\phi}^{(\ell)}\right)\right]_{2,2} &= \cos\tilde{\gamma}^{(\ell)} \cos\tilde{\phi}^{(\ell)}, \\
\left[\mathbf{R}\left(\tilde{\theta}^{(\ell)}, \tilde{\gamma}^{(\ell)}, \tilde{\phi}^{(\ell)}\right)\right]_{2,3} &= \cos\tilde{\theta}^{(\ell)} \sin\tilde{\gamma}^{(\ell)} \cos\tilde{\phi}^{(\ell)} - \sin\tilde{\theta}^{(\ell)} \sin\tilde{\phi}^{(\ell)}, \\
\left[\mathbf{R}\left(\tilde{\theta}^{(\ell)}, \tilde{\gamma}^{(\ell)}, \tilde{\phi}^{(\ell)}\right)\right]_{3,1} &= -\cos\tilde{\gamma}^{(\ell)} \sin\tilde{\theta}^{(\ell)}, \\
\left[\mathbf{R}\left(\tilde{\theta}^{(\ell)}, \tilde{\gamma}^{(\ell)}, \tilde{\phi}^{(\ell)}\right)\right]_{3,2} &= -\sin\tilde{\gamma}^{(\ell)}, \\
\left[\mathbf{R}\left(\tilde{\theta}^{(\ell)}, \tilde{\gamma}^{(\ell)}, \tilde{\phi}^{(\ell)}\right)\right]_{3,3} &= \cos\tilde{\gamma}^{(\ell)} \cos\tilde{\theta}^{(\ell)},
\end{aligned}$$

where $[\cdot]_{i,j}$ denotes the (i,j)th entry of the matrix inside the square brackets. Therefore,

the ℓth vector-sensor's mis-orientation parameters can be "blindly" calibrated as

$$\hat{\theta}^{(\ell)} = \arctan\left(-\left[\hat{\mathbf{R}}^{(\ell)}\right]_{3,1} / \left[\hat{\mathbf{R}}^{(\ell)}\right]_{3,3}\right), \tag{5.27}$$

$$\hat{\gamma}^{(\ell)} = \arcsin\left(-\left[\hat{\mathbf{R}}^{(\ell)}\right]_{3,2}\right), \tag{5.28}$$

$$\hat{\phi}^{(\ell)} = \arctan\left(\left[\hat{\mathbf{R}}^{(\ell)}\right]_{1,2} / \left[\hat{\mathbf{R}}^{(\ell)}\right]_{2,2}\right). \tag{5.29}$$

This algorithmic step is facilitated by each velocity-sensor's direct measurement of one Cartesian direction cosine of the incident source. Such a simple mis-orientation calibration step would be *un*viable for, say, an array of isotropic microphones/hydrophones. [13]

5.8 Proposed Algorithm's Step #5: Calibration of the Vector-Sensors' Mis-Location

Recall that each velocity-sensor directly measures each Cartesian direction-cosine, as mentioned earlier in (5.12)-(5.15), which respectively give:

$$\begin{aligned}
\frac{\left[\hat{\mathbf{a}}_k^{(\ell)}\right]_1}{\left[\hat{\mathbf{a}}_k^{(1)}\right]_1} &\approx \frac{g_x^{(\ell)}}{g_x^{(1)}}\,\frac{u_k^{(\ell)}}{u_k^{(1)}}\,q_k^{(\ell)}\;e^{j\frac{2\pi f_k}{c}\left\{u_k\Delta_x^{(\ell)}+v_k\Delta_y^{(\ell)}+w_k\Delta_z^{(\ell)}\right\}},\\
\frac{\left[\hat{\mathbf{a}}_k^{(\ell)}\right]_2}{\left[\hat{\mathbf{a}}_k^{(1)}\right]_2} &\approx \frac{g_y^{(\ell)}}{g_y^{(1)}}\,\frac{v_k^{(\ell)}}{v_k^{(1)}}\,q_k^{(\ell)}\;e^{j\frac{2\pi f_k}{c}\left\{u_k\Delta_x^{(\ell)}+v_k\Delta_y^{(\ell)}+w_k\Delta_z^{(\ell)}\right\}},\\
\frac{\left[\hat{\mathbf{a}}_k^{(\ell)}\right]_3}{\left[\hat{\mathbf{a}}_k^{(1)}\right]_3} &\approx \frac{g_z^{(\ell)}}{g_z^{(1)}}\,\frac{w_k^{(\ell)}}{w_k^{(1)}}\,q_k^{(\ell)}\;e^{j\frac{2\pi f_k}{c}\left\{u_k\Delta_x^{(\ell)}+v_k\Delta_y^{(\ell)}+w_k\Delta_z^{(\ell)}\right\}},\\
\frac{\left[\hat{\mathbf{a}}_k^{(\ell)}\right]_4}{\left[\hat{\mathbf{a}}_k^{(1)}\right]_4} &\approx \frac{g_p^{(\ell)}}{g_p^{(1)}}\,q_k^{(\ell)}\;e^{j\frac{2\pi f_k}{c}\left\{u_k\Delta_x^{(\ell)}+v_k\Delta_y^{(\ell)}+w_k\Delta_z^{(\ell)}\right\}}.
\end{aligned}$$

Hence, the spatial phase-factor due to the ℓth vector-sensor's mis-location equals

$$\beta_k^{(\ell)} \overset{\text{def}}{=} \angle\left(e^{-j\frac{2\pi}{\lambda_k}\left\{\hat{u}_k x^{(\ell)}+\hat{v}_k y^{(\ell)}+\hat{w}_k z^{(\ell)}\right\}}\left[\hat{\mathbf{a}}_k^{(\ell)}\right]_4 / \left[\hat{\mathbf{a}}_k^{(1)}\right]_4\right)$$

if the ℓth vector-sensor contains a pressure-sensor.

However, if the ℓth vector-sensor has no pressure-sensor, then the three velocity-sensors' data need to be used as follows:

$$\beta_k^{(\ell)} \overset{\text{def}}{=} \frac{1}{3}\sum_{i=1}^{3}\angle\left(e^{-j\frac{2\pi}{\lambda_k}\left\{\hat{u}_k x^{(\ell)}+\hat{v}_k y^{(\ell)}+\hat{w}_k z^{(\ell)}\right\}}\left[\hat{\mathbf{a}}_k^{(\ell)}\right]_i / \left[\hat{\mathbf{a}}_k^{(1)}\right]_i\right).$$

[13] The step in (5.26) is analogous to [129]; however, the present method (unlike [129]) does *not* require any cooperative emitter of a prior known direction-of-arrival, but explicitly estimates the $3(L-1)$ mis-orientation angles of $\theta^{(\ell)}$, $\gamma^{(\ell)}$, $\phi^{(\ell)}, \forall \ell > 1$.

Accounting for all $K \geq 3$ sources,

$$\underbrace{\begin{bmatrix} \frac{2\pi}{\lambda_1}\hat{u}_1 & \frac{2\pi}{\lambda_1}\hat{v}_1 & \frac{2\pi}{\lambda_1}\hat{w}_1 \\ \vdots & \vdots & \vdots \\ \frac{2\pi}{\lambda_K}\hat{u}_K & \frac{2\pi}{\lambda_K}\hat{v}_K & \frac{2\pi}{\lambda_K}\hat{w}_K \end{bmatrix}}_{\stackrel{\text{def}}{=}\mathbf{\Pi}} \underbrace{\begin{bmatrix} \Delta_x^{(\ell)} \\ \Delta_y^{(\ell)} \\ \Delta_z^{(\ell)} \end{bmatrix}}_{\stackrel{\text{def}}{=}\boldsymbol{\varepsilon}} \approx \underbrace{\begin{bmatrix} \beta_1^{(\ell)} \\ \vdots \\ \beta_K^{(\ell)} \end{bmatrix}}_{\stackrel{\text{def}}{=}\boldsymbol{\nu}}.$$

The dislocation is assumed here as sufficiently small, such that no 2π cyclic ambiguity arises, i.e. the dislocation would be a fraction of a wavelength. Hence, $\{\Delta_x^{(\ell)}, \Delta_y^{(\ell)}, \Delta_z^{(\ell)}\}$ may be estimated as

$$\hat{\Delta}_x^{(\ell)} = [\boldsymbol{\varepsilon}]_1, \tag{5.30}$$

$$\hat{\Delta}_y^{(\ell)} = [\boldsymbol{\varepsilon}]_2, \tag{5.31}$$

$$\hat{\Delta}_z^{(\ell)} = [\boldsymbol{\varepsilon}]_3, \tag{5.32}$$

where

$$\boldsymbol{\varepsilon} \stackrel{\text{def}}{=} \left[\left(\mathbf{\Pi}^H\mathbf{\Pi}\right)^{-1}\mathbf{\Pi}^H\boldsymbol{\nu}\right]^T. \tag{5.33}$$

The above $\mathbf{\Pi}$ would be full ranked for any $K \geq 3$, except for parameters at a few discrete values, that would occur with probability 1 due to the noises in the data model. Specifically at $K = 3$, the simplification of $\left(\mathbf{\Pi}^H\mathbf{\Pi}\right)^{-1}\mathbf{\Pi}^H = \mathbf{\Pi}^{-1}$ holds.

This algorithmic step #5 is again facilitated by each velocity-sensor's direct measurement of one distinct Cartesian direction-cosine. However, this algorithmic step #5's simple form would be unavailable for an array of isotropic sensors.

5.9 Monte Carlo Simulations

5.9.1 The Proposed Scheme's Efficacy for "Blind" Calibration & Direction Finding

The proposed scheme (developed in Sections 5.5 to 5.8) is demonstrated here, via Monte Carlo simulations shown in Figure 5.1, for its efficacy to "blindly" calibrate the *intra*-vector-sensor gain uncertainty, the *inter*-vector-sensor mis-orientation, and the *inter*-vector-sensor dislocation. Plotted in Figure 5.1 are the performance metrics defined in Table 5.1. Therein, $\delta_{\theta,k,i}$ ($\delta_{\phi,k,i}$) symbolizes the ith Monte Carlo trial's estimation-error for θ_k (ϕ_k); and $\lambda_{\min}$ is defined as the minimum of $\lambda_1, \ldots, \lambda_K$. Furthermore, $\text{CRB}(g_p^{(1)}) = 0$ and $\delta_{g_p^{(1)},i} = 0, \forall i$, both by definition of the data model.

For the special case of pure-tone signals

The simulation scenario is detailed below: There exist $K = 3$ pure-tone incident signals, at digital frequencies $f_1' = 0.47$, $f_2' = 0.11$, and $f_3' = 0.28$, which are a priori unknown to the algorithm. Each pure tone has a random phase, uniformly distributed between $[0, 2\pi)$ radians, independently generated at each Monte Carlo trial, and independent across the

Table 5.1: Definitions of the performance metrics plotted in Figures 5.1-5.4

	Composite Mean-Square Error (Comp-RMSE)	Composite Cramér-Rao Bound (Comp-CRB)
DoA	$\sqrt{\frac{1}{2KI}\Sigma_{k=1}^{K}\Sigma_{i=1}^{I}\left(\delta^2_{\theta,k,i}+\delta^2_{\phi,k,i}\right)}$	$\sqrt{\frac{1}{2K}\Sigma_{k=1}^{K}\left(\mathrm{CRB}(\theta_k)+\mathrm{CRB}(\phi_k)\right)}$
gain uncertainty	$\sqrt{\frac{1}{4LI}\Sigma_{i=1}^{I}\Sigma_{\ell=1}^{L}\left(\delta^2_{g_x^{(\ell)},i}+\delta^2_{g_y^{(\ell)},i}+\delta^2_{g_z^{(\ell)},i}+\delta^2_{g_p^{(\ell)},i}\right)}$	$\sqrt{\frac{1}{4L}\Sigma_{\ell=1}^{L}\left[\mathrm{CRB}(g_x^{(\ell)})+\mathrm{CRB}(g_y^{(\ell)})+\mathrm{CRB}(g_z^{(\ell)})+\mathrm{CRB}(g_p^{(\ell)})\right]}$
mis-orientation	$\sqrt{\frac{1}{3(L-1)I}\Sigma_{i=1}^{I}\Sigma_{\ell=2}^{L}\left(\delta^2_{\tilde{\theta}^{(\ell)},i}+\delta^2_{\tilde{\gamma}^{(\ell)},i}+\delta^2_{\tilde{\phi}^{(\ell)},i}\right)}$	$\sqrt{\frac{1}{3(L-1)}\Sigma_{\ell=2}^{L}\left[\mathrm{CRB}(\tilde{\theta}^{(\ell)})+\mathrm{CRB}(\tilde{\gamma}^{(\ell)})+\mathrm{CRB}(\tilde{\phi}^{(\ell)})\right]}$
dislocation	$\sqrt{\frac{1}{3(L-1)I\lambda^2_{\min}}\Sigma_{i=1}^{I}\Sigma_{\ell=2}^{L}\left(\delta^2_{\Delta_x^{(\ell)},i}+\delta^2_{\Delta_y^{(\ell)},i}+\delta^2_{\Delta_z^{(\ell)},i}\right)}$	$\sqrt{\frac{1}{3(L-1)\lambda^2_{\min}}\Sigma_{\ell=2}^{L}\left[\mathrm{CRB}(\Delta_x^{(\ell)})+\mathrm{CRB}(\Delta_y^{(\ell)})+\mathrm{CRB}(\Delta_z^{(\ell)})\right]}$

Table 5.2: The five non-ideal acoustic-vector-sensors' actual Cartesian locations, actual mis-locations, actual misorientations, actual gain nonidealities for the simulations in Figures 5.1-5.4

ℓ	1	2	3	4	5
Construction	4-component	4-component	4-component	4-component	4-component
$\frac{(x_\ell,y_\ell,z_\ell)}{\lambda_{\min}}$	(0, 0, 0)	(−1.5, 1.8, 1.9)	(2.2, −1.9, 1.5)	(1.8, 2.0, 2.1)	(−2.1, −1.9, 2.3)
$\frac{[\Delta_x^{(\ell)},\Delta_y^{(\ell)},\Delta_z^{(\ell)}]}{\lambda_{\min}}$	(0, 0, 0)	(0.17, 0.18, 0.17)	(−0.19, 0.18, 0.17)	(0.17, −0.15, −0.13)	(−0.18, 0.19, −0.20)
$(\tilde{\theta}^{(\ell)},\tilde{\gamma}^{(\ell)},\tilde{\phi}^{(\ell)})$	(0.0°, 0.0°, 0.0°)	(6.2°, −6.5°, −6.0°)	(7.3°, −6.9°, 6.7°)	(6.1°, 6.0°, 6.3°)	(7.2°, −6.5°, 6.6°)
$(g_x^{(\ell)},g_y^{(\ell)},g_z^{(\ell)},g_p^{(\ell)})$	(0.80, 1.20, 1.19, 1.00)	(1.18, 0.81, 1.21, 1.19)	(1.21, 0.82, 1.20, 1.23)	(1.18, 1.21, 0.84, 1.17)	(1.16, 0.82, 1.18, 1.24)

signals. The emitters' respective azimuth-elevation directions-of-arrival are $(\theta_1,\phi_1) = (38^\circ, 25^\circ)$, $(\theta_2,\phi_2) = (82^\circ, -143^\circ)$, and $(\theta_3,\phi_3) = (121^\circ, -73^\circ)$, also a priori unknown to the receiver. There exist $L = 5$ non-ideal vector-sensors, with non-ideal gains, mis-orientations, and mis-locations as indicated in Table 5.2. At each Monte Carlo trial, the collected data consist of $N = 500$ snapshots, corrupted by additive Gaussian noise, white over time, white also across all velocity-sensors and all pressure-sensors. Each icon in Figure 5.1 consists of $I = 100$ statistically independent Monte Carlo trials.

The Monte Carlo simulations in Figure 5.1 verify that the proposed algorithm offers highly accurate "blind" calibration and direction finding.

If vector-sensor contains pressure-sensor, for SNR = 10dB, the R.M.S.E. for gain estimation is 0.0243 which is about 12% of the gain deviation, the R.M.S.E. for mis-orientation estimation is 0.9408° which is about 14.4% of the orientation deviation, the R.M.S.E. for dislocation estimation is $0.04982\lambda_{\min}$ which is about 28.5% of the location deviation, and the R.M.S.E. for DOA estimation is 1.002°.

If vector-sensor contains no pressure-sensor, for SNR = 10dB, the R.M.S.E. for gain estimation is 0.02657 which is about 13% of the gain deviation, the R.M.S.E. for mis-orientation estimation is 1.231° which is about 18.9% of the orientation deviation, the R.M.S.E. for dislocation estimation is $0.03394\lambda_{\min}$ which is about 19.4% of the location deviation, and the R.M.S.E. for DOA estimation is 0.9258°.

For the special case of narrowband random signals, each with a subband unoccupied by any other incident signal

There are again $K = 3$ signals with non-overlapping subbands, centered at $f_1' = 0.47$, $f_2' = 0.11$, and $f_3' = 0.28$, wherein the envelopes are statistically independent over time and across signals, complex-valued, and circularly complex Gaussian distributed, with a zero mean and unit variance. The other simulation scenario and setting are same as

Section 5.9.1.

For SNR = 10dB, the R.M.S.E. for gain estimation is 0.0245 which is about 12% of the gain deviation, the R.M.S.E. for mis-orientation estimation is 1.001° which is about 15% of the orientation deviation, the R.M.S.E. for dislocation estimation is $0.05325\lambda_{\min}$ which is about 30% of the location deviation, and the R.M.S.E. for DOA estimation is 1.118°.

For the special case of narrowband random signals, all occupying the same band during the same period

The simulation scenario is same as Section 5.9.1, except that $f_1' = f_2' = f_3' = 0.13$. Please also see endnote 11.

For SNR = 10dB, the R.M.S.E. for gain estimation is 0.03076 which is about 15% of the gain deviation, the R.M.S.E. for mis-orientation estimation is 1.147° which is about 18% of the orientation deviation, the R.M.S.E. for dislocation estimation is $0.04728\lambda_{\min}$ which is about 27% of the location deviation, and the R.M.S.E. for DOA estimation is 0.6727°.

5.9.2 The Proposed Scheme's Orders-of-Magnitude Computational Simplicity Over the Maximum Likelihood Estimation (MLE)

To highlight the computational efficiency of the proposed scheme, it will be compared here against maximum-likelihood estimation (MLE) of the non-ideality parameters and the directions-of-arrival.

The MLE minimizes the objective function,

$$F(\mu) \;=\; \left\| \tilde{\mathbf{z}} - \sum_{k=1}^{K} \mathbf{a}_k(\boldsymbol{\mu}) \otimes \mathbf{s}_k \right\|^2, \tag{5.34}$$

where the $4LN \times 1$ vector $\tilde{\mathbf{z}}$ is re-sized from the $4L \times N$ data-matrix $\mathbf{Z}$, and

$$\begin{aligned} \boldsymbol{\mu} \;=\; & [\theta_1, \ldots, \theta_K, \phi_1, \ldots, \phi_K, \\ & g_x^{(1)}, \ldots, g_x^{(L)}, g_y^{(1)}, \ldots, g_y^{(L)}, g_z^{(1)}, \ldots, g_z^{(L)}, g_p^{(2)}, \ldots, g_p^{(L)}, \\ & \Delta_x^{(2)}, \ldots, \Delta_x^{(L)}, \Delta_y^{(2)}, \ldots, \Delta_y^{(L)}, \Delta_z^{(2)}, \ldots, \Delta_z^{(L)}, \\ & \tilde{\theta}^{(2)}, \ldots, \tilde{\theta}^{(L)}, \tilde{\gamma}^{(2)}, \ldots, \tilde{\gamma}^{(L)}, \tilde{\phi}^{(2)}, \ldots, \tilde{\phi}^{(L)}\Big] \end{aligned} \tag{5.35}$$

contains all $2K+10L-7$ (=49 for $k = 3$ and $L = 5$) number of to-be-estimated parameters, which are exactly the same as the proposed method assumes (see Section 5.3).

The MLE thus equals

$$\hat{\boldsymbol{\mu}} \;=\; \arg\min_{\boldsymbol{\mu}} F(\boldsymbol{\mu}), \tag{5.36}$$

with $F(\boldsymbol{\mu})$ iteratively evaluated via MATLAB's built-in minimization function "fminunc", which uses the Broyden-Fletcher-Goldfarb-Shanno (BFGS) method, to be set at the stopping criteria of MaxFunEvals= 10^4 for the maximum number of function evaluations, and MaxIter= 10^4 for the maximum number of iterations. These iterations are initialized at the ideal acoustic vector-sensors' nominal values of $g_x^{(\ell)} = g_y^{(\ell)} = g_z^{(\ell)} = g_p^{(\ell)} = 1$,

$\tilde{\theta}^{(\ell)} = \tilde{\gamma}^{(\ell)} = \tilde{\phi}^{(\ell)} = \Delta_x^{(\ell)} = \Delta_y^{(\ell)} = \Delta_z^{(\ell)} = 0$, and the direction-of-arrival values as indicated on the figures.

The simulation scenario is detailed below: There exist $K = 3$ pure-tone incident signals, at digital frequencies $f_1' = 0.47$, $f_2' = 0.16$, and $f_3' = 0.38$, which are a priori unknown to the receiver. Each pure tone has a random phase, uniformly distributed between $[0, 2\pi)$ radians, independently generated at each Monte Carlo trial, and independent across the signals. The emitters' respective azimuth-elevation directions-of-arrival are $(\theta_1, \phi_1) = (80^\circ, 20^\circ)$, $(\theta_2, \phi_2) = (40^\circ, -155^\circ)$, and $(\theta_3, \phi_3) = (85^\circ, 105^\circ)$, also a priori unknown to the receiver. There exist $L = 5$ non-ideal acoustic vector-sensors, with non-ideal gains, mis-orientations, and mis-locations as indicated in Table 5.3. At each Monte Carlo trial, the collected data consist of $N = 80$ snapshots, corrupted by additive Gaussian noise, white over time, white also across all velocity-sensors and all pressure-sensors. Each icon in Figure 5.5 consists of $I = 100$ statistically independent Monte Carlo trials.

Table 5.3: The five non-ideal acoustic-vector-sensors' actual Cartesian locations, actual mis-locations, actual misorientations, actual gain nonidealities for the simulations in Figure 5.5

ℓ	1	2	3	4	5
Construction	4-component	4-component	4-component	4-component	4-component
$\frac{(x_\ell, y_\ell, z_\ell)}{\lambda_{\min}}$	(0, 0, 0)	(0.22, 0.22, 0)	(0.25, 0.25, 0)	(0.28, 0.28, 0)	(0.32, 0.32, 0)
$\frac{(\Delta_x^{(\ell)}, \Delta_y^{(\ell)}, \Delta_z^{(\ell)})}{\lambda_{\min}}$	(0, 0, 0)	(0.01, 0.02, 0.03)	(0.021, 0.018, 0.037)	(0.015, 0.018, 0.020)	(0.032, 0.026, 0.010)
$(\tilde{\theta}^{(\ell)}, \tilde{\gamma}^{(\ell)}, \tilde{\phi}^{(\ell)})$	$(0.0^\circ, 0.0^\circ, 0.0^\circ)$	$(8^\circ, 5^\circ, 9^\circ)$	$(3^\circ, 6^\circ, 2^\circ)$	$(4^\circ, 5^\circ, 8^\circ)$	$(6^\circ, 10^\circ, 7^\circ)$
$(g_x^{(\ell)}, g_y^{(\ell)}, g_z^{(\ell)}, g_p^{(\ell)})$	(1.12, 1.10, 1.03, 1)	(0.9, 1.06, 1.20, 1.17)	(1.06, 0.97, 1.11, 1.02)	(1.10, 1.06, 1.02, 1.15)	(0.9, 0.91, 1.14, 1.05)

Figure 5.5 plots the various composite MSE's versus the computational complexity, for the proposed scheme and for maximum likelihood estimation. This computational complexity is measured in terms of elapsed CPU time, as indicated by MATLAB's built-in functions "TIC" and "TOC". [14] In Figure 5.5, the TolFun value for MLE varies from $[10^{-1}, 10^{-1.5}, \ldots, 10^{-5.5}, 10^{-6}]$. The simulation scenario and setting are same as for Figure 5.1, except that SNR= 25dB here.

Figure 5.5 shows that the MLE would require a computational time *over three orders-of-magnitude* over that of the proposed method (i.e., the lone circle icon at the lower left corner of each subfigure), for comparable composite MSE's. Why is the proposed scheme so much simpler in computational load? This is because the proposed algorithm (unlike the MLE) needs no exhaustive/iterative search, but solves mostly linear equations. The MLE has a computational load that increases with the number N of snapshots, but the proposed method's computational load (after forming the data-correlation matrix) is *in*dependent of N.

Furthermore, the MLE is predicated on a perfect prior knowledge of the noise's full

[14] The proposed scheme's CPU-time consists of time in estimating the array's steering vectors by the "Uni-Vector-Hydrophone" ESPRIT in Section 5.4, for gain-uncertainty calibration in solving (5.19)-(5.22), for mis-orientation calibration in solving (5.27)-(5.29), and for mis-location calibration in solving (5.30)-(5.32). The MLE's CPU-time is the time to minimize the objective function in (5.36) via MATLAB's built-in function "FMINUNC".

space-time statistics - a demanding and perhaps unrealistic requirement, *not* imposed by the proposed scheme.

5.10 Summary

Herein advanced is the first algorithm in the open literature (to the best of the authors' knowledge) to "blindly" calibrate the intra-acoustic-vector-sensor gain-uncertainty, as well as the inter-acoustic-vector-sensor dislocation and mis-orientation, that may exist in a distributed array of acoustic vector-sensors. The proposed algorithm is computationally simpler than maximum-likelihood estimation by orders-of-magnitude.

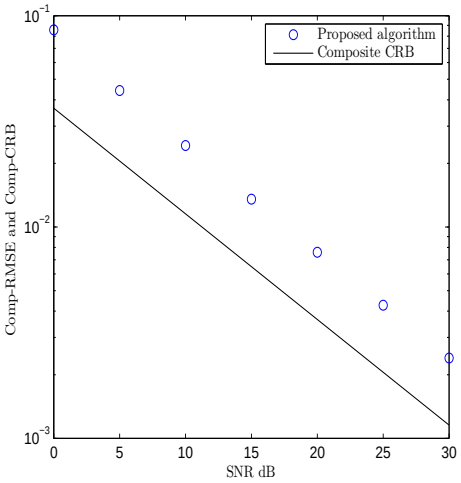

(a) Composite mean square error (Comp-RMSE) in estimating the gain-uncertainty coefficients.

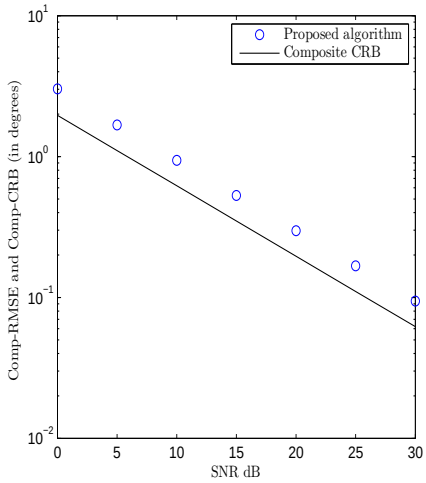

(b) Composite mean square error (Comp-RMSE) in estimating the mis-orientation angles.

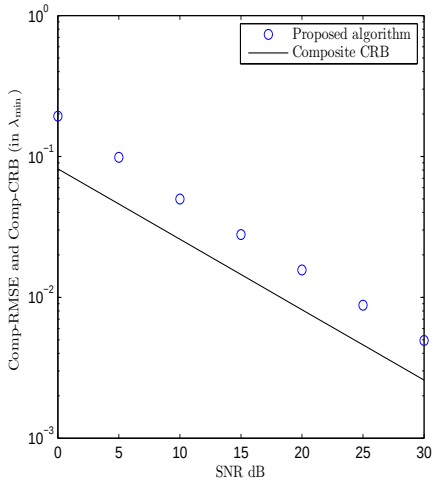

(c) Composite mean square error (Comp-RMSE) in estimating the dislocations.

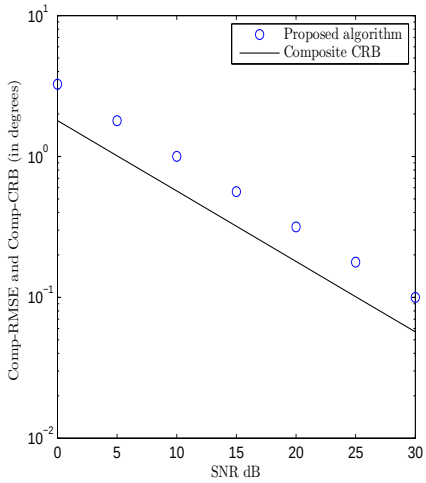

(d) Composite mean square error (Comp-RMSE) in estimating the azimuth-elevation directions-of-arrival.

Figure 5.1: Each acoustic vector-sensor contains pressure sensor: Monte Carlo simulations verify the efficacy of proposed scheme (in Sections 5.5 to 5.8) for "blind" calibration of intra-vector-sensor gain uncertainties, inter-vector-sensor mis-orientations, and inter-vector-sensor dislocations, as well as for direction finding, in the presence of pure-tone signals.

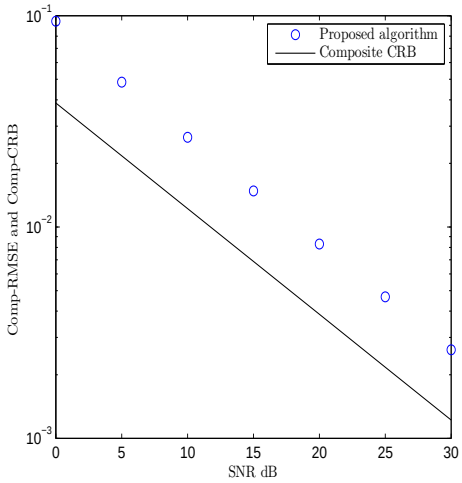

(a) Composite mean square error (Comp-RMSE) in estimating the gain-uncertainty coefficients.

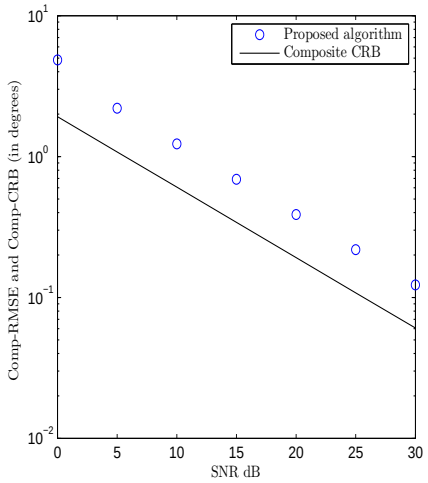

(b) Composite mean square error (Comp-RMSE) in estimating the mis-orientation angles.

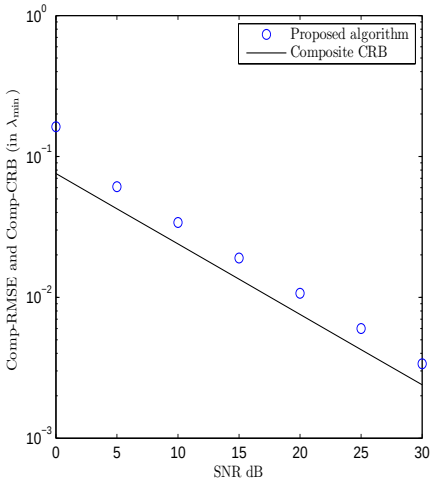

(c) Composite mean square error (Comp-RMSE) in estimating the dislocations.

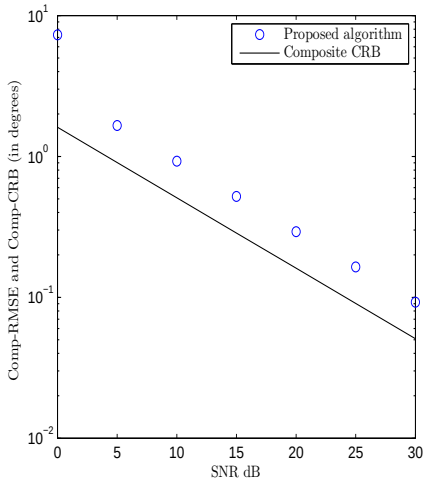

(d) Composite mean square error (Comp-RMSE) in estimating the azimuth-elevation directions-of-arrival.

Figure 5.2: Each acoustic vector-sensor contains no pressure sensor: Monte Carlo simulations verify the efficacy of proposed scheme (in Sections 5.5 to 5.8) for "blind" calibration of intra-vector-sensor gain uncertainties, inter-vector-sensor mis-orientations, and inter-vector-sensor dislocations, as well as for direction finding, in the presence of pure-tone signals.

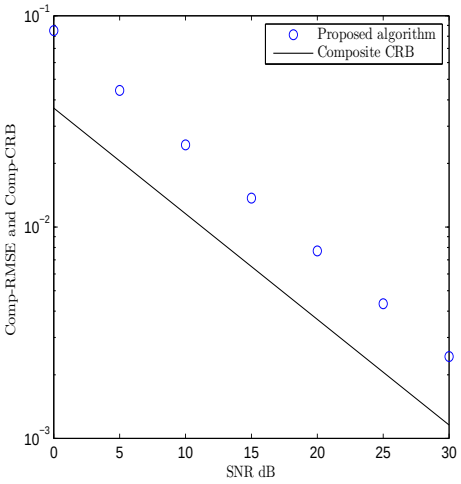

(a) Composite mean square error (Comp-RMSE) in estimating the gain-uncertainty coefficients.

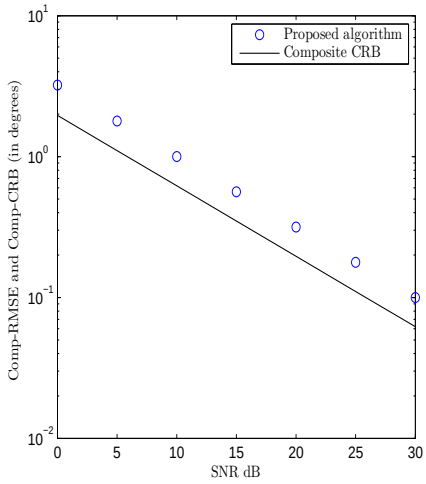

(b) Composite mean square error (Comp-RMSE) in estimating the mis-orientation angles.

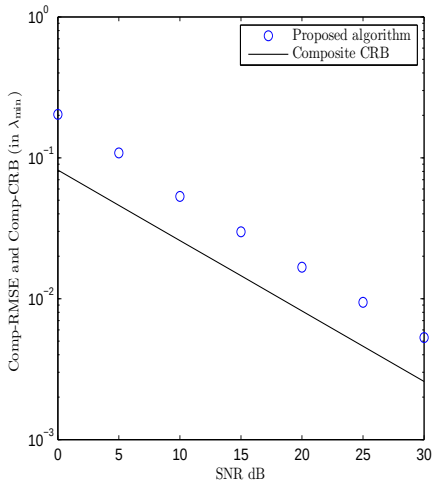

(c) Composite mean square error (Comp-RMSE) in estimating the dislocations.

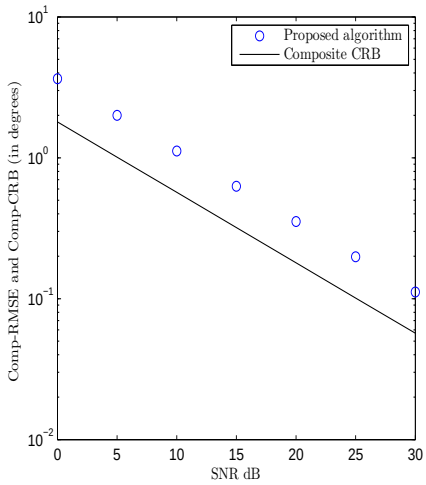

(d) Composite mean square error (Comp-RMSE) in estimating the azimuth-elevation directions-of-arrival.

Figure 5.3: Monte Carlo simulations verify the efficacy of proposed scheme (in Sections 5.5 to 5.8) for "blind" calibration of intra-vector-sensor gain uncertainties, inter-vector-sensor mis-orientations, and inter-vector-sensor dislocations, as well as for direction finding, in the presence of narrowband random signals, each with a subband unoccupied by any other incident signal.

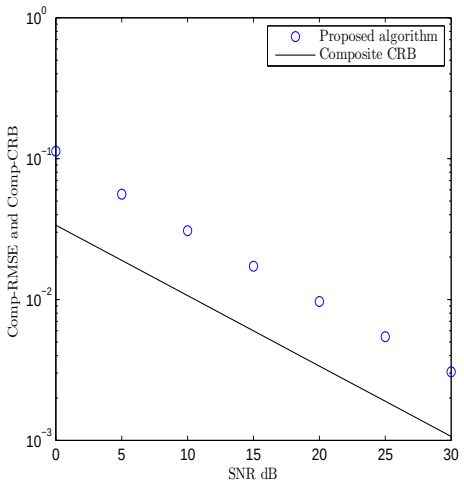

(a) Composite mean square error (Comp-RMSE) in estimating the gain-uncertainty coefficients.

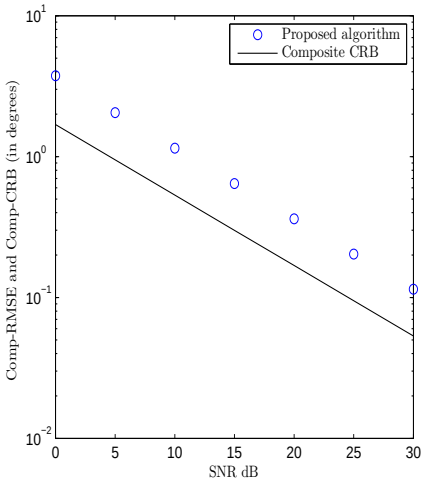

(b) Composite mean square error (Comp-RMSE) in estimating the mis-orientation angles.

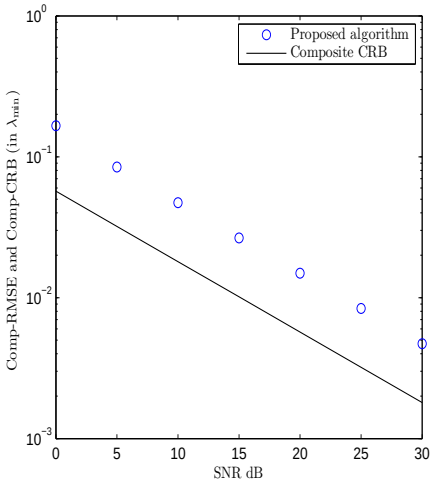

(c) Composite mean square error (Comp-RMSE) in estimating the dislocations.

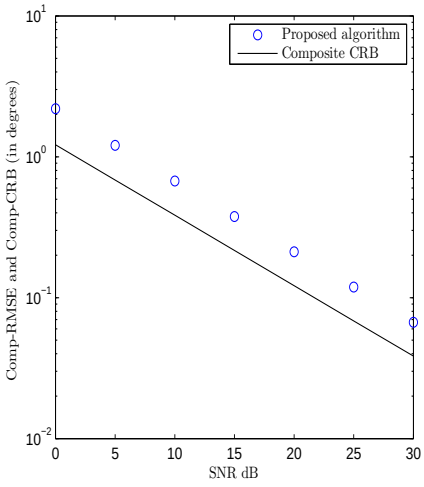

(d) Composite mean square error (Comp-RMSE) in estimating the azimuth-elevation directions-of-arrival.

Figure 5.4: Monte Carlo simulations verify the efficacy of proposed scheme (in Sections 5.5 to 5.8) for "blind" calibration of intra-vector-sensor gain uncertainties, inter-vector-sensor mis-orientations, and inter-vector-sensor dislocations, as well as for direction finding, in the presence of narrowband random signals, all occupying the same band during the same period.

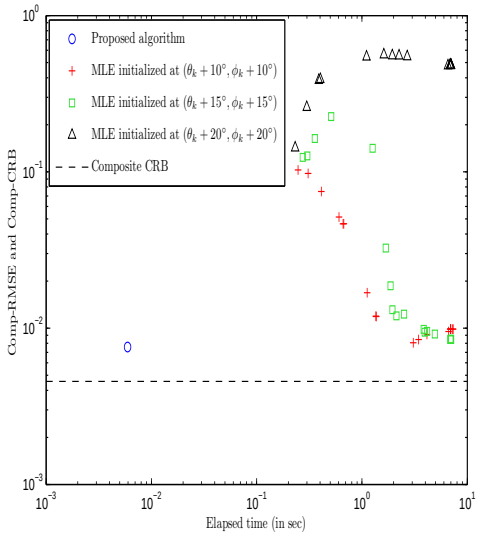

(a) Composite mean square error (Comp-RMSE) in estimating the gain-uncertainty coefficients.

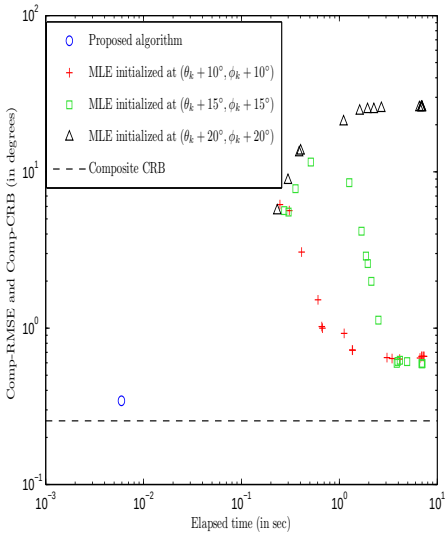

(b) Composite mean square error (Comp-RMSE) in estimating the mis-orientation angles.

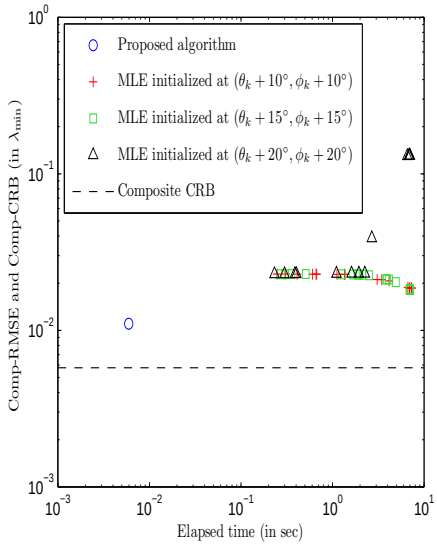

(c) Composite mean square error (Comp-RMSE) in estimating the dislocations.

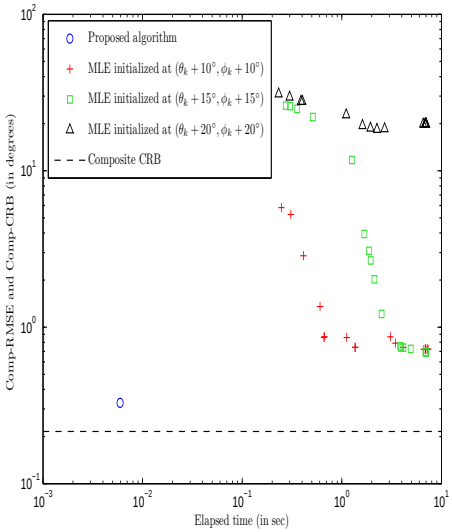

(d) Composite mean square error (Comp-RMSE) in estimating the azimuth-elevation directions-of-arrival.

Figure 5.5: The proposed scheme (i.e., the lone circle icon at the lower left corner of each subfigure) requires only about 0.1% of the MLE's computational load, for comparable composite RMSE's.

Chapter 6

A Lower Bound of Direction-of-Arrival Estimation for an Acoustic Vector Sensor Subject to Sensor Breakdown

[1]

6.1 Literature review

Direction-finding accuracy has been assessed for ideal acoustic vector sensors in terms of the Cramér-Rao bound in [26, 35, 45, 53, 58, 62, 70, 98, 103, 106, 133, 135, 149]. For non-ideal vector sensors with gain responses, unequal phase responses, spatial dislocation from the nominal array grids, misorientation – their direction-finding Cramér-Rao bounds have been derived in [122]. However, a real-world acoustic vector sensor could have some of its constituent sensor(s) inoperational altogether. For this, the present work analytically derives an approximate lower bound of the direction-of-arrival estimation error variance.

6.2 The Mathematical Model

6.2.1 An Ideal Acoustic Vector Sensor's Array Manifold

For an ideal four-element acoustic vector sensor located at the origin of the three-dimensional Cartesian coordinates, its far-field 4×1 array manifold equals [26, 135]:

$$\mathbf{a} \overset{\text{def}}{=} \begin{bmatrix} 1 \\ \sin\theta\cos\phi \\ \sin\theta\sin\phi \\ \cos\theta \end{bmatrix} \tag{6.1}$$

[1] This chapter is taken from [159], jointly authored by the candidate and his chief supervisor.

Table 6.1: Various failure cases for the acoustic vector sensor and their corresponding closed-form Cramér-Rao bounds

failure case #	x-axis velocity sensor functional ?	y-axis velocity sensor functional ?	z-axis velocity sensor functional ?	Array Manifold $\mathbf{Sa}=$	$\mathrm{CRB}^{(\mathbf{S})}(\theta) =$	$\mathrm{CRB}^{(\mathbf{S})}(\phi) =$
1	✓	×	×	$\begin{bmatrix} \sin(\theta)\cos(\phi) \end{bmatrix}$	∞	∞
2	×	✓	×	$\begin{bmatrix} \sin(\theta)\sin(\phi) \end{bmatrix}$	∞	∞
3	×	×	✓	$\begin{bmatrix} \cos(\theta) \end{bmatrix}$	∞	∞
4	✓	✓	×	$\begin{bmatrix} \sin(\theta)\cos(\phi) \\ \sin(\theta)\sin(\phi) \end{bmatrix}$	$\mathrm{CRB}_{x,y}(\theta) = \frac{\sigma^2}{2M}\frac{1}{\cos^2\theta}$	$\mathrm{CRB}_{x,y}(\phi) = \frac{\sigma^2}{2M}\frac{1}{\sin^2\theta}$
5	✓	×	✓	$\begin{bmatrix} \sin(\theta)\cos(\phi) \\ \cos(\theta) \end{bmatrix}$	$\mathrm{CRB}_{x,z}(\theta) = \frac{\sigma^2}{2M}\frac{1}{\sin^2\theta}$	$\mathrm{CRB}_{x,z}(\phi) = \frac{\sigma^2}{2M}\frac{\left(-\cot^2\theta+\csc^2\theta\csc^2\phi\right)}{\sin^2\theta}$
6	×	✓	✓	$\begin{bmatrix} \sin(\theta)\sin(\phi) \\ \cos(\theta) \end{bmatrix}$	$\mathrm{CRB}_{y,z}(\theta) = \frac{\sigma^2}{2M}\frac{1}{\sin^2\theta}$	$\mathrm{CRB}_{y,z}(\phi) = \frac{\sigma^2}{2M}\frac{\left(-\cot^2\theta+\csc^2\theta\sec^2\phi\right)}{\sin^2\theta}$
7	✓	✓	✓	$\begin{bmatrix} \sin(\theta)\cos(\phi) \\ \sin(\theta)\sin(\phi) \\ \cos(\theta) \end{bmatrix}$	$\mathrm{CRB}_{x,y,z}(\theta) = \frac{\sigma^2}{2M}$	$\mathrm{CRB}_{x,y,z}(\phi) = \frac{\sigma^2}{2M}\frac{1}{\sin^2\theta}$

where $\theta \in [0, \pi]$ symbolizes the elevation angle measured from the vertical z-axis, $\phi \in [0, 2\pi)$ denotes the azimuth angle measured from the positive x-axis. The first component in $\mathbf{a}$ corresponds to the pressure sensor. The second, third and fourth components correspond to the velocity sensors aligned along the x-axis, the y-axis, and the z-axis, respectively.

6.2.2 Sensor-Failure Model

Any particular velocity sensor must either function or fail, over the entire time-window when measurements are collected. Let p_ℓ denote probability that the ℓth velocity sensor breaks down. Alternatively, p_ℓ could be construed as the probability of the following composite event: the ℓth velocity sensor has either failed or been falsely identified as having failed. Any two velocity sensors would fail independently. The acoustic vector sensor's direction-finding capability needs not be affected by the presence or absence of the pressure sensor. This is because the pressure sensor in isotropic, thus provides no information on the incident wavefield's direction-of-arrival. Columns 2-4 of Table 6.1 list the only 7 possible operational states of the acoustic vector sensor.

The receiver is assumed to perfectly detect any failed velocity sensor, and would then disregard any output from any allegedly failed velocity sensor. If under two velocity sensors are identified as operational, the receiver system would need to shut down, as direction finding would be infeasible. Such a scenario would occur very rarely, as any well designed

velocity sensor would fail with only a small probability.

This chapter will derive an approximate lower bound for the direction-of-arrival estimation error variance, conditioned on the event that the whole receiver system remains operational. – in other words, conditional on at least two velocity sensors remain operational. This event occurs if and only if any of Table 6.1's failure cases #4 to #7 occur.

6.2.3 Review of the Wong-Wu-Hsu-Song Approximate Lower Bound [155]

The Wong-Wu-Hsu-Song approximate lower bound $\mathrm{ALB}_{\geq 2}$ was developed in [155], for the estimation of the one-dimensional direction-of-arrival ϕ, using a linear array of L number of uniformly spaced sensors that are identical and isotropic. In that context,

$$\begin{aligned}
\mathrm{ALB}_{\geq 2}(\phi) &= E\left[\left(\hat{\phi}-\phi\right)^2 \middle| Q \geq 2\right] \\
&= \Bigg\{ p^{L-2}(1-p)^2 \sum_{\{u_1,u_2\}\subseteq\,\Omega} \mathrm{CRB}_2^{\{u_1,u_2\}}(\phi) + p^{L-3}(1-p)^3 \sum_{\{u_1,u_2,u_3\}\subseteq\,\Omega} \mathrm{CRB}_3^{\{u_1,u_2,u_3\}}(\phi) \\
&\quad + \cdots + p(1-p)^{L-1} \sum_{\{u_1,u_2,\cdots,u_{L-1}\}\subseteq\Omega} \mathrm{CRB}_{L-1}^{\{u_1,u_2,\cdots,u_{L-1}\}}(\phi) \\
&\quad + (1-p)^L \mathrm{CRB}_L^{\{u_1,u_2,\cdots,u_L\}}(\phi) \Bigg\} \frac{1}{1-p^L-L(1-p)p^{L-1}},
\end{aligned} \tag{6.2}$$

where Ω refers to the set of L sensors, Q denotes the number of operational sensors out of all L sensors, $\mathrm{CRB}_q^{\{u_1,u_2,\cdots,u_q\}}(\phi)$ symbolizes the Cramér-Rao bound of the arrival-angle estimate $\hat{\phi}$, with the q operational sensors indexed by $u_1, u_2, \cdots, u_q$.

6.3 Derivation of the Approximate Lower Bound

6.3.1 The Data Model for Any Failure Case in Table 6.1

To focus on the phenomenon of random sensor breakdown, the following analysis will presume a simple model of the incident signal and a simple model of the noise. For more complex signal/noise scenarios, the present analytic approach can be modified straightforwardly.

Consider a spatially fixed point source in the far field, emitting a unit-power sinusoid signal $s(t) = \exp\left\{j\left(\frac{2\pi c}{\lambda}t + \varphi\right)\right\}$, at a known wavelength λ, a known propagation speed c, and a known initial phase φ. This signal impinges upon an acoustic vector sensor located at the spherical coordinates' origin. This signal is corrupted by a 3×1 vector of additive noise $\mathbf{n}(t)$, which is modeled as stochastic, Gaussian distributed, with a zero mean, with a diagonal spatial co-variance matrix $\mathbf{\Gamma}_0 = \mathrm{diag}[\sigma_v^2, \sigma_v^2, \sigma_v^2]$, under a zero temporal self-correlation. Modeled as deterministic but a priori unknown are the scalars θ, ϕ, and σ_v, grouped as elements of the vector $\boldsymbol{\rho}$.

At each time instant t, a fully operational acoustic vector sensor would collect a 3×1 data vector,

$$\mathbf{z}(t) = \mathbf{a}s(t) + \mathbf{n}(t). \tag{6.3}$$

Altogether, there exist N such time-samples, represented as a 3×3 data matrix, $\mathbf{Z} \stackrel{\text{def}}{=} [(\mathbf{z}(t_1))^T, \cdots, (\mathbf{z}(t_N))^T]^T$, where $t_i \neq t_j, \forall i \neq j$.

Direction-finding aims to estimate the azimuth arrival angle ϕ and the elevation arrival angle θ, based on the observations $\mathbf{Z}$. All other unknown parameters are nuisance parameters.

Suppose exactly one of the three velocity sensors is inoperational, as for failure cases #4-6 in Table 6.1. Then define a 2×3 selection-matrix $\mathbf{S}$ that equals a 3×3 identity-matrix $\mathbf{I}_3$ with one row omitted. If it is the x-axis (y-axis, z-axis) velocity sensor that has failed, omit the first (second, third) row. Hence, (6.3) becomes

$$\mathbf{Sz}(t) \quad = \quad \mathbf{Sa}s(t) + \mathbf{Sn}(t). \tag{6.4}$$

If all three velocity sensors are operational (as for failure case #7 in Table 6.1), then (6.4) would remain applicable with $\mathbf{S}$ degenerating to $\mathbf{I}_3$.

6.3.2 The Cramér-Rao Bound (CRB) for Each Specific Failure Case in Table 6.1

For the complex-value Gaussian $\mathbf{Z}$ and the unknown parameter vector $\boldsymbol{\rho}$ of Section 6.3.1, [24] (p. 525 and Appendix 15C) gives,

$$\begin{aligned}
\left[\mathrm{CRB}^{(\mathbf{S})}(\boldsymbol{\rho})\right]^{-1} \quad &= \quad \mathbf{J}^{(\mathbf{S})}_{\boldsymbol{\rho},\boldsymbol{\rho}} \quad = \quad \begin{bmatrix} J^{(\mathbf{S})}_{\theta,\theta} & J^{(\mathbf{S})}_{\theta,\phi} & J^{(\mathbf{S})}_{\theta,\sigma_v} \\ J^{(\mathbf{S})}_{\phi,\theta} & J^{(\mathbf{S})}_{\phi,\phi} & J^{(\mathbf{S})}_{\phi,\sigma_v} \\ J^{(\mathbf{S})}_{\sigma_v,\theta} & J^{(\mathbf{S})}_{\sigma_v,\phi} & J^{(\mathbf{S})}_{\sigma_v,\sigma_v} \end{bmatrix} \\
&= \quad 2\mathrm{Re}\left[\left(\frac{\partial\left(\mathbf{Sa}\otimes\mathbf{s}\right)}{\partial\boldsymbol{\rho}}\right)^H \left(\mathbf{S}\boldsymbol{\Gamma}_0 \otimes \mathbf{I}_N\right)^{-1} \left(\frac{\partial\left(\mathbf{Sa}\otimes\mathbf{s}\right)}{\partial\boldsymbol{\rho}}\right)\right] \\
&\quad +\mathrm{Tr}\left[\left(\mathbf{S}\boldsymbol{\Gamma}_0 \otimes \mathbf{I}_N\right)^{-1} \frac{\partial\left(\mathbf{S}\boldsymbol{\Gamma}_0 \otimes \mathbf{I}_N\right)}{\partial\boldsymbol{\rho}} \left(\mathbf{S}\boldsymbol{\Gamma}_0 \otimes \mathbf{I}_N\right)^{-1} \frac{\partial\left(\mathbf{S}\boldsymbol{\Gamma}_0 \otimes \mathbf{I}_N\right)}{\partial\boldsymbol{\rho}}\right],
\end{aligned} \tag{6.5}$$

where $\mathrm{Re}[\cdot]$ denotes the real-value part of the entity inside $[\cdot]$, $\mathrm{Tr}[\cdot]$ represents the trace operator, $\mathbf{s} \stackrel{\text{def}}{=} [s(t_1), \cdots, s(t_N)]$, and $\otimes$ symbolizes the Kronecker product.

As only the elevation arrival angle θ and the azimuth arrival angle ϕ are to-be-estimated, the Cramér-Rao bounds for $\{\theta, \phi\}$ would equal the diagonal entries in,

$$\begin{bmatrix} \mathrm{CRB}^{(\mathbf{S})}(\theta) & * \\ * & \mathrm{CRB}^{(\mathbf{S})}(\phi) \end{bmatrix} = \left[\begin{bmatrix} J^{(\mathbf{S})}_{\theta,\theta} & J^{(\mathbf{S})}_{\theta,\phi} \\ J^{(\mathbf{S})}_{\phi,\theta} & J^{(\mathbf{S})}_{\phi,\phi} \end{bmatrix} - \begin{bmatrix} J^{(\mathbf{S})}_{\theta,\sigma_v} \\ J^{(\mathbf{S})}_{\phi,\sigma_v} \end{bmatrix} \left(J^{(\mathbf{S})}_{\sigma_v,\sigma_v}\right)^{-1} \begin{bmatrix} J^{(\mathbf{S})}_{\theta,\sigma_v} & J^{(\mathbf{S})}_{\phi,\sigma_v} \end{bmatrix}\right]^{-1} \tag{6.6}$$

where $*$ denotes an entry not of interest to the present investigation. The above equation has used the well-known partitioned-matrix inversion formula.

Table 6.1 lists the expressions of $\mathrm{CRB}^{(\mathbf{S})}(\theta)$ and $\mathrm{CRB}^{(\mathbf{S})}(\phi)$, derived using (6.6), for each of the seven failure cases. Note Table 6.1's failure cases #1-3, where exactly one velocity sensor remains operational. There, $\mathrm{CRB}^{(\mathbf{S})}(\theta)$ and $\mathrm{CRB}^{(\mathbf{S})}(\phi)$ approach infinity, meaning one velocity sensor would be inadequate for direction-finding. Thus, a functional acoustic vector sensor system requires at least two operational velocity sensors.

6.3.3 Derivation of the Approximate Lower Bound for the Direction-of-Arrival Estimation Error Variance

The Wong-Wu-Hsu-Song approximate lower bound was developed in [155] for one-dimensional direction-of-arrival estimation, but the acoustic vector sensor here can determine the two-dimensional azimuth-elevation direction-of-arrival of the incident wavefield.

For the elevation angle estimation error variance, the Wong-Wu-Hsu-Song approximate lower bound [155] becomes

$$\begin{aligned} & \mathrm{ALB}_{\geq 2}(\theta) = E\left[\left(\hat{\theta}-\theta\right)^2 \middle| Q \geq 2\right] \\ = & \sum_{q=2}^{3}\left(E\left[\left(\hat{\theta}-\theta\right)^2 \middle| \text{ exactly } q \text{ velocity sensors operational}\right]\right. \\ & \left.\Pr\left\{\text{exactly } q \text{ velocity sensors operational } \middle| Q \geq 2\right\}\right), \end{aligned} \tag{6.7}$$

The outer summation starts from $Q = 2$, because the entire direction-finding system would be inoperational (with an undefined estimate and thus an undefined estimation error) if only one or zero velocity sensor works.

Typically the velocity sensors come in a lot from one manufacturer. Hence, all the velocity sensors are characterized by the same breakdown probability p. Hence, re-write (6.7) as

$$\begin{aligned} \mathrm{ALB}_{\geq 2}(\theta) &= \frac{\left\{p\,(1-p)^2\left[\mathrm{CRB}_{x,y}(\theta)+\mathrm{CRB}_{x,z}(\theta)+\mathrm{CRB}_{y,z}(\theta)\right]+(1-p)^3\,\mathrm{CRB}_{x,y,z}(\theta)\right\}}{\sum_{Q=2}^{3}\binom{3}{Q}p^{3-Q}\,(1-p)^Q} \\ &= \frac{\sigma^2}{2M}\frac{(1-p+2p\csc^2\theta+p\sec^2\theta)}{1+2p}. \end{aligned} \tag{6.8}$$

The above expression has drawn upon the $\mathrm{CRB}^{(\mathbf{S})}(\theta)$ expressions in Table 6.1. This $\mathrm{ALB}_{\geq 2}(\theta)$ is plotted in Figure 6.1.

Some qualitative observations on $\mathrm{ALB}_{\geq 2}(\theta)$:

{a} This $\mathrm{ALB}_{\geq 2}(\theta)$ is independent of ϕ, as expected, because the θ may be estimated by examining the power along the vertical axis alone or by examining the power on the entire horizontal plane as a whole – neither of which is affected by ϕ.

{b} As $p \to 0$, $\mathrm{ALB}_{\geq 2}(\theta) \to \frac{\sigma^2}{2M}$, which is independent of θ, in addition to being independent of ϕ.

{c} For $p > 0$, $\mathrm{ALB}_{\geq 2}(\theta)$ approaches infinity at $\theta = 0, \frac{\pi}{2}, \pi$, due to the $\sin\theta$ factor in the denominators of $\mathrm{CRB}_{x,z}(\theta)$ and $\mathrm{CRB}_{y,z}(\theta)$, and due to the $\cos\theta$ factor in the denominator of $\mathrm{CRB}_{x,y}(\theta)$. These $\mathrm{CRB}_{x,z}(\theta)$, $\mathrm{CRB}_{y,z}(\theta)$, $\mathrm{CRB}_{x,y}(\theta)$ would be increasingly significant to $\mathrm{ALB}_{\geq 2}(\theta)$ as p increases, hence the aforementioned peaks become more prominent as p increases.

Similarly for $\hat{\phi}$,

$$\mathrm{ALB}_{\geq 2}(\phi) = \frac{\sigma^2}{2M(1+2p)}\frac{1-2p\cot^2\theta+4p\csc^2(2\phi)\csc^2\theta}{\sin^2\theta}. \tag{6.9}$$

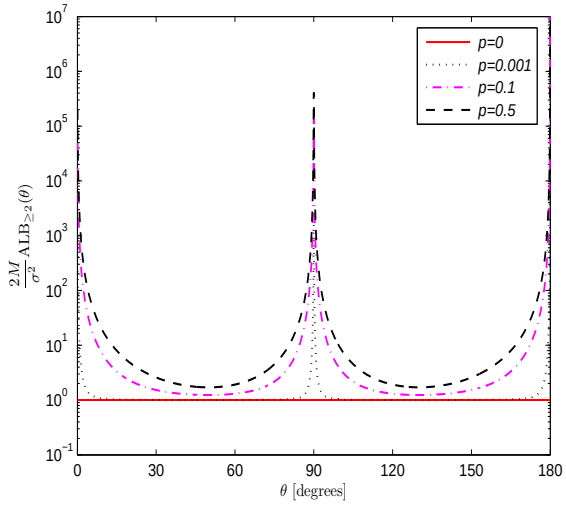

Figure 6.1: ALB$_{\geq 2}(\theta)$ derived in (6.8), which is independent of ϕ.

This ALB$_{\geq 2}(\phi)$ is plotted in Figures 6.3 and 6.2.

Some qualitative observations on ALB$_{\geq 2}(\phi)$:

{d} At all p, ALB$_{\geq 2}(\phi)$ goes to infinity at $\theta = 0, \pi$. This is because all of CRB$_{x,y}(\phi)$ and CRB$_{y,z}(\phi)$, CRB$_{x,z}(\phi)$ and CRB$_{x,y,z}(\phi)$ have infinite peaks at $\theta = 0, \pi$.

{e} At $p = 0$, ALB$_{\geq 2}(\phi)$ is independent of ϕ, because CRB$_{x,y,z}(\phi)$ is so. However, for $p > 0$, ALB$_{\geq 2}(\phi)$ would depend on CRB$_{x,y}(\phi)$ and CRB$_{y,z}(\phi)$, CRB$_{x,z}(\phi)$, all latter two of which depend on ϕ and approach infinity at $\phi = 0, \frac{\pi}{2}, \pi$. As p increases, these peaks become more prominent.

6.3.4 Verification by Monte Carlo Simulation of the Maximum Likelihood Estimator

The maximum likelihood estimator can asymptotically attain the Cramer-Rao bound, if the latter exists. Though the approximate lower bound is not necessarily a Cramer-Rao bound, the maximum likelihood estimation error variance will serve below as a benchmark of the approximate lower bound.

Figure 6.4 shows Monte Carlo simulations of the maximum likelihood estimator, verifying the tightness of the new metric of ALB$_{\geq 2}$, derived in (6.8) and (6.9). Here, $p = 0.2$, $\theta = 30^\circ$, $\phi = 40^\circ$, $\frac{\lambda}{c} = 450$Hz. Each data point is based on 2000 independent Monte Carlo experiments to simulate the arrays sensor-failure scenario and to simulate the maximum likelihood estimator. The maximum likelihood estimator uses 200 snapshots of data, with its iteration initialized at $\theta = 10^\circ$ and $\phi = 70^\circ$. The MATLAB built-in optimization function "FMINUNC" is used, with an allowable maximum of $10,000$ iterations or $10,000$ evaluations of the optimization cost function.

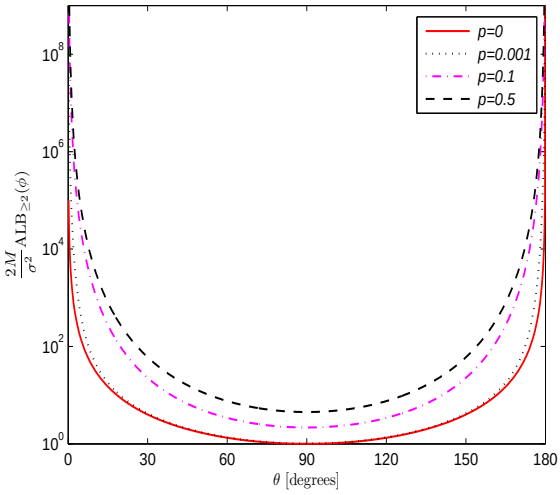

(a) $\phi = 15^o$

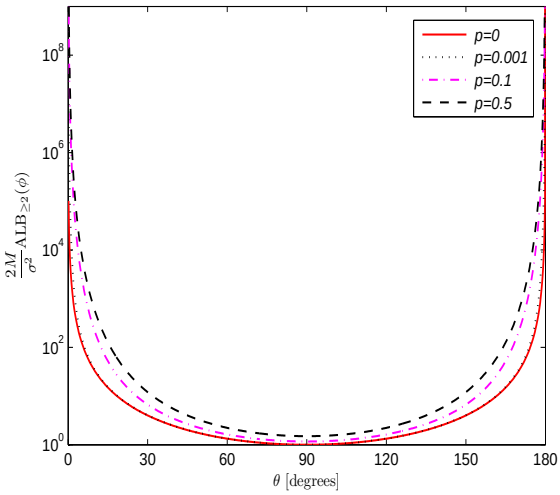

(b) $\phi = 135^o$

Figure 6.2: $\text{ALB}_{\geq 2}(\phi)$ derived in (6.8), when $\phi = 15°, 135°$.

6.4 Summary

This work derives approximate lower bounds for azimuth-elevation direction-of-arrival estimation using an acoustic vector sensor whose component sensors are individually subject to failure. Monte Carlo simulations of the maximum likelihood estimator verify the tightness of these bounds.

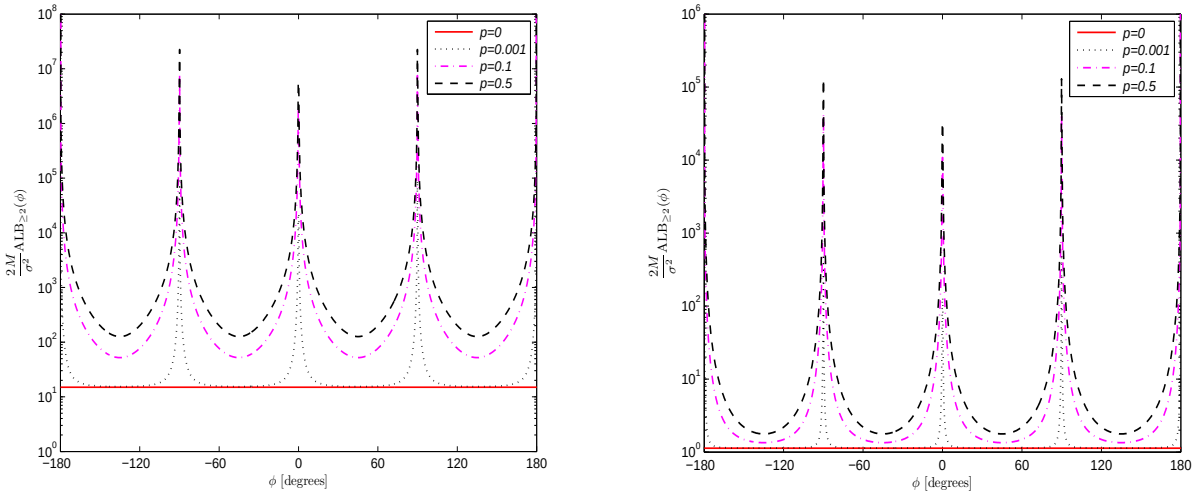

(a) $\theta = 15^o$ (b) $\theta = 70^o$

Figure 6.3: $\text{ALB}_{\geq 2}(\phi)$ derived in (6.8), when $\theta = 15°, 70°$.

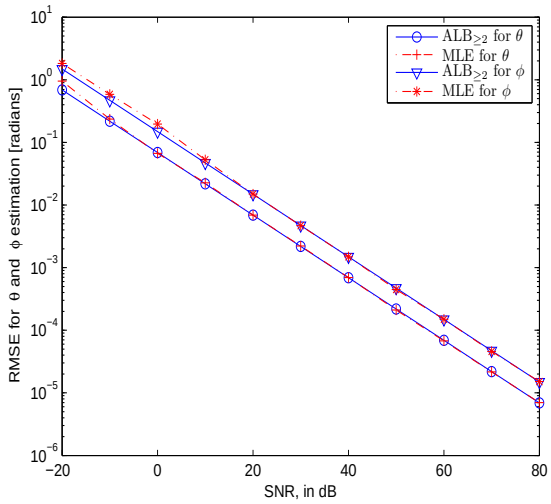

Figure 6.4: Maximum likelihood estimations verify the tightness of the the proposed metrics derived in (6.8) and (6.9).

Chapter 7

Three Dimensional Localization of a Near Field Emitter of Unknown Spectrum Using an Acoustic Vector Sensor

[1]

7.1 The Acoustic Vector Sensor's *Near*-field Array-Manifold

An acoustic vector sensor (a.k.a. vector hydrophone) is composed of three identical velocity sensors[2] in orthogonal orientations, and one pressure sensor (a.k.a. microphone or hydrophone) — all collocated spatially as a compact unit. A velocity sensor measures the particle velocity vector field's component along the velocity sensor's orientation. This particle velocity vector equals the spatial gradient of the customary pressure scalar field.[3] Both the particle velocity vector field and the pressure scalar field are thus measured directly by an acoustic vector sensor's four constituent sensors. Hence, the overall acoustic vector sensor measures both the vector plus the pressure scalar. This contrasts with a customary microphone or hydrophone, measuring only the acoustic pressure.

More precisely: Consider a point emitter incident with unit power upon an acoustic vector sensor, located at the Cartesian coordinates' origin. This acoustic vector sensor

[1] This chapter is taken from [160], jointly authored by the candidate and his chief supervisor.

[2] For a literature survey on the hardware implementations of velocity sensors, please refer to [7, 30].

[3] For a discussion of the acoustics physics underlying velocity sensor technology, please see [94].

would have this array manifold [135] [4] [5]

$$\mathbf{a} \;=\; \mathbf{a}(\theta,\phi,R) \;\stackrel{\text{def}}{=}\; \begin{bmatrix} u(\theta,\phi) \\ v(\theta,\phi) \\ w(\theta) \\ \frac{1}{\sqrt{1+\left(\frac{c}{2\pi f R}\right)^2}} e^{j \arctan \frac{c}{2\pi f R}} \end{bmatrix} \tag{7.1}$$

where $\theta \in [0,\pi]$ symbolizes the elevation angle of arrival measured from the positive z-axis, $\phi \in [0,2\pi)$ represents the azimuth angle of arrival measured from the positive x-axis, $u(\theta,\phi) = \sin(\theta)\cos(\phi)$ signifies the direction cosine along the x-axis, $v(\theta,\phi) = u(\theta,\phi)$ refers to the direction cosine along the y-axis, $w(\theta) = \cos(\theta)$ denotes the direction cosine along the z-axis, R symbolizes the distance between the acoustic vector sensor and the incident emitter, f denotes the incident signal's frequency. Specifically, the first, second, and third components in (7.1) correspond to the acoustic velocity sensors aligned along the x-axis, the y-axis, and the z-axis, respectively. The fourth component corresponds to the pressure sensor, which is isotropic. That fourth component would degenerate to unity for sufficiently large R, as for a source in the far field.

7.1.1 The Acoustic Vector Sensor for Source Localization

The acoustic vector sensor is versatile for source localization, on account of these properties:

(i) A single acoustic vector sensor possesses an intrinsic two dimensional directivity in the azimuth and the elevation, because the acoustic vector sensor simultaneously measures all three Cartesian components of the particle velocity field vector.

(ii) Among the three velocity sensors, their subarray manifold is independent of incident wavefield's frequency spectrum and of the radial separation of the emitter and the sensor. [135, 153, 154].

(iii) Multiple emitters' azimuth angles of arrival and the elevation angles of arrival may be estimated and then automatically matched, with only one acoustic vector sensor. [53].

For literature survey on direction finding algorithms exploiting the acoustic vector sensor's unique array manifold, please see [157]. In this literature, most works can handle only narrowband sources incident from only the far field. Wideband sources are handled in [61, 66, 76, 78, 87, 134, 147], but only if the sources lie in the far field. Near field sources are handled in [53, 132], but using an incorrect array manifold for the acoustic vector sensor – the correct array manifold has been derived only subsequently and recently in [135].

[4] The near field measurement models in [53, 132] for an acoustic vector sensor are incorrect.

[5] In [135], an extra multiplicative term $\rho_0 c$ exists in the fourth element of (7.1), where ρ_0 refers to the known density of the propagation medium, and c signifies the known propagation speed. Instead, (7.1) here has normalized the magnitude of each element to range between 0 and 1.

For both wideband and near field, this work is first to propose any source localization algorithm using an acoustic vector sensor. [6]

7.1.2 Whether to Exploit $\angle[\mathbf{a}]_4$ or $|[\mathbf{a}]_4|$ to Estimate R

Three dimensional localization of an emitter requires the estimation of the emitter's radial separation R from the sensors, in addition to the estimation of the azimuth elevation direction of arrival. Information of R is available from the vector $\mathbf{a}$, exclusively in its fourth entry. There, both the phase $\angle[\mathbf{a}]_4$ and the magnitude $|[\mathbf{a}]_4|$ offer information on R. Which should be used, or should both be used?

The following will show that $\angle[\mathbf{a}]_4$ is more sensitive to R, than $|[\mathbf{a}]_4|$ is. From (7.1),

$$\begin{aligned}\left|\frac{\partial\angle[\mathbf{a}]_4}{\partial R}\right| &= \frac{c}{f}\frac{2\pi}{\left(\frac{c}{f}\right)^2+4\pi^2R^2}\\ \left|\frac{\partial|[\mathbf{a}]_4|}{\partial R}\right| &= \left(\frac{c}{f}\right)^2\frac{2\pi}{\left[\left(\frac{c}{f}\right)^2+4\pi^2R^2\right]^{3/2}}\end{aligned}$$

Hence,

$$\frac{\left|\frac{\partial\angle[\mathbf{a}]_4}{\partial R}\right|}{\left|\frac{\partial|[\mathbf{a}]_4|}{\partial R}\right|} = \sqrt{1+\left(R\frac{2\pi f}{c}\right)^2} > 1,\ \forall R \tag{7.2}$$

That is, the phase of $[\mathbf{Z}(k^\circ)]$ embeds information on R in a way more sensitive to R than the magnitude is. Hence, the former should be used.

7.2 The Proposed Algorithm - Signal of Unknown Spectrum, in Temporally White Noise

Subsequent steps will demonstrate how to geolocate the near field emitter in three dimensions. The key insights are

(a) The array manifold's first three entries, which are frequency independent.

(b) The azimuth elevation direction of arrival information is contained exclusively in the array manifold's first three entries, whose Frobenius norm must equal one, regardless of the direction of arrival and regardless of the radial distance. That is, $[u(\theta,\phi)]^2+[v(\theta,\phi)]^2+[w(\theta)]^2=1),\ \forall\theta,\phi$.

(c) The radial distance information is contained exclusively in the array manifold's fourth entry, the magnitude and the phase of which each has a one-to-one correspondence to the radial distance R.

[6] Please refer to [122, 154] for extended literature surveys on acoustic vector sensor beam pattern analysis, hardware implementations, sea trials, atmospheric trials, in-room trials, and practical applications.

7.2.1 Data Statistical Model

For the near field acoustic vector sensor described in (7.1), it gathers the following 4×1 vector measurement at time $t = mT$:

$$\begin{aligned}\mathbf{z}(m) &= \frac{\sqrt{\mathcal{P}}}{M}\left\{\sum_{k=1}^{M}\mathbf{a}\left(\theta,\phi,R,\frac{k-1}{M}F_s\right)\ S(k)\ e^{j2\pi\frac{m(k-1)}{M}}\right\} \\ &\quad +\mathbf{n}(m)\end{aligned}$$

where $S(k)$ denotes the kth component of the discrete Fourier Transform (DFT) of the incident discrete time sequence $\{\mathbf{s}(m),\ m = 0, \cdots, M-1\}$ (which may be a priori unknown), M refers to the total number of snapshots, F_s symbolizes the sampling frequency, and $\mathbf{n}(m)$ represents a zero mean spatiotemporally uncorrelated random noise sequence of a priori unknown power $\mathcal{P}_n$.

The present problem is to estimate θ, ϕ, R, based on the M number of snapshots in $\mathbf{M_z} = [\mathbf{z}(1), \mathbf{z}(2), \cdots, \mathbf{z}(M)]$.

7.2.2 Estimation of Azimuth Elevation Arrival Angles from time-domain $\mathbf{M_z}$

This subsection exploits the aforementioned insight (a) that the array manifold's first three entries ,which contain the azimuth elevation direction of arrival information, are frequency independent.

The data correlation matrix of the received signal from the first three components can be computed as $\mathbf{R}_{\text{sub}} = \mathbf{M}_{\mathbf{z}}^{\text{sub}}\mathbf{M}_{\mathbf{z}}^{\text{sub}\,H}$, where $\mathbf{M}_{\mathbf{z}}^{\text{sub}} = \begin{bmatrix}\mathbf{I}_3 & \mathbf{0}_{3\times 1}\end{bmatrix}\mathbf{M_z}$ indicating the first three rows of $\mathbf{M_z}$, and $\mathbf{I}_3$ symbolizes the 3×3 identity matrix and ^{H} denotes the Hermitian operator.

Let $\mathbf{e}$ denote the eigenvector associated with the largest eigenvalue of $\mathbf{R}_{\text{sub}}$, then the Cartesian direction cosines may be estimated as

$$\hat{u} = \text{sign}(u)\frac{|[\mathbf{e}]_1|}{\|\mathbf{e}\|_2} \tag{7.3}$$

$$\hat{v} = \text{sign}(v)\frac{|[\mathbf{e}]_2|}{\|\mathbf{e}\|_2} \tag{7.4}$$

$$\hat{w} = \text{sign}(w)\frac{|[\mathbf{e}]_3|}{\|\mathbf{e}\|_2}, \tag{7.5}$$

The above sign$(\cdot)$ term estimates the sign of each of the first three entries of $\mathbf{a}$. Then, $\{\theta, \phi\}$ may be unambiguously estimated as

$$\hat{\theta} = \arccos\{\hat{w}\} \tag{7.6}$$

$$\hat{\phi} = \begin{cases} -\arccos\left\{\frac{\hat{u}}{\sin(\hat{\theta})}\right\}, & \frac{\hat{v}}{\sin(\hat{\theta})} \le 0 \\ \arccos\left\{\frac{\hat{u}}{\sin(\hat{\theta})}\right\}, & \frac{\hat{v}}{\sin(\hat{\theta})} \ge 0 \end{cases} \tag{7.7}$$

Notice that sign(u), sign(v) and sign(w) can be determined based on the information from one DFT bin that will be elucidated in the following subsections.

7.2.3 To Estimate the Steering Vector At a Chosen DFT bin

From $\mathbf{M_z}$, compute its discrete Fourier transform (DFT) $\mathbf{M_Z} = [\mathbf{Z}(1), \mathbf{Z}(2), \cdots, \mathbf{Z}(M)]$. From the first $\frac{M+2}{2}$ columns of $\mathbf{M_Z}$, identify the column (i.e. the discrete frequency) giving the maximum spectral magnitude. This DFT bin must also gives the highest signal-to-noise power ratio, as the additive noise has been presumed as white. That is identify the value of k°, such that $f_{k^\circ} = \frac{(k^\circ - 1)}{M} F_s$ corresponding to That is,

$$k^\circ \;=\; \arg \max_{1 \le k \le \frac{M}{2}+1} \sum \|\mathbf{Z}(k)\|\,, \tag{7.8}$$

where $\|\cdot\|$ denotes the Frobenius norm of the vector inside. Only the first $\frac{M+2}{2}$ DFT bins need be searched, because of their magnitude symmetry with the remaining DFT bins.[7]

The above identified $\mathbf{Z}(k^\circ)$ represents an ambiguous estimate of the steering vector. That is,

$$\mathbf{Z}(k^\circ) \;\approx\; \kappa \mathbf{a}\left(\theta, \phi, R, \frac{(k^\circ - 1)}{M} F_s\right), \tag{7.9}$$

where κ denotes an unknown complex value non zero scalar.

7.2.4 To Estimate R from $|[\mathbf{Z}(k^\circ)]_4|$

The radial distance R has a one-to-one correspondence with $|[\mathbf{a}]_4|$, where $[\cdot]_i$ symbolizes the ith entry of the vector inside the square brackets. Note that the above refers to only the magnitude of $[\mathbf{a}]_4$, not its phase. This $|[\mathbf{a}]_4|$ is not directly available, but earlier steps have estimated $\mathbf{a}$ to within an unknown scalar κ, which is complex value. Unambiguous estimation of $|[\mathbf{a}]_4|$ would require the estimation of only $|\kappa|$, but not the phase $\angle\kappa$ of κ.

To estimate $|\kappa|$, draw upon insight (b) stated at the beginning of this section, that the steering vector's first three entries must have a unity Frobenius norm regardless of the emitter's three dimensional location. That is,

$$\widehat{|\kappa|} \;=\; \sum_{i=1}^{3} |[\mathbf{Z}(k^\circ)]_i|^2 \tag{7.10}$$

Now, to estimate R, draw upon insight (b) stated at the beginning of this section, that a one-to-one mapping exists between $|\mathbf{a}|$ and R. That is,

$$\hat{R}_{\text{mag}} \;=\; \frac{\frac{cM}{(k^\circ - 1)F_s}}{2\pi\sqrt{\left(\frac{\widehat{|\kappa|}}{|[\mathbf{Z}(k^\circ)]_4|}\right)^2 - 1}}. \tag{7.11}$$

In the above, both $\widehat{|\kappa|}$ and $\hat{R}_{\text{mag}}$ have exploited only the magnitudes of the entries of $\mathbf{Z}(k^\circ)$, not their phases.

[7] The array manifold in (7.1) suggests that R may be more accurately estimated for a larger λ. Hence, (7.8) could search over only $1 \le k \le f_L \ll \frac{M}{2} + 1$, for some suitably chosen f_L.

As an estimate of R, available here is $\hat{R}_{\text{mag}}$. The latter may be computed and then be compared against $[\mathbf{Z}(k^\circ)]_4$, to give

$$\begin{aligned}\hat{\kappa} &= [\mathbf{Z}(k^\circ)]_4 \ / \ [\mathbf{a}]_4 \\ &= [\mathbf{Z}(k^\circ)]_4 \ e^{-j \arctan \frac{c}{2\pi \hat{R}_{\text{mag}}} \frac{M}{F_s(k^\circ-1)}} \sqrt{1+\left(\frac{c}{2\pi \hat{R}_{\text{mag}}} \frac{M}{F_s(k^\circ-1)}\right)^2}.\end{aligned}$$

This same complex value $\hat{\kappa}$ would also interrelated the complex value $[\mathbf{Z}(k^\circ)]_i$ exactly back to the real value $[\mathbf{a}]_i$, through $[\mathbf{a}]_i = [\mathbf{Z}(k^\circ)]_i / \hat{\kappa}$ for $i = 1, 2, 3$, but only under noiseless conditions. However, under noisy conditions, the above interrelations would become approximate, necessitating the removal of any imaginary value part in $[\mathbf{Z}(k^\circ)]_i / \hat{\kappa}$ to ensure a real value $[\mathbf{a}]_i$ for $i = 1, 2, 3$.

Thus, sign(u), sign(v) and sign(w) in (7.3)-(7.5) can be determined as

$$\text{sign}(u) = \text{sign}\left(\frac{[\mathbf{Z}(k^\circ)]_1}{\hat{\kappa}}\right) \tag{7.12}$$

$$\text{sign}(v) = \text{sign}\left(\frac{[\mathbf{Z}(k^\circ)]_2}{\hat{\kappa}}\right) \tag{7.13}$$

$$\text{sign}(w) = \text{sign}\left(\frac{[\mathbf{Z}(k^\circ)]_3}{\hat{\kappa}}\right), \tag{7.14}$$

where $\Re(\cdot)$ refers to the real value part of the entity inside the parentheses and $\|\cdot\|_2$ denotes the 2 norm operator.

7.2.5 To Estimate R from $\angle[\mathbf{Z}(k^\circ)]_4$

This subsection exploits the aforementioned insight (b) that a one-to-one mapping exists also between R and $\angle[\mathbf{a}]_4$.

As a one-to-one mapping exists between R and $\angle[\mathbf{a}]_4$; thus, an approximate one-to-one mapping also exists between $\hat{R}_{\text{phs}}$ and $\angle[\mathbf{Z}(k^\circ)]_4$. Therefore, consider the complex phase of the fourth entry of the vector equation in (7.9),

$$\angle[\mathbf{Z}(k^\circ)]_4 - \widehat{\angle\kappa} = \arctan \frac{c}{2\pi f \hat{R}_{\text{phs}}}. \tag{7.15}$$

Setting $f = \left(\frac{k^\circ-1}{M}\right) F_s$, (7.15) gives:

$$\hat{R}_{\text{phs}} = \frac{c}{2\pi} \frac{M}{(k^\circ-1)F_s} \cot\left(\angle[\mathbf{Z}(k^\circ)]_4 - \widehat{\angle\kappa}\right), \tag{7.16}$$

where

$$\widehat{\angle\kappa} = \angle\left(\frac{[\mathbf{Z}(k^\circ)]_1 / \hat{u} + [\mathbf{Z}(k^\circ)]_2 / \hat{v} + [\mathbf{Z}(k^\circ)]_3 / \hat{w}}{3}\right) \tag{7.17}$$

In the above, both $\widehat{\angle\kappa}$ and $\hat{R}_{\text{phs}}$ have exploited only the phases of the entries of $\mathbf{Z}(k^\circ)$, not their magnitudes.

7.2.6 Estimation of R Base on All the Frequency Bins

In this subsection, the results from all the DFT bins are combined by some sort of subspace method as in [10]. The basic procedures are as follows:

At each DFT bin

Let $\mathbf{E}_n^{(k)}$ denote the 4×3 noise subspace eigenvector matrix for data correlation matrix $\mathbf{R}^{(k)} \stackrel{\text{def}}{=} \mathbf{Z}(k)\mathbf{Z}(k)^H$. The distance from orthogonality between array manifold and noise subspace may be measured as $\left\| \mathbf{a}\left(\theta, \phi, R, \frac{(k-1)}{M} F_s\right)^H \mathbf{E}_n^{(k)} \right\|_2$. Smaller this value is, closer to orthogonal steering vector and noise subspace will likely be.

For all the DFT bins

The distance from orthogonality between steering vector and noise subspace at different DFT bins can be combined using arithmetic mean metric so as to find range R that yields the minimum of the following estimator.

$$\hat{R} \;=\; \arg\min_{R} \sum_{k=2}^{\frac{M+2}{2}} \left\| \mathbf{a}\left(\hat{\theta}, \hat{\phi}, R, \frac{(k-1)}{M} F_s\right)^H \mathbf{E}_n^{(k)} \right\|_2 \tag{7.18}$$

Notice that this optimization problem can be effectively solved by initializing with $R = \hat{R}_{\text{phs}}$.

7.3 The Proposed Algorithm - Signal of Unknown Spectrum, in Temporally Colored Noise

If the additive noise is temporally colored, the DFT bin satisfying (7.8) would not necessarily give the highest signal-to-noise power ratio. Instead, some sort of "signal subspace fitting" like procedure in Section 7.2.6 could be used to identify the DFT bin most advantageous for use in Sections 7.2.4 to 7.2.5. The basic idea is as follows: At any one frequency f_k, the weaker the noise is, the closer to orthogonal steering vector and noise subspace will likely be.

The following is one such rudimentary procedure: The steering vector which is the "most orthogonal" to noise subspace eigenvector matrix $\mathbf{E}_n^{(k)}$ occurs at the $\tilde{k}$th DFT bin, with $\tilde{k}$ equal to

$$\arg\min_{2 \le k \le \frac{M+2}{2}} \left\| \mathbf{a}\left(\theta_k, \phi_k, R_k, \frac{(k-1)}{M} F_s\right)^H \mathbf{E}_n^{(k)} \right\|_2$$

where θ_k, ϕ_k are estimated respectively from (7.6) and (7.7) in which the signs of direction cosines are determined via (7.12)-(7.14) but replacing k° therein by k, and R_k is estimated from $\mathbf{Z}(k)$, via (7.16) but replacing k° therein by k.

After thus identifying $\tilde{k}$, the emitter's azimuth elevation arrival angles may be estimated as $\hat{\theta} = \theta_{\tilde{k}}$ and $\hat{\phi} = \phi_{\tilde{k}}$, the emitter's range R may be estimated from (7.18) by initializing with $\hat{\theta} = \theta_{\tilde{k}}$, $\hat{\phi} = \phi_{\tilde{k}}$, $\hat{R} = R_{\tilde{k}}$.

7.4 Verification by Monte Carlo Simulations

The following Monte Carlo simulations verify the efficacy of the new source localization algorithms proposed in Sections 7.2 and 7.3.

Here, the emitter lies at $\theta = 60^o$, $\phi = 40^o$, $R = 25$m. For underwater acoustic applications: $f_s = 400$Hz, $c = 1524$m/s, $M = 800$. The temporally colored Gaussian noise is generated as follows for Figure 7.2: Pass a temporally white zero mean Gaussian noise sequence through an equiripple filter bandpass filter, which is realized by the MATLAB built-in function fdesign.bandpass(Fst1=$\frac{30}{f_s/2}$, Fp1=$\frac{40}{f_s/2}$, Fp2=$\frac{180}{f_s/2}$, Fst2=$\frac{195}{f_s/2}$, Ast1=60, Ap=1, Ast2=60).

Each icon in Figures 7.1 and 7.2 consists of $I = 2000$ statistically independent Monte Carlo trials.[8] These figures plot the "root mean square errors" of the Cartesian direction cosines, $\text{RMSE}(\hat{\theta}, \hat{\phi}) = \frac{1}{\sqrt{2}I} \sum_{i=1}^{I} \sqrt{\delta_{\theta,i}^2 + \delta_{\phi,i}^2}$, where $\delta_{\theta,i}$ ($\delta_{\phi,i}$) symbolizes the ith Monte Carlo trial's estimation error in $\hat{\theta}$ ($\hat{\phi}$). Also plotted is $\text{RMSE}(R) = \frac{1}{I} \sum_{i=1}^{I} \sqrt{\delta_{R,i}^2}$, where $\delta_{R,i}$ symbolizes the ith trial's estimation error in $\hat{R}$. Because the noise spectrum may be arbitrary and unknown, the Cramér-Rao bound is not derived.

These figures show that the direction of arrival can be estimated within 0.8° for 5dB SNR in white noise, and to within 1.5° for 5dB SNR in colored noise. The distance is less accurately estimated: a 4% error can be obtained only for white noise SNR exceeding 15dB and for colored noise SNR over 10dB. Note that the colored noise case allows better estimation accuracy, because the noise power is unevenly distributed over the DFT bins, with some DFT bin enjoying above average SNR and thus offering better estimation accuracy.

7.5 Summary

Herein proposed are algorithms to localize a near field source, emitting a signal of unknown spectrum, based on data collected by one acoustic vector sensor, corrupted additively by white noise or by unknown colored noise. Monte Carlo algorithms verify the efficacy of these algorithms.

[8] For Figure 7.1, the optimization in (7.8) is over $20 \geq k \geq 40$. The lower limit arises because underwater acoustic signals seldom falls below 10Hz. The upper limit corresponds to a $f_L = 20$Hz. These are not used for Figure 7.2, where the noise spectrum is a priori unknown.

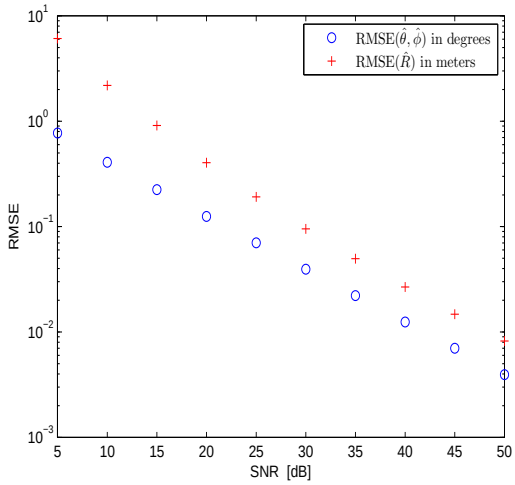

Figure 7.1: Monte Carlo simulations verify the efficacy of the source localization algorithm proposed in Section 7.3 for an incident signal of unknown spectrum corrupted additively by temporally white zero mean Gaussian noise.

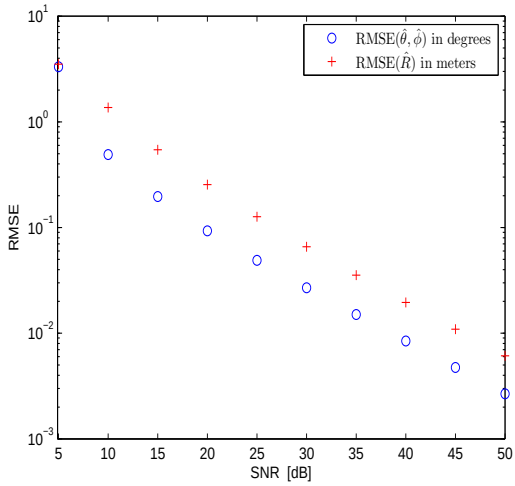

Figure 7.2: Monte Carlo simulations verify the efficacy of the source localization algorithm proposed in Section 7.3 for an incident signal of unknown spectrum corrupted additively by zero mean Gaussian noise of unknown temporal correlation.

Chapter 8

"Blind" Reception to Null Unknown Interference for Block-Based Single-Carrier Transmission with an Insufficient Guard Interval

[1]

8.1 Literature Review

Single-carrier (SC) block-based (BB) cyclic-prefixed (CP) transmission combines two advantages: (i) The use of a single carrier (unlike the use of multiple carriers) avoids high peak-to-average power ratios (PAPR) in the modulator output. (ii) Block-based transmission's cyclic prefix converts the linear convolution between the transmitted signal and the channel impulse response (CIR) into a circular convolution, thereby allowing the receiver to enjoy the simplicity of single-tap equalization at each discrete-Fourier-transform (DFT) bin.

Uplink wireless communication often requires a single transmit-antenna (to simplify the mobile handset) but allows multiple receive-antenna (which can be readily accommodated at a base-station). For such a "single-input multiple-output" (SIMO) scenario, several schemes [67, 68, 79, 80, 81, 97, 108, 125] have been proposed for SC-BB-CP transmission. Among them, [68, 80, 79] allow an *in*sufficient guard interval (GI), and [97] alone can handle co-channel / adjacent-channel interference (but only if these interferers' channel impulse responses are prior known). In contrast, this present work provides both advantages, plus the additional advantages of (a) allowing *un*known channel impulse responses of the

[1] The "Single-Input Single Output" (SISO) part in this chapter is taken from [148], jointly authored by the candidate and his chief supervisor. The "Single-Input Multiple Output" (SIMO) part in this chapter is taken from [164], jointly authored by the candidate, his chief supervisor, and Prof. Yung-Fang CHEN.

*un*known co-channel / adjacent-channel interferences, and (b) allowing *un*known spatio-temporal correlation of any additive noises.

These superior capabilities are achieved in the proposed scheme here by "blind" beamforming, that maximizes the "signal to interference-plus-noise" ratio (SINR) across the multiple receive-antennas. This "max-SINR" *blind* beamforming is predicated on the use of zero-padding in each transmitter symbol-block's *in*sufficient guard interval, which may be shorter than the order of the time-spreading channel. [2] [3]

8.2 Review of Block-Based Cyclically-Prefixed Singe-Carrier Transmission Model

8.2.1 At the Single-Antenna Transmitter

The information-bearing symbols $\{u(j), \forall j\}$ are segmented at the transmitter, into blocks of N symbols. Represent the kth block as an N-element vector, $\mathbf{u}(k) = \left[u_{-\frac{N}{2}+1}(k), \cdots, u_{\frac{N}{2}}(k)\right]^T$, where $u_n(k) = u\left(kN + \frac{N}{2} - 1 + n\right)$, for $n = -\frac{N}{2}+1, \ldots, \frac{N}{2}$.

Prefix $\mathbf{u}(k)$ with a length-G guard interval, which could be a cyclic prefix (CP), i.e. a replication of the last v entries of $\mathbf{u}(k)$. Mathematically, this cyclic-prefixing operation equals the multiplication of $\mathbf{u}(k)$ into an $(N+G)\times N$ cyclic-prefix-insertion matrix $\mathbf{T}_{cp} = \begin{bmatrix} \mathbf{0}_{G\times(N-G)} & \mathbf{I}_G \\ & \mathbf{I}_N \end{bmatrix}$, to produce the $(N+G)$-element vector, $\tilde{\mathbf{u}}(k) = \mathbf{T}_{cp}\mathbf{u}(k)$. This CP serves to reduce or to eliminate up to up to G taps of inter-block interference (IBI), caused by a frequency-selective fading-channel. The guard interval needs not be a cyclic prefix as above, but could be entirely zero-energy symbols, or some mix of the two.

8.2.2 The Channel Fading & Additive Noise

The desired signal is herein modeled to travel through $Q+1$ time-delayed multipaths to each of L receive-antennas [4], where $Q+1 < N+G$. Between the transmit-antenna and the ℓth receive-antenna, the channel is modeled as time-invariant, characterized by a discrete-time impulse-response $\left\{h_0^{(\ell)}, h_1^{(\ell)}, \cdots, h_Q^{(\ell)}\right\}$ of up to order Q.

Consider the kth symbol-block reaching the ℓth receive-antenna. That symbol-block of $N+G$ symbols is corrupted additively by co-channel interference (CCI), adjacent-channel interference (ACI), out-of-system interference, and/or other noises, which are together summed in an $(N+G)\times 1$ vector $\boldsymbol{\eta}^{(\ell)}(k)$, modeled to be zero-mean and statistically independent from $\mathbf{u}(k)$.

[2] Among the earlier cited references, "max-SINR" beamforming is used in only [80], but [80] presumes the total *absence* of all interference and colored noise in the collected data.

[3] Among the earlier cited references, *zero padding* is used in the transmitted signal's guard interval in only [108], which uses *time*-domain equalization, which is the computationally more complicated than the frequency-domain equalization (FDE) here. Moreover, [108] offers none of the advantages mentioned earlier.

[4] For Single-Input Single-Output (SISO) system, $L = 1$. For Single-Input Multiple-Output (SIMO) system, $L \geq 2$.

At the ℓth receive-antenna, that kth symbol-block thus produces the data,

$$\widetilde{\mathbf{r}}^{(\ell)}(k) \;=\; \mathbf{H}_0^{(\ell)} \underbrace{\mathbf{T}_{\rm cp}\mathbf{u}(k)}_{\tilde{\mathbf{u}}(k)} + \mathbf{H}_1^{(\ell)} \underbrace{\mathbf{T}_{\rm cp}\mathbf{u}(k-1)}_{\tilde{\mathbf{u}}(k-1)} + \boldsymbol{\eta}^{(\ell)}(k),$$

where $\mathbf{H}_0^{(\ell)} \in \mathbb{C}^{(N+G)\times(N+G)}$ denotes a lower triangular Toeplitz matrix with its first column equal to $\left[h_0^{(\ell)}, h_1^{(\ell)}, \cdots, h_Q^{(\ell)}, 0, \cdots, 0\right]^T$, $\mathbf{H}_1^{(\ell)} \in \mathbb{C}^{(N+G)\times(N+G)}$ symbolizes an upper triangular Toeplitz matrix with its first row being $[0, \cdots, 0, h_Q^{(\ell)}, \cdots, h_1^{(\ell)}]$, and $\mathbb{C}$ refers to the set of all complex-value numbers.

8.2.3 Processing at the Receive-Antenna

The receiver deletes the cyclic prefix from the received signal, via $\mathbf{R}_{\rm cp} = [\mathbf{0}_{N\times G} \quad \mathbf{I}_{N\times N}]$, to produce an $N \times 1$ vector,

$$\begin{aligned}
\mathbf{x}^{(\ell)}(k) \;&=\; \mathbf{R}_{\rm cp} \underbrace{\left[\mathbf{H}_0^{(\ell)}\tilde{\mathbf{u}}(k) + \mathbf{H}_1^{(\ell)}\tilde{\mathbf{u}}(k-1) + \boldsymbol{\eta}^{(\ell)}(k)\right]}_{=\tilde{\mathbf{r}}^{(\ell)}(k)} \\
&= \underbrace{\left(\mathbf{R}_{\rm cp}\mathbf{H}_0^{(\ell)}\mathbf{T}_{\rm cp} + \mathbf{H}_{\rm ISI}^{(\ell)}\right)}_{=\mathbf{C}^{(\ell)}} \mathbf{u}(k) - \mathbf{H}_{\rm ISI}^{(\ell)}\mathbf{u}(k) \\
&\quad + \mathbf{H}_{\rm IBI}^{(\ell)}\mathbf{u}(k-1) + \mathbf{R}_{\rm cp}\boldsymbol{\eta}^{(\ell)}(k), \qquad (8.1)
\end{aligned}$$

at the ℓth receive-antenna. The above $N \times N$ inter-block interference (IBI) matrix equals

$$\mathbf{H}_{\rm IBI}^{(\ell)} \triangleq \mathbf{R}_{\rm cp}\mathbf{H}_1^{(\ell)}\mathbf{T}_{\rm cp} = \begin{bmatrix} & h_Q^{(\ell)} & \cdots & h_{G+1}^{(\ell)} \\ & \ddots & & \vdots \\ & 0 & \ddots & \vdots \\ \mathbf{0}_{N,N-Q+G} & \vdots & \ddots & h_Q^{(\ell)} \\ & \vdots & \cdots & 0 \end{bmatrix},$$

$$\begin{aligned}
\mathbf{H}_{\rm ISI}^{(\ell)} &\triangleq \mathbf{H}_{\rm IBI}^{(\ell)}\mathbf{P}, \\
\mathbf{P} \;&\triangleq\; \begin{bmatrix} \mathbf{0}_{G\times(N-G)} & \mathbf{I}_G \\ \mathbf{I}_{N-G} & \mathbf{0}_{(N-G)\times G} \end{bmatrix}.
\end{aligned}$$

In (8.1), the $N \times N$ matrix $\mathbf{C}^{(\ell)}$ equals $\mathbf{W}_N^H\mathbf{D}^{(\ell)}\mathbf{W}_N$ and is circulant, regardless of the relative magnitudes of G and Q. Here, $\mathbf{W}_N$ denotes the $N \times N$ discrete Fourier transform (DFT) matrix; and the $N \times N$ matrix $\mathbf{D}^{(\ell)}$ signifies the channel transfer-function matrix, which is diagonal for $G \geq Q$, with its (k,k)th entry equal to the kth DFT coefficient of the channel impulse response $\left\{h_0^{(\ell)}, h_1^{(\ell)}, \cdots, h_Q^{(\ell)}\right\}$ appended by $(N-Q-1)$ zeros. That is, $[\mathbf{D}]_{k,k}^{(\ell)} = \sum_{q=0}^{Q} h_q^{(\ell)} e^{-j\frac{2\pi}{N}kq}$, $\forall k = 0, \ldots, N-1$.

8.3 The Proposed Zero-Inserting Precoder

To suppress the ISI and IBI, but with a length-G *in*sufficient cyclic prefix: [72] proposes inserting $2(Q-G)$ zero-energy symbols to correspond to the $Q-G$ non-zero columns in $\mathbf{H}_{IBI}$

plus the $Q-G$ non-zero columns in $\mathbf{H}_{ISI}$. The present scheme will *not* incur this $2(Q-G)$-symbol overhead, but deploys a guard interval (comprising of zero-energy symbols, plus an optional cyclic prefix) that may be *shorter* than the channel impulse response. From the data received during the zero-energy symbol-intervals, the proposed scheme estimates the combined effects of the signal-of-interest's self-interference, of any multiple-access-user interference, of any overlaid interference, and of the additive noises. This zeros-inserting precoder allows the receiver to subsequently form a data-subgroup containing mostly interference and noise, but little SOI. This will then facilitate the receiver to suppress these very same interference and noise. (This approach has some philosophical resemblance to the null-subcarriers-based method in [84, 101, 127] for OFDM and [126] for SC-FDMA, though the system architectures and the algorithmic details there are very different.)

The present scheme can operate with any non-zero number of zero-energy symbols, with or without a cyclic prefix. This zeros-inserting precoding can be realized by an $N \times (N-P)$ precoding matrix $\mathbf{T}_{zero}$, formed by inserting P number of all-zero rows into an $(N-P) \times (N-P)$ identity matrix. For example, *a*ppending all these zeros would require a precoding matrix of $\mathbf{T}_{zero} = \begin{bmatrix} \mathbf{I}_{(N-P)\times(N-P)} \\ \mathbf{0}_{P\times(N-P)} \end{bmatrix}$.

8.4 The Proposed SISO Receiver

In the Single-Input Single-Output (SISO) architecture, at the receiver, (8.1) remains valid despite the zero-inserting precoder, but now has $\mathbf{u}(k) = \mathbf{T}_{zero}\mathbf{s}(k)$. Moreover, the superscript $^{(\ell)}$, which appears in Sections 8.2.2-8.2.3, will be removed in this section as $L = 1$ in SISO receiver. The proposed linear equalizer involves a post-FFT linear single-tap-per-subcarrier *frequency*-domain equalizer (FDE) $\mathbf{W}$, followed by a post-IFFT signal-to-interference-and-noise (SINR) maximizer in the *time*-domain. These are shown in Figure 8.1.

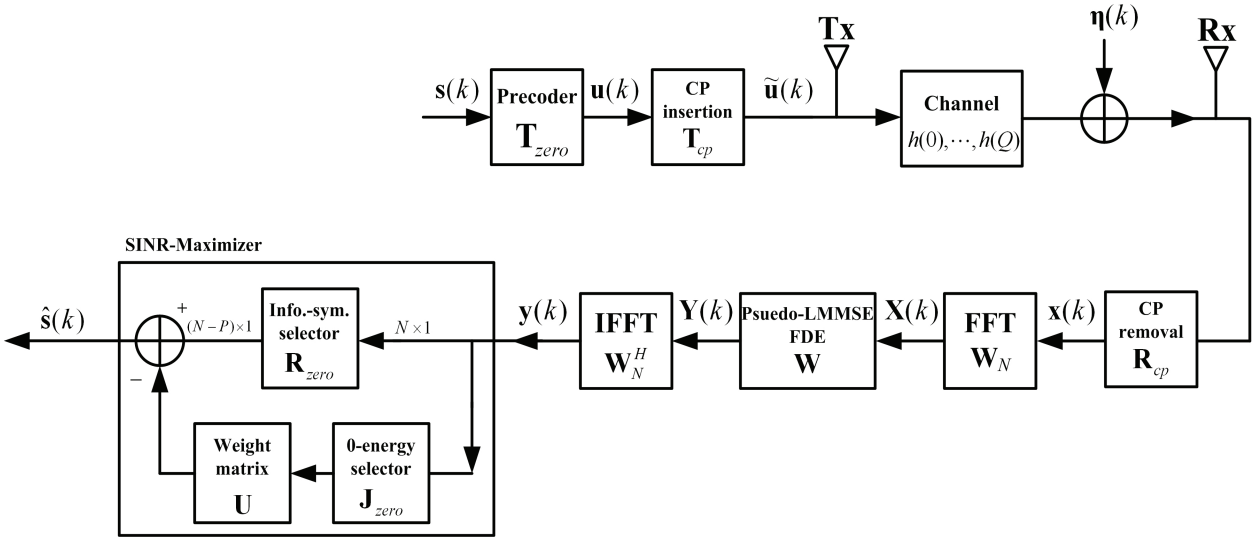

Figure 8.1: The proposed zero-inserting precoder and the proposed two-stage equalizer for SISO SC-CP system.

8.4.1 Linear Minimum Mean-Square-Error (LMMSE) Frequency-Domain Equalization (FDE)

The first stage is a single-tap-per-subcarrier frequency-domain linear equalizer (FDE),

$$\mathbf{W} \;=\; \mathbf{D}^H \left(\mathbf{D}\mathbf{D}^H + \frac{1}{\mathrm{SNR}} \mathbf{I}_N \right)^{-1}, \tag{8.2}$$

where superscript ^{H} denotes complex-conjugate transposition, $\mathrm{SNR} \stackrel{\mathrm{def}}{=} \frac{\sigma_s^2}{\sigma_n^2}$, σ_s^2 refers to the signal power, and σ_n^2 symbolizes the noise power. The $N \times N$ diagonal $\mathbf{W}$ of (8.2) reduces the signal-of-interest's energy in the zero-energy symbol-intervals. (This $\mathbf{W}$ would constitute a linear minimum-mean-square-error (LMMSE) equalizer, if no interference existed and if $G \geq Q$.) The output of $\mathbf{W}$ equals

$$\mathbf{y}(k) \;=\; \mathbf{W}_N^H \mathbf{W} \mathbf{W}_N \underbrace{\left\{ \mathbf{C}\mathbf{u}(k) - \mathbf{H}_{ISI}\mathbf{u}(k) + \mathbf{H}_{IBI}\mathbf{u}(k-1) + \mathbf{n}(k) \right\}}_{=\mathbf{x}(k)}. \tag{8.3}$$

8.4.2 SINR-Maximizer

For the second stage:

(a) Form a $P \times N$ "zero-*selection*" matrix, to block all information-bearing symbol-intervals (which have non-zero energy at transmission). E.g., $\mathbf{J}_{zero} = \left[\mathbf{0}_{P\times(N-P)} \middle| \mathbf{I}_{P\times P} \right]$ would be compatible with the earlier defined $\mathbf{T}_{zero}$.

(b) Also form a $(N-P) \times N$ "zero-*removal*" matrix, to remove the precoder-inserted zeros. E.g., $\mathbf{R}_{zero} = \left[\mathbf{I}_{(N-P)\times(N-P)} \middle| \mathbf{0}_{(N-P)\times P} \right]$ would be compatible with the earlier defined $\mathbf{T}_{zero}$ and $\mathbf{J}_{zero}$.

Next, form the $(N-P) \times P$ matrix $\mathbf{U}$, to minimize the mean-squared error ξ between the signal-output from $\mathbf{R}_{zero}$ and $\mathbf{J}_{zero}$, i.e.

$$\xi_{\mathbf{min}} \;=\; \min_{\mathbf{U}} \underbrace{E\left[\left\| \mathbf{i}(k) - \mathbf{U}\mathbf{J}_{zero}\mathbf{y}(k) \right\|_2^2 \right]}_{\triangleq \xi}, \tag{8.4}$$

where $\mathbf{i}(k) \triangleq \mathbf{R}_{zero}\mathbf{W}_N^H \mathbf{W}\mathbf{W}_N \left[-\mathbf{H}_{ISI}\mathbf{u}(k) + \mathbf{H}_{IBI}\mathbf{u}(k-1) + \mathbf{n}(k) \right]$ represents the interference and noises in the information-bearing symbols' durations. The optimization in (8.4) can be solved via the principle of orthogonality, i.e. $E[\mathbf{U}\mathbf{J}_{zero}\mathbf{y}(k)\ (\mathbf{i}(k) - \mathbf{U}\mathbf{J}_{zero}\mathbf{y}(k))^H] = \mathbf{0}$, to yield
$\mathbf{U} = \mathbf{R}_{zero}\mathbf{R}_{\mathbf{i}(k)\mathbf{i}(k)}\mathbf{J}_{zero}^H \left[\mathbf{J}_{zero}\mathbf{R}_{\mathbf{y}(k)\mathbf{y}(k)}\mathbf{J}_{zero}^H \right]^{-1}$, which may be pre-calculated off-line, using the prior knowledge that

$$\begin{aligned} \mathbf{R}_{\mathbf{i}(k)\mathbf{i}(k)} \triangleq\; & \mathbf{W}_N^H \mathbf{W}\mathbf{W}_N \left\{ \mathbf{H}_{ISI}\mathbf{R}_{\mathbf{u}(k)\mathbf{u}(k)} (\mathbf{W}_N^H \mathbf{W}\mathbf{W}_N \mathbf{H}_{ISI})^H \right. \\ & \left. + \mathbf{H}_{IBI}\mathbf{R}_{\mathbf{u}(k-1)\mathbf{u}(k-1)} (\mathbf{W}_N^H \mathbf{W}\mathbf{W}_N \mathbf{H}_{IBI})^H + \mathbf{R}_{\mathbf{n}(k)\mathbf{n}(k)} (\mathbf{W}_N^H \mathbf{W}\mathbf{W}_N)^H \right\} \end{aligned} \tag{8.5}$$

Lastly, the $(N-P) \times 1$ transmitted symbol-vector $\mathbf{s}(k)$ is estimated by the receiver as $\hat{\mathbf{s}}(k) = (\mathbf{R}_{zero} - \mathbf{U}\mathbf{J}_{zero})\, \mathbf{y}(k)$.

Table 8.1: The proposed scheme's computational complexity, versus that of the customary LMMSE-FDE

	LMMSE-Based FDE	The Proposed 2-Stage Equalizer
# of complex-value multiplications	$N \log_2 N + N$	$N \log_2 N + N + (N-P)P$
# of complex-value additions	$2N \log_2 N$	$2N \log_2 N + (N-P)P$

The real-time computational complexity of this proposed precoder/equalizer scheme is compared in Table 8.5 against the customary LMMSE-FDE (i.e. (8.2) alone, without the precoder and without the SINR-maximizer) in terms of N and P. As $\mathbf{W}$ and $\mathbf{U}$ may be pre-computed off-line, while $\mathbf{T}_{zero}$, $\mathbf{R}_{zero}$ and $\mathbf{J}_{zero}$ involve no multiplication nor addition – these do not contribute to the real-time computational load.

8.5 Monte Carlo Simulations for SISO Receiver

The information-bearing symbols $\{s(k)\}$ are modulated with equi-probable QPSK-symbols. The transmitted signal has $N = 64$. The channel impulse response has $Q + 1 = 11$ complex-valued taps, each randomly generated and not cross-correlated among themselves. Each tap's real-value part and imaginary-value part are not cross-correlated. Each tap is Gaussian, zero-mean. The qth tap has an exponentially decaying variance of $\sigma_q^2 = \left(1 - e^{-\frac{T_s}{T_{RMS}}}\right) e^{-q\frac{T_s}{T_{RMS}}}, \forall q = 0, \cdots, Q$, where T_s denotes the sampling period, and T_{RMS} symbolizes the root-mean-square delay-spread of the channel. The additive noise is complex-value, temporally uncorrelated, zero-mean, Gaussian, with a noise power of $\sigma^2_{\boldsymbol{\eta}(k)\boldsymbol{\eta}(k)}$.

Consider these two curves in Figure 8.2:

(i) The top dashed black curve at $G = 6$ and $P = 0$ (i.e. an insufficient CP but no zeros-inserting precoding).

(ii) The bottom green curve at $G = 0$ and $P = 6$ (i.e. no CP but 6 zeros-inserted by the precoder, as proposed in this chapter).

These two curves both incur a same overhead of $P + G = 6$ symbols, but the proposed scheme lowers the BER by $1 - \frac{9\times10^{-4}}{3.8\times10^{-3}} = 76\%$ at SNR= 15dB, and by $1 - \frac{3.2\times10^{-5}}{1.4\times10^{-3}} = 98\%$ at SNR= 25dB. In terms of the computational complexity for case (ii) above, Table suggests that the proposed scheme would increase the popular LMMSE-FDE method's number of complex-value multiplications by 60% and the number of complex-value additions by 45%.

Alternatively, if the transmission overhead is lightened to just 4 inserted zeros (i.e. $\frac{(6+64)-(4+64)}{6+64} = 2.9\%$ reduction overhead on the data-rate) but no cyclic prefix, then the proposed scheme can still lower the BER by $1 - \frac{2.9\times10^{-3}}{3.8\times10^{-3}} = 24\%$ at SNR= 15dB, and by $1 - \frac{7.8\times10^{-4}}{1.4\times10^{-3}} = 44\%$ at SNR= 25dB.

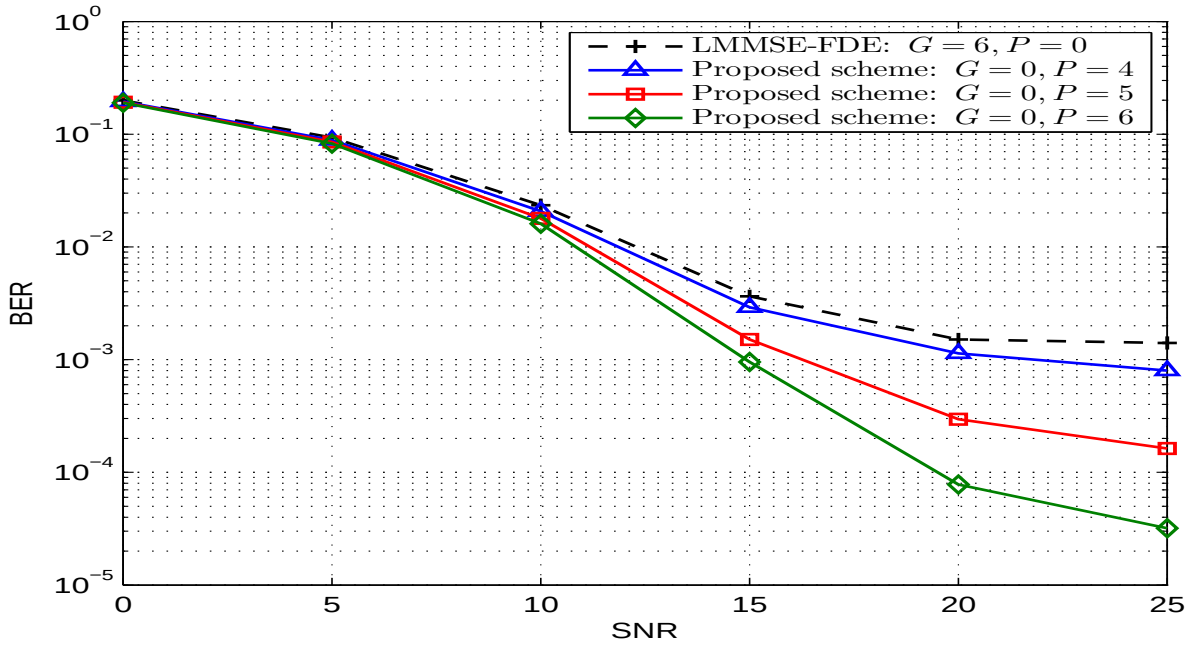

Figure 8.2: The BER of the proposed scheme 's BER performance of the proposed algorithm Ib with P zero-energy symbols inserted at the end of symbol-block v.s. MMSE-FDE with length of $G = 6$ CP inserted where $P \leq G$. The channel has an exponential decay with $\frac{T_s}{T_{rms}} = \frac{1}{4}$.

8.6 The Proposed SIMO Receiver

An SIMO-beamforming receiver will be proposed here, for use with a GI that can be *in*sufficient (despite the zero padding) as described earlier in Section 8.3. This L-sensor receiver will first equalize the SOI separately at each sensor in the frequency-domain, before "blind" spatial beamforming to constructively sum the SOI's multipaths and to suppress any a priori *un*known co-channel interference, adjacent-channel interference, and/or spatio-temporally colored noises.

8.6.1 Pseudo Linear Minimum Mean-Square-Error (LMMSE) Frequency-Domain Equalization (FDE) at Each Sensor

At the ℓth sensor, the received data is first processed by *some* frequency-domain equalizer (FDE), apart from other sensor's data. *Any* FDE could do. The purpose here is to "clear" the nominally zero-energy intervals of the received data of any SOI energy. These zero-energy intervals contain no SOI energy at *transmission*, but the channel's temporal spreading has "smeared" SOI energy onto these nominally zero-energy intervals at *reception*. When these nominally zero-energy intervals are again cleared of the SOI energy, they could contain only the interferences and the noises, thereby facilitating subsequent "blind" estimation of these same interferences and noises.

Although any FDE could be used, one possibility is a pseudo "linear minimum mean-square-error" (LMMSE) FDE[5]

$$\mathbf{W}^{(\ell)} = [\mathbf{D}^{(\ell)}]^H \left(\mathbf{D}^{(\ell)}[\mathbf{D}^{(\ell)}]^H + \frac{1}{\text{SNR}}\mathbf{I}_N \right)^{-1}, \tag{8.6}$$

which is an $N \times N$ diagonal matrix. In the above, the superscript ^{H} denotes the Hermitian operation, and SNR refers to the signal-to-noise power ratio in linear scale (not in dB). This pseudo-LMMSE FDE would be exactly LMMSE, if there exists no co-channel / adjacent-channel / out-of-system interference, and if the additive noise is temporally white, as in the data models presumed in [67, 68, 79, 125, 148]. This pseudo-LMMSE FDE has NOT presumed *any* prior knowledge of any spatio-temporal statistics of any co-channel interference, any adjacent-channel interference, and/or any noises. Subsequently presented Monte Carlo simulations will show that this pseudo-LMMSE FDE can nonetheless clear the nominally zero-energy intervals of the smeared SOI energy, adequately so.

The FDE would output

$$\mathbf{y}^{(\ell)}(k) \;=\; \mathbf{W}_N^H \mathbf{W}^{(\ell)} \mathbf{W}_N \mathbf{x}^{(\ell)}(k).$$

[5]Other possibilities include the "zero forcing" (ZF) FDE, obtainable from (8.6) by setting the "SNR" parameter to ∞.

8.6.2 Eigen-Based Spatial Beamforming in the *Time*-Domain

At each "zero-energy" symbol ("zero-energy" at transmission) in kth symbol-block, form the $L \times 1$ *spatial* snapshot,

$$\mathbf{y}_p(k) \quad = \quad \left[y_p^{(1)}(k), y_p^{(2)}(k), \ldots, y_p^{(L)}(k) \right]^T , \tag{8.7}$$

$\forall p \in \{N-P+1, \ldots, N\}$. In the above, the superscript ^{T} refers to transposition. Over K symbol-blocks, the $L \times L$ "interference plus noise" (I+N) *spatial* correlation matrix is estimated as

$$\mathbf{R}_{\text{I+N}} \quad = \quad \frac{1}{KP} \sum_{k=1}^{K} \sum_{p=N-P+1}^{N} \mathbf{y}_p(k) \left(\mathbf{y}_p(k)\right)^H . \tag{8.8}$$

On the other hand, the symbol-block's remaining $N-P$ symbols would contain the signal-of-interest, any interference, and noise. Hence, similar to (8.7) and (8.8), the $L \times L$ "signal plus interference and noise" (S+I+N) *spatial* correlation matrix is estimated as

$$\mathbf{R}_{\text{S+I+N}} \quad = \quad \frac{1}{K(N-P)} \sum_{k=1}^{K} \sum_{p=1}^{N-P} \mathbf{y}_p(k) \left(\mathbf{y}_p(k)\right)^H .$$

Then compute the generalized eigenvector corresponding to the largest-magnitude generalized eigenvalue of the matrix pencil $\{\mathbf{R}_{\text{S+I+N}}, \mathbf{R}_{\text{I+N}}\}$, to yield the spatial beamformer weight vector $\mathbf{w}_{\text{opt}}$ that maximizes the "signal to interference-and-noise ratio" (SINR): (Please see Section IV-C in [13])

$$\begin{aligned} \text{SINR}(\mathbf{w}) \quad &= \quad \frac{\mathbf{w}^H \{\mathbf{R}_{\text{S+I+N}} - \mathbf{R}_{\text{I+N}}\} \mathbf{w}}{\mathbf{w}^H \mathbf{R}_{\text{I+N}} \mathbf{w}} \\ &= \quad \frac{\mathbf{w}^H \mathbf{R}_{\text{S+I+N}} \mathbf{w}}{\mathbf{w}^H \mathbf{R}_{\text{I+N}} \mathbf{w}} - 1. \end{aligned}$$

This spatial beamformer outputs an $1 \times N$ symbol-vector

$$\mathbf{z}(k) \quad = \quad \frac{\mathbf{w}_{\text{opt}}^H \mathbf{Y}(k)}{\|\mathbf{w}_{\text{opt}}\|},$$

where $\|\cdot\|$ represents the Frobenius norm, and $\mathbf{Y}(k) = \left[\mathbf{y}^{(1)}(k), \mathbf{y}^{(2)}(k), \cdots, \mathbf{y}^{(L)}(k)\right]$.

The earlier equalization stage of Section 8.6.1 is essential to this beamforming stage here. Otherwise, the data at the nominally zero-padding interval would still contain such a significant amount of the SOI that $\mathbf{R}_{I+N}$ would be erroneously estimated thereof, causing the spatial beamformer to erroneously null much of the SOI, while erroneously passing much of the "I+N".

8.7 Monte Carlo Simulations for SIMO Receiver

Figure 8.3 presents Monte Carlo simulations that verify the proposed scheme's efficacy despite an insufficient "guard interval", that requires only an overhead of $P+G$ (i.e. P inserted zeroes plus a G-length of cyclic prefix), shorter than a channel order of Q.

Figure 8.3 shows the proposed scheme's bit-error rate (BER) below those of a equal-weight beamformer and of a single receive-antenna. [6]

The simulation settings are as follows:

1. The signal-of-interest's (SOI) information-bearing symbols are QPSK-modulated and equi-probable. The transmitted signal has $N = 64$ symbol-periods per symbol-block. The channel impulse response's $Q + 1 = 7$ complex-valued taps are each randomly generated, with each tap's real-value part and imaginary-value part not cross-correlated and each white, Gaussian, zero-mean, with a variance of $\sigma_q^2 = e^{-q\frac{T_s}{T_{\text{RMS}}}}$, $\forall q = 0, \ldots, Q$, where T_s denotes the sampling period, T_{RMS} symbolizes the root-mean-square (RMS) delay-spread of the channel, set here at $T_s = T_{\text{RMS}}$.

2. The receiver has $L = 5$ half-wavelength spaced isotropic sensors. The desired signal's $Q + 1 = 7$ time-delayed multipaths respectively have the directions-of-arrival $\theta_0 = -10°$, $\theta_1 = 0°$, $\theta_2 = -20°$, $\theta_3 = 40°$, $\theta_4 = 75°$, $\theta_5 = 60°$, $\theta_6 = 45°$ relative to the normal to the array-axis.

3. There is 1 CCI source, of the same time-frequency structure and statistical properties as the SOI. This CCI's channel is statistically identical as (but statistically independent from) the SOI's channel, except that the CCI's $Q + 1 = 7$ time-delayed multipaths arrive at 50°, 10°, 60°, 20°, −15°, 0°, and 55°. This CCI has a 8-symbol-period arrival-delay relative to the SOI.

4. There is 1 ACI source, of the same temporal structure and statistical properties as the SOI, except that its carrier-frequency is 1.25× that of the SOI. This ACI's channel is statistically identical as (but statistically independent from) the SOI's channel, except that the ACI's $Q + 1 = 7$ time-delayed multipaths arrive at 40°, −50°, 30°, −10°, 5°, 65°, and 75°. This ACI has a 10-symbol-period arrival-delay relative to the SOI.

5. The additive noise is complex-value, spatio-temporally correlated, with a constant power. The $(N + G) \times L$ matrix $\mathbf{N} = \left[\boldsymbol{\eta}^{(1)}(k), \cdots, \boldsymbol{\eta}^{(L)}(k)\right] \cdot \mathbf{D}$ of spatio-temporally colored noise is generated as $\mathbf{N} = \mathbf{U}_{N+G,N+G}\mathbf{G}\mathbf{U}_{L,L}$. Here, $\mathbf{U}_{J,K}$ is a $J \times K$ matrix of statistically independent complex-value entries, each having a real-value part and an imaginary part statistically independent from each other, but with each part uniformly distributed in $[0, 1]$. Likewise, $\mathbf{G}$ is an $(N + G) \times L$ matrix of statistically independent complex-valued entries, each circularly complex Gaussian distributed, with a zero mean and unit variance. Lastly, $\mathbf{D}$ is an $L \times L$ diagonal matrix, whose ℓth entry equals (SNR $\|\boldsymbol{\eta}^{(ell)}(k)\|$), where $\|\cdot\|$ denotes the Frobenius norm of the entry inside.

[6] Figure 8.3 has no curve at $P = 0$ for the SINR-maximization beamformer, because $P = 0$ would mean no zero-energy symbol inserted, thereby precluding the formation of any $\mathbf{R}_{I+N}$ to realize any SINR-maximization beamformer in (8.9).

6. Each data-point on Figure 8.3 is based on 500 independent Monte Carlo experiments, each involving 600 symbol-blocks, which are processed as 12 consecutive groups of $K = 50$ symbol-blocks. The bit-error rate (BER) is calculated by considering the QPSK's real-value part and imaginary-part each as a separate bit.

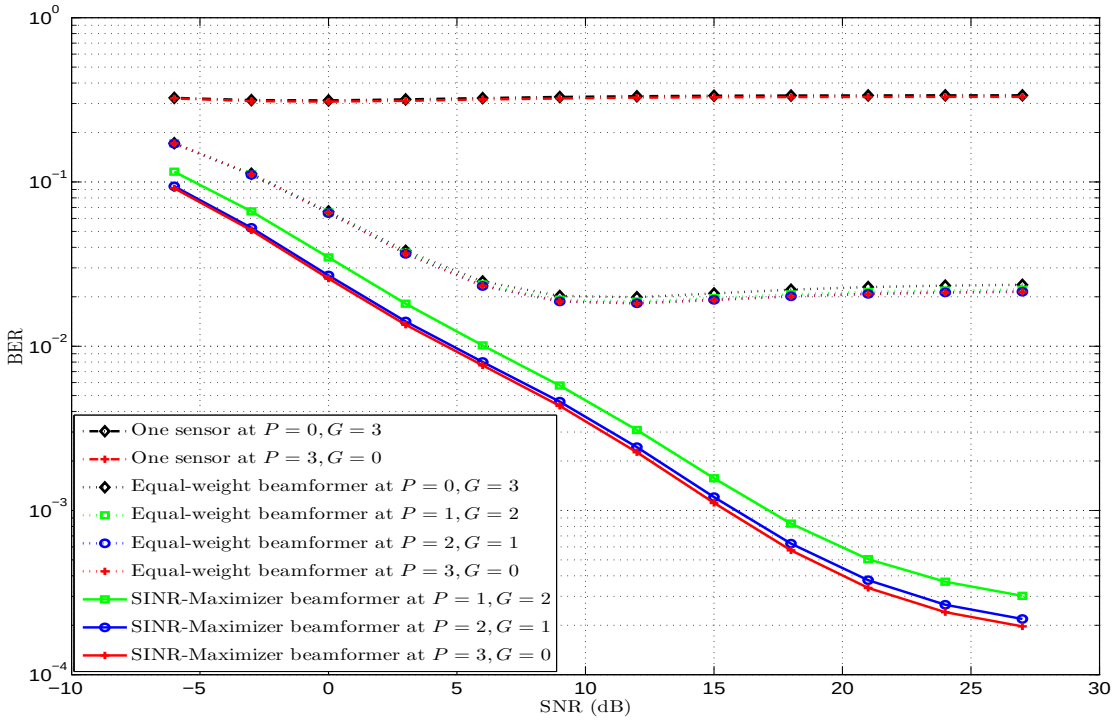

Figure 8.3: Monte Carlo simulations verify the efficacy of proposed *in*sufficient-GI "max-SINR"-beamforming scheme.

These simulations verify the proposed scheme's efficacy in handling CCI and/or ACI of *un*known channel impulse responses and in handling additive noises of *un*known spatio-temporal correlation, despite allowing an *in*sufficient guard interval to reduce the overhead in transmission.

Moreover, Figure 8.3 shows that the more zero-padding replaces cyclic-prefixing in the insufficient GI, the lower the BER is. This is because more zero-padding allows more observation of the interferences and the noises in the near-absence of the SOI, hence a more accurate estimate of $\mathbf{R}_{I+N}$, thereby better spatial beamforming, to reject the "I+N" and to constructively sum the SOI's multipaths.

8.8 Summary

For SISO / SIMO cyclic-prefixed block-based single-carrier-based communication systems, at the transmitter, this chapter proposes a zero-inserting time-domain precoder which allows observation of the interferences and the noises, then facilitate the receiver to suppress these very same interference and noise. Section 8.4 introduces a two-stage equalizer for a

single receiver antenna, to allow an insufficient guard interval, in order to reduce the transmission overhead. Section 8.6 extends the single-input single-output (SISO) architecture used in Section 8.4 to multiple receive-antennas, for the additional capabilities of "blind" spatial focusing towards the signal-of-interest (SOI) and "blind" spatial suppression of any unknown co-channel / adjacent-channel / out-of-system interferences impinging from unknown directions-of-arrival.

Chapter 9

Conclusion

Chapters 2-7 introduce six contributions towards hydrophone-array signal processing.

chapter 2 presents azimuth-elevation direction-finding closed-form formulas to estimate an incident source's azimuth-elevation angle-of-arrival (AOA), for various combinations of *higher-order* directional acoustic sensors, that are orthogonally oriented in a collocated triad. Also identified are the validity-regions for *un*ambiguous estimation of the azimuth-elevation arrival-angle. In contrast, Chapters 3-7 concerns only the zero-order acoustic sensor (i.e. acoustic pressure sensor) and/or the first-order acoustic sensor (i.e. acoustic particle-*velocity* sensor).

The works presented in chapters 2, 5-7 are based on the collocated geometry of acoustic vector-sensor, while chapters 4 and 3 allows the acoustic vector-sensor's component-sensors to be spread out arbitrarily in the three-dimensional space. Specifically, chapter 3 proposes a new direction-finding algorithm to allow the acoustic vector-sensor's four component-sensors to be spatially separated over a general array-grid, perhaps with a much extended spatial aperture, thereby improving direction-finding accuracy while mitigating hardware implementation difficulties in spatially collocating the three velocity-sensors at one point in space. One shortcoming of the direction-finding algorithm introduced in chapter 3, however, is its requirement of a pressure sensor, to be deployed along with the three uni-axial velocity sensors. This would be problematic for *near*-field localization to estimate the emitter's radial distance from the "acoustic vector sensor", in addition to the emitter's azimuth-elevation angle-of-arrival, because the pressure sensor's data differ from the uni-axial velocity sensors' data by a distance-dependent frequency-dependent magnitude-scaling factor and by a distance-dependent frequency-dependent complex phase [135], though these factors arise only for an emitter lying in the *near*-field of the acoustic vector sensor. Chapter 4 shows how the direction-finding of incident emitters can be achieved using three orthogonally oriented uni-axial velocity sensors which are spatially separated.

Chapter 5 advances the first algorithm in the open literature (to the best of the authors' knowledge) to "blindly" calibrate the intra-acoustic-vector-sensor gain-uncertainty, as well as the inter-acoustic-vector-sensor dislocation and mis-orientation, that may exist in a distributed array of acoustic vector-sensors. The proposed algorithm is computationally

simpler than maximum-likelihood estimation by orders-of-magnitude.

Chapter 6 derives approximate lower bounds for azimuth-elevation direction-of-arrival estimation using an acoustic vector sensor whose component sensors are individually subject to failure. This approximate lower bound equals a weighted sum of Cramér-Rao bounds, conditioned on disjoint events of sensor breakdown, that together define the overall phenomenon of random sensor breakdown. Its tightness is verified by Monte Carlo simulation of a maximum likelihood estimator.

The *near*-field wideband source localization problem is addressed using an acoustic vector-sensor by chapter 7, which develops a parameter estimation algorithm to localize a near field source, emitting a signal of unknown spectrum, based on data collected by one acoustic vector sensor, corrupted additively by white noise or by unknown colored noise.

Chapter 8 introduce two contributions towards signal processing for single-carrier block-based transmission/reception.

Chapter 8 first proposes a zero-inserting time-domain precoder, which allows observation of the interferences and the noises, then facilitate the receiver to suppress these very same interference and noise for both single-input single-output (SISO) and single-input multiple-output SIMO receivers. From the data received during the zero-energy symbol-intervals, Section 8.4 introduces a two-stage equalizer for a single receiver antenna, to estimates the combined effects of the signal-of-interests self-interference, of any multiple-access-user interference, of any overlaid interference, and of the additive noises. These denigrating effects are then subtracted from the information-bearing parts of the symbol-block, via a SINR-maximizer in the receiver. Section 8.6 extends the SISO architecture used in Section 8.4 to multiple receive-antennas. The multiple receiver-sensors will first equalize the SOI separately at each sensor in the frequency domain, before "blind" spatial beamforming to constructively sum the SOIs multipaths and to suppress any a priori unknown co-channel interference, adjacent-channel interference, and/or spatio-temporally colored noises.

Bibliography

[1] H. F. Olson, "Gradient Microphones" *Journal of the Acoustical Society of America*, vol. 17, no. 3, pp. 192-198, January 1946.

[2] C. B. Leslie, J. M. Kendall & J. L. Jones, "Hydrophone for Measuring Particle Velocity," *Journal of the Acoustical Society of America*, vol. 28, no. 4, pp. 711-715, July 1956.

[3] B. R. Beavers & R. Brown, "Third Order Gradient Microphone for Speech Reception," *Journal of the Audio Engineering Society*, vol. 18, no. 6, pp. 636-640, December 1970.

[4] S.-H. Ko, G. A. Brigham & J. L. Butler, "Multimode Spherical Hydrophone," *Journal of the Acoustical Society of America*, vol. 56, no. 6, pp. 1890-1898, December 1974.

[5] G. M. Sessler & J. E. West, "Second-Order Gradient Unidirectional Microphones Utilizing an Electret Transducer," *Journal of the Acoustical Society of America*, vol. 58, no. 1, pp. 273-278, July 1975.

[6] J. L. Butler & S. L. Ehrlich, "Superdirective Spherical Radiator," *Journal of the Acoustical Society of America*, vol. 61, no. 6, pp. 1427-1431, June 1977.

[7] C. L. LeBlanc, *Handbook of Hydrophone Element Design Technology*, Naval Underwater Systems Center Technical Report 5813, 1978.

[8] Y. Ishigaki, M. Yamamoto, K. Totsuka & N. Miyaji, "Zoom Microphone," *Audio Engineering Society Convention*, p. 1713, 1980.

[9] A. J. Brouns, "Second-Order Gradient Noise-Cancelling Microphone," *IEEE International Conference on Acoustics, Speech, and Signal Processing*, pp. 786-789, 1981.

[10] Mati Wax, Tie-Jun Shan, & Thomas Kailath, "Spatio-temporal spectral analysis by eigenstructure methods ," *IEEE Transactions on Acoustics, Speech and Signal Processing*, vol. 32, no. 4, pp. 817-827, Aug 1984.

[11] M. A. Josserand & C. Maerfeld, "PVF2 Velocity Hydrophone," *Journal of the Acoustical Society of America*, vol. 78, no. 3, pp. 860-867, 1985.

[12] V. J. Hughes, J. G. Boulton, J. M. Coles, T. R Empson & N. J. Kerry, "Why an Optically-Based Hydrophone Works Better," *Sensor Review*, vol. 7, no. 3, pp. 123-126, July 1987.

[13] B. D. Van Veen & K. M. Buckley, "Beamforming: A Versatile Approach to Spatial Filtering," *IEEE Acoustics, Speech & Signal Processing Magazine*, vol. 5, no. 2, pp. 4-24, April 1988.

[14] R. Roy & T. Kailath, "ESPRIT - Estimation of Signal Parameters via Rotational Invariance Techniques," *IEEE Transactions of Acoustics, Speech, and Signal Processing*, vol. 37, pp. 984C995, July 1989.

[15] A. D. Pierce, *Acoustics—An Introduction to its Physical Principles and Applications.* New York: McGraw-Hill, 1989.

[16] G. L. D'Spain, W. S. Hodgkiss & G. L. Edmonds, "Energetics of the Deep Ocean's Infrasonic Sound Field," *Journal of the Acoustical Society of America*, vol. 89, no. 3, pp. 1134-1158, March 1991.

[17] G. L. D'Spain, W. S. Hodgkiss & G. L. Edmonds, "The Simultaneous Measurement of Infrasonic Acoustic Particle Velocity and Acoustic Pressure in the Ocean by Freely Drifting Swallow Floats," *IEEE Journal of Oceanic Engineering*, vol. 16, no. 1, pp. 195-207, April 1991.

[18] V. A. Shchurov, "Coherent and Diffuse Fields of Underwater Acoustic Ambient Noise," *Journal of the Acoustical Society of America*, vol. 90, no. 2, part 1, pp. 991-1001, August 1991.

[19] V. A. Shchurov, V. I. Ilyichev, V. P. Kuleshov & M. V. Kuyanova, "The interaction of Energy Flows of Underwater Ambient Noise and a Local Source," *Journal of the Acoustical Society of America*, vol. 90, no. 2, part 1, pp. 1002-1004, August 1991.

[20] "Acoustic Doppler Current Profiler Performance in Near Surface and Bottom Boundaries," *IEEE Journal of Oceanic Engineering*, vol. 16, no. 4, pp. 390-396, October 1991.

[21] J. C. Nickles, G. L. Edmonds, R. A. Harriss, F. H. Fisher, W. S. Hodgkiss, J. Giles & G. D'Spain, "A Vertical Array of Directional Acoustic Sensors," *IEEE Oceans Conference*, vol. 1, pp. 340-345, 1992.

[22] G. L. D'Spain, W. S. Hodgkiss, G. L. Edmonds, J. C. Nickles, F. H. Fisher & R. A. Harriss, "Initial Analysis of The Data From The Vertical DIFAR Array," *IEEE Oceans Conference*, vol. 1, pp. 346-351, 1992.

[23] G. C. Chen & W. S. Hodgkiss, "VLF Source Localization with a Freely Drifting Acoustic Sensor Array," *IEEE Journal of Oceanic Engineering*, vol. 18, no. 3, pp. 209-223, July 1993.

[24] Steven M. Kay, *Fundamentals of Statistical Signal Processing, Volume I: Estimation Theory* Prentice-Hall, 1993.

[25] V. A. Shchurov, V. I. Ilyichev & V. P. Kuleshov, "Ambient Noise Energy Motion in the Near Surface Layer in Ocean Wave-Guide," *Journal de Physique*, vol. 4, no. 5, part 2, pp. 1273-1276, May 1994.

[26] A. Nehorai & E. Paldi, "Acoustic Vector-Sensor Array Processing," *IEEE Transactions on Signal Processing*, vol. 42, no. 10, pp. 2481-2491, September 1994.

[27] G. L. D'Spain, "Relationship of Underwater Acoustic Intensity Measurements to Beamforming," *Canadian Acoustics*, vol. 22, part 3, pp. 157-158, September 1994.

[28] F. Desharnals & G. L. D'Spain, "Acoustic Intensity Measurements with Swallow Floats," *Canadian Acoustics*, vol. 22, part 3, pp. 159-160, September 1994.

[29] B. Hochwald & A. Nehorai, "Identifiability in Array Processing Models with Vector-Sensor Applications," *IEEE Transactions on Signal Processing*, vol. 44, no. 1, pp. 83-95, January 1996.

[30] M. J. Berliner & J. F. Lindberg, *Acoustical Particle Velocity Sensors: Design, Performance and Applications*, Woodbury, New York, U.S.A.: AIP Press, 1996.

[31] D. Lubman, "Antifade Sonar Employs Acoustic Field Diversity to Recover Signals from Multipath Fading," in *Acoustical Particle Velocity Sensors: Design, Performance and Applications*, pp. 335-344, Woodburg, New York, U.S.A.: AIP Press, 1996.

[32] P. J. Stein, S. E. Euerle, R. K. Menoche & R. E. Janiesch, "Pressure Gradient Sensors for Bearing Determination in Shallow Water Tracking Ranges," in *Acoustical Particle Velocity Sensors: Design, Performance and Applications*, pp. 359-373, Woodburg, New York, U.S.A.: AIP Press, 1996.

[33] K. T. Wong & M. D. Zoltowski, "Closed-form Underwater Acoustic Direction-Finding with Arbitrarily Spaced Vector-Hydrophones at Unknown Locations," *IEEE Journal of Oceanic Engineering*, vol. 22, no. 3, pp. 566-575, July 1997.

[34] K. T. Wong & M. D. Zoltowski, "Extended-Aperture Underwater Acoustic Multi-source Azimuth/Elevation Direction-Finding Using Uniformly But Sparsely Spaced Vector Hydrophones," *IEEE Journal of Oceanic Engineering*, vol. 22, no. 4, pp. 659-672, October 1997.

[35] M. Hawkes & A. Nehorai, "Acoustic Vector-Sensor Beamforming and Capon Direction Estimation," *IEEE Transactions on Signal Processing*, vol. 46, no. 9, pp. 2291-2304, September 1998.

[36] G. S. Kang & D. A. Heide, "Acoustic Noise Reduction for Speech Communication (Second-Order Gradient Microphone)," *IEEE International Symposium on Circuits and Systems*, vol. 4, pp. 556-559, 1999.

[37] V. A. Shchurov & M. V. Kuyanova, "Use of Acoustic Intensity Measurements in Underwater Acoustics (Modern State and Prospects)," *Chinese Journal of Acoustics*, vol. 18, no. 4, pp. 315-326, 1999.

[38] M. Hawkes & A. Nehorai, "Effects of Sensor Placement on Acoustic Vector-Sensor Array Performance," *IEEE Journal of Oceanic Engineering*, vol. 24, no. 1, pp. 33-40, January 1999.

[39] A. Nehorai & P. Tichavský, "Cross-Product Algorithms for Source Tracking Using an EM Vector Sensor," *IEEE Transactions on Signal Processing*, vol. 47, no. 10, pp. 2863-2867, October 1999.

[40] K. T. Wong & M. D. Zoltowski, "Root-MUSIC-Based Azimuth-Elevation Angle-of-Arrival Estimation with Uniformly Spaced but Arbitrarily Oriented Velocity Hydrophones," *IEEE Transactions on Signal Processing*, vol. 47, no. 12, pp. 3250-3260, December 1999.

[41] H.-E. de Bree, W. F. Druyvesteyn, E. Berenschot & M. Elwenspoek, "Three-Dimension Sound Intensity Measurements Using Microflown Particle Velocity Sensors," *IEEE International Conference on Electro Mechanical Systems*, pp. 124-129, 1999.

[42] P. C. Hines, A. L. Rosenfeld, B. H. Maranda & D. L. Hutt, "Evaluation of the Endfire Response of a Superdirective Line Array in Simulated Ambient Noise Environments," *IEEE Oceans Conference*, vol. 3, pp. 1489-1292, 2000.

[43] A. L. Butler, J. L. Butler, W. L. Dalton & J. A. Rice, "Multimode Directional Telesonar Transducer," *IEEE Oceans Conference*, vol. 2, pp. 1289-1292, 2000.

[44] K. T. Wong & M. D. Zoltowski, "Self-Initiating MUSIC-Based Direction Finding in Underwater Acoustic Particle Velocity-Field Beamspace," *IEEE Journal of Oceanic Engineering*, vol. 25, no. 2, pp. 262-273, April 2000.

[45] A. Nehorai & M. Hawkes, "Performance Bounds for Estimating Vector Systems," *IEEE Transactions on Signal Processing* vol. 48, no. 6, pp. 1737-1749, June 2000.

[46] J. W. Parkins, S. D. Sommerfeldt & J. Tichy, "Error Analysis of a Practical Energy Density Sensor," *Journal of the Acoustical Society of America*, vol. 108, no. 1, pp. 211-222, July 2000.

[47] M. D. Zoltowski & K. T. Wong, "Closed-Form Eigenstructure-Based Direction Finding Using Arbitrary but Identical Subarrays on a Sparse Uniform Cartesian Array Grid," *IEEE Transactions on Signal Processing*, vol. 48, no. 8, pp. 2205-2210, August 2000.

[48] M. Hawkes & A. Nehorai, "Acoustic Vector-Sensor Processing in the Presence of a Reflecting Boundary," *IEEE Transactions on Signal Processing*, vol. 48, no. 11, pp. 2981-2993, November 2000.

[49] F. Haihong, L. Guolong & H. Junying, "The Direction Estimation Using Combined Sensor with Pressure and Particle Velocity," *Acta Acustica*, vol. 25, no. 6, November 2000.

[50] J. Hui, H. Liu, M. Fan & G. Liang, "Study on the Physical Basis of Pressure and Particle Velocity Combine Processing," *Chinese Journal of Acoustics*, vol. 20, no. 3, pp. 203-212, 2001.

[51] X. Liu, J. Xiang & Y. Zhou, "Passive Tracking and Size Estimation of Volume Target Based on Acoustic Vector Intensity," *Chinese Journal of Acoustics*, vol. 20, no. 3, pp. 225-238, 2001.

[52] R. Aubauer & D. Leckschat, "Optimized Second-Order Gradient Microphone for Hands-Free Speech Recordings in Cars," *Speech Communication*, no. 34, pp. 13-23, April 2001.

[53] P. Tichavský, K. T. Wong & M. D. Zoltowski, "Near-Field/Far-Field Azimuth and Elevation Angle Estimation Using a Single Vector Hydrophone," *IEEE Transactions on Signal Processing*, vol. 49, no. 11, pp. 2498-2510, November 2001.

[54] H. L. Van Trees, *Detection, Estimation, and Modulation Theory, Part IV: Optimum Array Processing*, New York, U.S.A.: Wiley, 2002.

[55] M. T. Silvia & R. T. Richards, "A Theoretical and Experimental Investigation of Low-Frequency Acoustic Vector Sensors," *IEEE Oceans Conference*, vol. 3, pp. 1886-1897, 2002.

[56] K. T. Wong & H. Chi, "Beam Patterns of an Underwater Acoustic Vector Hydrophone Located Away from Any Reflecting Boundary," *IEEE Journal of Oceanic Engineering*, vol. 27, no. 3, pp. 628-637, July 2002.

[57] M. Pesavento, A. B. Gershman & K. M. Wong, "Direction Finding in Partly Calibrated Sensor Arrays Composed of Multiple Subarrays," *IEEE Transactions on Signal Processing*, vol. 50, no. 9, pp. 2103-2115, September 2002.

[58] S. Guiqing, Y. Desen, J. Lanyue & S. Shengguo, "Maximum Likelihood Ratio Detection and Maximum Likelihood DOA Estimation Based on the Vector Hydrophone," *Acta Acustica*, vol. 28, no. 1, January 2003.

[59] J. A. McConnell, "Analysis of a Compliantly Suspended Acoustic Velocity Sensor," *Journal of the Acoustical Society of America*, vol. 113, no. 3, pp. 1395-1405, March 2003.

[60] B. A. Cray, V. M. Evora & A. H. Nuttall, "Highly Directional Acoustic Receivers," *Journal of the Acoustical Society of America*, vol. 113, no. 3, pp. 1527-1533, March 2003.

[61] M. Hawkes & A. Nehorai, "Wideband Source Localization Using a Distributed Acoustic Vector-Sensor Array," *IEEE Transactions on Signal Processing* vol. 51, no. 6, pp. 1479-1491, June 2003.

[62] B. H. Maranda, "The Statistical Accuracy of an Arctangent Bearing Estimator," *IEEE Oceans Conference*, vol. 4, pp. 2127-2132, 2003.

[63] J. C. Shipps & K. Deng, "A Miniature Vector Sensor for Line Array Applications," *IEEE Oceans Conference*, vol. 5, pp. 2367-2370, 2003.

[64] C. M. S. See & A. B. Gershman, "Direction-of-Arrival Estimation in Partly Calibrated Subarray-based Sensor Arrays," *IEEE Transactions on Signal Processing*, vol. 52, no. 2, pp. 329-338, February 2004.

[65] J. L. Butler, A. L. Butler & J. A. Rice, "A Tri-modal Directional Transducer," *Journal of the Acoustical Society of America*, vol. 115, no. 2, pp. 658-665, February 2004.

[66] H.-W. Chen & J.-W. Zhao, "Wideband MVDR Beamforming for Acoustic Vector Sensor Linear Array," *IEE Proceedings – Radar, Sonar & Navigation*, vol. 151, no. 3, pp. 158-162, June 2004.

[67] K. Takeda, T. Itagaki & F. Adachi, "Joint Use of Frequency-Domain Equalization and Transmit/Receive Antenna Diversity for Single-Carrier Transmissions," *IEICE Transactions on Communications*, vol. E87-B, no. 7, pp. 1946-1953, July 2004.

[68] Q. Zhang & T. Le-Ngoc, "Channel-Estimate-Based Frequency-Domain Equalization (CE-FDE) for Broadband Single-Carrier Transmission," *Wireless Communications and Mobile Computing*, vol. 2004, no. 4, pp. 449-461, 2004.

[69] Q. Lu, S. Yang, J. Zhang & S. Piao, "High Resolution DOA Estimation in Beam Space Based on Acoustic Vector-Sensor Array," *Journal of Harbin Engineering University*, vol. 25, no. 4, pp. 440-445, August 2004.

[70] S. Guiqing & L. Qihu, "Acoustic Vector Sensor Signal Processing," *Acta Acustica*, vol. 29, no. 6, November 2004.

[71] J. C. Shipps & B. M. Abraham, "The Use of Vector Sensors for Underwater Port and Waterway Security," *ISA/IEEE Sensors for Industry Conference*, pp. 41-44, 2004.

[72] K. Hayashi & H. Sakai, "A Simple Interference Elimination Scheme for Single Carrier Block Transmission with Insufficient Cyclic Prefix," *International Symposium On Wireless Personal Multimedia Communications*, vol. 2, pp. 577-581, 2004.

[73] C. H. Hansen, *Noise Control : From Concept to Application*, London, U.K. : Taylor & Francis, 2005.

[74] A.-C. Hladky-Hennion, J. K. Cochran, Jr., R. Meyer, D. C. Markley & R. E. Newnham, "The Wagon Wheel Transducer as a vector Sensor and a Directional Projector," *Ceramic Transactions*, vol. 169, pp. 17-38, 2005.

[75] S. A. Vorobyov, A. B. Gershman & K. M. Wong, "Maximum Likelihood Direction-of-Arrival Estimation in Unknown Noise Fields Using Sparse Sensor Arrays," *IEEE Transactions on Signal Processing*, vol. 53, no. 1, pp. 34-43, January 2005.

[76] H.-W. Chen & J. Zhao, "Coherent Signal-Subspace Processing of Acoustic Vector Sensor Array for DOA Estimation of Wideband Sources," *Signal Processing*, vol. 85, pp. 837-847, April 2005.

[77] J. W. van Honschoten, V. B. Svetovoy, G. J. M. Krijnen & M. C. Elwenspoek, "Optimization of a Thermal Flow Sensor for Acoustic Particle Velocity Measurements," *Journal of Microelectromechanical Systems*, vol. 14, no. 3, pp. 436-443, June 2005.

[78] Xu You-gen, Liu Zhi-wen, & Yao Guang-xiang, "Uni-Vector-Sensor SOS/HOS-CSS for Wide-band Non-Gaussian Source Direction Finding," *IEEE International Symposium on Microwave, Antenna, Propagation and EMC Technologies for Wireless Communications Proceedings*, pp. 855-858, 2005.

[79] K. Hayashi & H. Sakai, "Per-Tone Equalization for Single Carrier Block Transmission with Insufficient Cyclic Prefix," *IEICE Transactions on Information and Systems*, vol. E88-D, no. 7, pp. 1323-1330, July 2005.

[80] K. Hayashi, T. Kojima & H. Sakai, "An Adaptive Antenna Array for Single Carrier Modulation with Cyclic Prefix," *Electronics and Communications in Japan*, part 1, vol. 88, no. 9, pp. 38-48, 2005.

[81] W. S. Leon, Y.-C. Liang & C. Xu, "Cyclic Delay Diversity for Single Carrier-Cyclic Prefix Systems," *Asilomar Conference on Signals, Systems and Computers*, pp. 519-523, 2005.

[82] V. Shchurov, *Vector Acoustics of the Ocean*, Vladivostok, Russia: Dalnauka, 2006.

[83] M. E. Lockwood & D. L. Jones, "Beamformer Performance with Acoustic Vector Sensors in Air," *Journal of the Acoustical Society of America*, vol. 119, no. 1, pp. 608-619, January 2006.

[84] C. Y. Lin, J. Y. Wu & T. S. Lee, "A Near-Optimal Low-Complexity Transceiver for CP-free Multi-Antenna OFDM Systems," *IEICE Transactions on Communications*, vol. 89, no. 1, pp. 88-99, January 2006.

[85] D. R. Yntema, W. F. Druyvesteyn & M. Elwenspoek, "A Four Particle Velocity Sensor Device" *Journal of the Acoustical Society of America*, vol. 119, no. 2, pp. 943-951, February 2006.

[86] D. Zha & T. Qiu, "Underwater Sources Location in Non-Gaussian Impulsive Noise Environments," *Digital Signal Processing*, vol. 16, pp. 149-163, March 2006.

[87] H. W. Chen & J. W. Zhao, "A two-dimensional wideband direction-of-arrival estimation algorithm with acoustic vector-sensor array," *Acta Acustica*, vol. 31, no. 3, pp. 270-275, May 2006.

[88] K. T. Wong & M. K. Awad, "Source Tracking with a Vector-Hydrophone," *IEEE Oceans Conference Asia-Pacific*, 2006.

[89] N. Zou, C. C. Swee & B. A. L. Chew, "Vector Hydrophone Array Development and Its Associated DOA Estimation Algorithms," *IEEE Oceans Conference Asia-Pacific*, 2006.

[90] C. Wan, A. Kong & C. Liu, "A Comparative Study of DOA Estimation Using Vector/Gradient Sensors," *IEEE Oceans Conference Asia-Pacific*, 2006.

[91] N. Qi & T. Tian, "Acoustic Vector Hydrophone Array Supergain Energy Flux Beamforming," *International Conference on Signal Processing*, vol. 4, 2006.

[92] J. A. Clark & G. Tarasek, "Localization of Radiating Sources along the Hull of a Submarine Using a Vector Sensor Array," *IEEE Oceans Conference*, 2006.

[93] J. F. McEachern, J. A. McConnell, J. Jamieson & D. Trivett, "ARAP - Deep Ocean Vector Sensor Research Array," *IEEE Oceans Conference*, 2006.

[94] V. Shchurov, *Vector Acoustics of the Ocean*, Vladivostok, Russia: Dalnauka, 2006.

[95] S. A. Elkader, A. B. Gershman & K. M. Wong, "Rank Reduction Direction-of-Arrival Estimators With an Improved Robustness Against Subarray Orientation Errors," *IEEE Transactions on Signal Processing*, vol. 54, no. 5, pp. 2396-2406, May 2006.

[96] C. Qi, Z. Chen, Y. Zhang & Y. Wang, "DOA Estimation and Self-Calibration Algorithm for Multiple Subarrays in the Presence of Mutual Coupling," *IEE Proceedings: Radar, Sonar & Navigation*, vol. 153, no. 4, pp. 333-337, August 2006.

[97] K. Takeda, R. Kawauchi & F. Adachi, "Frequency-Domain Adaptive Antenna Array for Single-Carrier Uplink Transmissions Using Frequency-Domain Equalization," *Symposium on Wireless Personal Multimedia Communications*, pp. 776-780, 2006.

[98] J. Ahmadi-Shokouh & H. Keshavarz, "A Vector-Hydrophone's Minimal Composition for Finite Estimation-Variance in Direction-Finding Near/Without a Reflecting Boundary," *IEEE Transactions on Signal Processing*, vol. 55, no. 6, pp. 2785-2794, June 2007.

[99] Y. Xu, Z. Liu & J. Cao, "Perturbation Analysis of Conjugate MI-ESPRIT for Single Acoustic Vector-Sensor-Based Noncircular Signal Direction Finding," *Signal Processing*, vol. 87, no. 7, pp. 1597-1612, July 2007.

[100] D. J. Schmidlin, "Directionality of Generalized Acoustic Sensors of Arbitrary Order," *Journal of the Acoustical Society of America*, vol. 121, no. 6, pp. 3569-3578, June 2007.

[101] C.-Y. Liu & C.-S. Wang, "Adaptive Antennas Arrays for Interference Cancellation in OFDM Communications Systems with Virtual Carriers," *IEEE Transactions on Vehicular Technology*, vol. 56, no. 4, pp. 1837-1844, July 2007.

[102] A. Abdi, H. Guo & P. Sutthiwan, "A New Vector Sensor Receiver for Underwater Acoustic Communication," *IEEE Oceans Conference*, 2007.

[103] J. Tao, W. Chang & W. Cui, "Vector Field Smoothing for DOA Estimation of Coherent Underwater Acoustic Signals in Presence of a Reflecting Boundary," *IEEE Sensors Journal*, vol. 7, no. 8, pp. 1152-1158, August 2007.

[104] K. P. Arunkumar & G. V. Anand, "Multiple Source Localization in Shallow Ocean using a Uniform Linear Horizontal Array of Acoustic Vector Sensors," *IEEE Region 10 Conference*, 2007.

[105] H. Cox & H. Lai, "Performance of Line Arrays of Vector and Higher Order Sensors," *Asilomar Conference on Signals, Systems and Computers*, pp. 1231-1236, 2007.

[106] H. Lai & K. Bell, "Cramer-Rao Lower Bound for DOA Estimation Using Vector and Higher-Order Sensor Arrays," *Asilomar Conference on Signals, Systems and Computers*, pp. 1262-1266, 2007.

[107] K. P. Arunkumar & G. V. Anand, "Source Localisation in Shallow Ocean using a Vertical Array of Acoustic Vector Sensors," *European Signal Processing Conference*, 2007.

[108] Y. Takahashi, Y. Iwanami & E. Okamoto, "A Time-Domain Block Equalization Scheme on SIMO Frequency Selective Channels," *IEEE Region 10 Conference*, 2007.

[109] S. Mohan, M. E. Lockwood, M. L. Kramer & D. L. Jones, "Localization of Multiple Acoustic Sources with Small Arrays Using a Coherence Test" *Journal of the Acoustical Society of America*, vol. 123, no. 4, pp. 2136C2147, April 2008.

[110] Y. Xu & Z. Liu, "Noncircularity-Exploitation in Direction Estimation of Noncircular Signals with an Acoustic Vector-Sensor," *Digital Signal Processing*, vol. 18, pp. 777-796, 2008.

[111] K. G. Nagananda & G. V. Anand "Subspace Intersection Method of Bearing Estimation in Shallow Ocean Using Acoustic Vector Sensors," *European Signal Processing Conference*, 2008

[112] Y. H. Wang, J. Q. Zhang, B. Hu & J. He, "Hypercomplex Model of Acoustic Vector Sensor Array with Its Application for the High Resolution Two Dimensional Direction of Arrival Estimation," *IEEE International Instrumentation and Measurement Technology Conference*, 2008.

[113] L. Guanfang, Z. Anbang, H. Junying & S. Guocang, "The Application of Empirical Mode Decomposition in Target-starting Sound Detection," *IEEE Vehicle Power and Propulsion Conference*, 2008.

[114] G. Yunchao, S. Enfang, L. Baifeng & S. Zhengyan, "Application of Complex Empirical Mode Decomposition in Separation of Multiple Targets Using a Single Vector Sensor," *IEEE International Conference Neural Networks & Signal Processing*, pp. 294-298, 2008.

[115] D. Zha, "Underwater 2-D Source Localization Based On Fractional Order Correlation Using Vector Hydrophone," *Congress on Image and Signal Processing*, pp. 31-34, 2008.

[116] G. Yunchao, S. Enfang & S. Zhengyan, "Comparison of EMD and Complex EMD in Signal Processing," *Congress on Image and Signal Processing*, pp. 141-145, 2008.

[117] H. Lai, K. Bell & H. Cox, "DOA Estimation Using Vector Sensor Arrays," *Asilomar Conference on Signals, Systems & Computers*, pp. 293-297, 2008.

[118] L. Yun-fei & Z. Cui-e, "A Study of Channel Estimation in OFDM System Based on a Single Vector Sensor for Underwater Acoustic Communications," *International Conference on Wireless Communications, Networking and Mobile Computing*, 2008.

[119] Y. Yuan, B. Zhang, D. Fan & G. Tong, "DFT and PSD for Estimating DOA with an Active Acoustic Array," *IEEE International Conference on Automation and Logistics*, pp. 694-699, 2008.

[120] J. He & L. Zhong, "Underwater Acoustic Azimuth and Elevation Angle Estimation Using Spatial Invariance of Two Identically Oriented Vector Hydrophones at Unknown Locations in Impulsive Noise," *Digital Signal Processing*, vol. 19, pp. 452-462, 2009.

[121] J. He, S. Jiang, J. Wang & Z. Liu, "Direction Finding in Spatially Correlated Noise Fields with Arbitrarily-Spaced and Far-Separated Subarrays at Unknown Locations," *IET Radar, Sonar & Navigation*, vol. 3, no. 3, pp. 278-284, June 2009.

[122] P. K. Tam & K. T. Wong, "Cramér-Rao Bounds for Direction Finding by an Acoustic Vector-Sensor Under Non-Ideal Gain-Phase Responses, Non-Collocation, or Non-Orthogonal Orientation," *IEEE Sensors Journal*, vol. 9, no. 8, pp. 969-982, August 2009.

[123] D. Kasilingam, D. Schmidlin & P. Pacheco, "Super-Resolution Processing Technique for Vector Sensors," *IEEE Radar Conference*, 2009.

[124] H. Jin & L. Zhong, "Two-Step Azimuth and Elevation Angle Estimation with vector Hydrophone Array," *Chinese Journal of Electronics*, vol. 18, no. 4, pp. 754-758, October 2009.

[125] F. Adachi, H. Tomeba & K. Takeda, "Frequency-Domain Equalization for Broadband Single-Carrier Multiple Access," *IEICE Transactions on Communications*, vol. E82-B, no. 5, pp. 1441-1456, May 2009.

[126] C.-Y. Liu, Y.-F. Chen & C.-P. Li, "Blind Beamforming Schemes in SC-FDMA Systems with Insufficient Cyclic Prefix and Carrier Frequency Offset," *IEEE Transactions on Vehicular Technology*, vol. 58, no. 9, pp. 4848-4859, November 2009.

[127] Y.-R. Huang, C. C. Fung & K. T. Wong, "Interference Suppression for OFDM Systems With Insufficient Guard Interval Using Null Subcarriers," *IEEE Signal Processing Letters*, vol. 16, no. 11, pp. 929-932, November 2009.

[128] D. Kasilingam, D. Schmidlin & P. Pacheco, "Super-Resolution Processing Technique for Vector Sensors," *IEEE Radar Conference*, 2009.

[129] T. G. H. Basten, H. E. de Bree, W. F. Druyvesteyn & J. W. Wind, "Multiple Incoherent Sound Source Localization Using a Single Vector Sensor," *International Congress on Sound and Vibration*, 2009.

[130] Z. Lan-yue & Y. De-sen, "Research on the Application of Extended-Aperture Algorithm based on Uniformly Vector Hydrophone Linear Array," *IEEE Conference on Industrial Electronics and Applications*, pp. 3016-3021, 2009.

[131] A. Agarwal, A. Kumar, M. Aggarwal & R. Bahl, "Design and Experimentation with Acoustic Vector Sensors," *International Symposium on Ocean Electronics*, pp. 139-146, 2009.

[132] Y. De-sen, C. Huan, S. Sheng-guo & X. Di, "The High Resolution Orientation Research of Under Water Composed Array Sources in Near Field via the Most Likely Estimation," *International Conference on Information Engineering and Computer Science*, 2010.

[133] K. G. Nagananda & G. V. Anand, "Subspace Intersection Method of High-Resolution Bearing Estimation in Shallow Ocean Using Acoustic Vector Sensors," *Signal Processing*, no. 90, pp. 105-118, January 2010.

[134] K. T. Wong, "Acoustic Vector-Sensor 'Blind' Beamforming & Geolocation for FFH-Sources," *IEEE Transactions on Aerospace and Electronic Systems*, vol. 46, no. 1, pp. 444-449, January 2010.

[135] Y. I. Wu, K. T. Wong & S.-k. Lau, "The Acoustic Vector-Sensors Near-Field Array-Manifold," *IEEE Transactions on Signal Processing*, vol. 58, no. 7, pp. 3946-3951, July 2010.

[136] K. T. Wong, Y. I. Wu & S.-k. Lau, "The Acoustic Vector-Sensor's Near-Field Array-Manifold," *IEEE Transactions on Signal Processing*, vol. 58, no. 7, pp. 3946-3951, July 2010.

[137] J.-W. Tao, W.-X. Chang & W. Cui, "Direction-Finding of Coherent Signals Based on Cylindrical Vector-Hydrophones Array," *Signal, Image and Video Processing*, vol. 4, no. 2, pp. 221-232, 2010.

[138] E. H. G. Tijs, G. C. H. E. de Croon, J. W. Wind, B. Remes, C. De Wagter, H.-E. de Bree, R. Ruijsink, "Hear-and-Avoid for Micro Air Vehicles," *International Micro Air Vehicle Conference*, 2010.

[139] M. Shujau, C. H. Ritz & I. S. Burnett, "Using In-Air Acoustic Vector Sensors for Tracking Moving Speakers," *International Conference on Signal Processing and Communication Systems*, 2010.

[140] P. Wang, G.-j. Zhang, J.-j. Xiong, C.-y. Xue & W.-d. Zhang, "Root-MUSIC Algorithm with Real-Valued Eigende-Composition for Acoustic Vector Sensor Array," *International Conference on Pervasive Computing Signal Processing and Applications*, pp. 652-656, 2010.

[141] Z. Yuan, X. Gu & K. Hu, "A Modified DOA Estimation Algorithm for Coherent Signals Based on Single Acoustic Vector Hydrophone," *International Congress on Image and Signal Processing*, pp. 3830-3832, 2010.

[142] A. Abdi, H. Guo, A. Song & M. Badiey, "An Overview of Underwater Acoustic Communication via Particle Velocity Channels: Channel Modeling and Transceiver Design," *Meeting of the Acoustical Society of America*, vol. 9, pp. 070002, 2010.

[143] P. Felisberto, P. Santos & S. M. Jesus, "Tracking Source Azimuth Using a Single Vector Sensor," *International Conference on Sensor Technologies and Applications*, pp. 416-421, 2010.

[144] B. Xu, J. Wind, H.-E. De Bree, T. Basten & E. Druyvesteyn, "Amplitude, Phase, Location and Orientation Calibration of an Acoustic Vector Sensor Array, Part I: Theory," *Proceedings of Meetings on Acoustics*, vol. 9, 2010.

[145] T. . Basten, J. Wind, B. Xu, H.-E. De Bree, & E. Druyvesteyn, "Amplitude, Phase, Location and Orientation Calibration of an Acoustic Vector Sensor Array, Part II: Experiments," *Proceedings of Meetings on Acoustics*, vol. 9, 2010.

[146] D. Xie, J. Huang & H. Ge, "Localization of Near-field Sources with Partly Calibrated Subarray-based Array," *IEEE Conference on Industrial Electronics and Applications*, pp. 1758-1761, 2010.

[147] T. Li, J. Tabrikian & A. Nehorai, "A Barankin-Type Bound on Direction Estimation Using Acoustic Sensor Arrays," *IEEE Transactions on Signal Processing*, vol. 59, no. 1, pp. 431-435, January 2011.

[148] Y. Song, C. C. Fung, K. T. Wong, H. Meng & D.-F. Tseng, "Precoder/two-stage equaliser for block-based single-carrier transmission with insufficient guard interval," *Electronics Letters*, vol. 47, no. 13, pp. 746-748, 23 June 2011.

[149] D. Levin, S. Gannot & E. A. P. Habets, "Direction-of-Arrival Estimation Using Acoustic Vector Sensors in the Presence of Noise," *IEEE International Conference on Acoustics, Speech, Signal Processing*, vol. 4, pp. 104-107, 2011.

[150] X. Zhong, A. Premkumar, A. Madhukumar & L. C. Tong, "Multi-modality Likelihood Based Particle Filtering For 2-D Direction of Arrival Tracking Using A Single Acoustic Vector Sensor," *International Workshop on Acoustics and Video Coding and Communication*, 2011.

[151] H. S. Lim, K. Rameshchandra & W. S. Toh, "Estimation and Compensation of Rotation Perturbation in Linear 2D Acoustic Vector Sensor Array," *IEEE Oceans Conference*, 2011.

[152] P. Parvazi, M. Pesavento & A. B. Gershman, "Direction-of-Arrival Estimation and Array Calibration for Partly-Calibrated Arrays," *IEEE International Conference on Acoustics, Speech, and Signal Processing*, pp. 2552-2555, 2011.

[153] K. T. Wong, Y. I. Wu, X. Yuan, S.-k. Lau & S.-k. Tang, "A Directionally Tunable but Frequency-Invariant Beamformer for an Acoustic Velocity-Sensor Triad to Enhance Speech Perception," *International Conference on Networked Sensing Systems*, 2011.

[154] Y. I. Wu & K. T. Wong, "Acoustic Near-Field Source Localization by Two Passive Anchor Nodes," *IEEE Transactions on Aerospace and Electronic Systems*, vol. 48, no. 1, pp. 159-169, January 2012.

[155] K. T. Wong, Y. I. Wu, Y.-S. Hsu & Y. Song, "A Lower Bound of DOA-Estimates from an Array Randomly Subject to Sensor-Breakdown," *IEEE Sensors Journal*, vol. 12, no. 5, pp. 911-913, May 2012.

[156] K. T. Wong & X. Yuan, " 'Vector Cross-Product Direction-Finding' with an Electromagnetic Vector-Sensor of Six Orthogonally Oriented but Spatially Non-Collocating Dipoles / Loops," *IEEE Transactions on Signal Processing*, vol. 59, no. 1, pp. 160-171, May 2011.

[157] M. K. Awad & K. T. Wong, "RLS Source-Tracking Using One Acoustic Vector-Sensor," *IEEE Transactions on Aerospace & Electronic Systems*, vol. 48, no. 3, July 2012.

[158] Y. Song & K. T. Wong, "Closed-Form Direction Finding Using Collocated but Orthogonally Oriented Higher-Order Acoustic Sensors," *IEEE Sensors Journal*, vol. 12, no. 8, pp. 2604-2608, August 2012.

[159] Y. Song & K. T. Wong, "A Lower Bound of Direction-of-Arrival Estimation for Acoustic Vector Sensor with Sensor Breakdown," *IEEE Transactions on Aerospace & Electronic Systems*, vol. 48, no. 4, pp. 3703-3708, October 2012.

[160] Y. Song & K. T. Wong, "Three Dimensional Localization of a Near-Field Emitter of Unknown Spectrum Using an Acoustic Vector Sensor," *IEEE Transactions on Aerospace & Electronic Systems*, vol. 49, no. 2, pp. 1035-1041, April 2013.

[161] Y. Song, K. T. Wong & F. J. Chen, ""Blind" Calibration of an Array of Acoustic Vector-Sensors Suffering Gain Errors / Mis-Location / Mis-Orientation," under review by the *IEEE Transactions on Signal Processing*.

[162] Y. Song & K. T. Wong, "Azimuth-Elevation Direction Finding Using a Microphone and Three Orthogonal Velocity Sensors as a Non-Collocated Subarray," *Journal of the Acoustical Society of America*, vol. 133, no. 4, pp. 1987-1995, April 2013.

[163] Y. Song & K. T. Wong, ""Blind" Calibration of Electromagnetic Vector Sensors Whose Dipole-Triads/Loop-Triads Deviate from Their Nominal Gains / Phases / Orientations / Locations," under review by the *IEEE Transactions on Signal Processing*.

[164] Y. Song, K. T. Wong & Yung-Fang CHEN, ""Blind" Reception-Beamforming to Null Unknown Interference for Block-Based Single-Carrier Transmission with an Insufficient Guard Interval," under review by the *IEEE Wireless Communications Letters*.

[165] Y. Song & K. T. Wong, "Acoustic Direction Finding Using a Spatially Spread Tri-Axial Velocity Sensor," under review by the *IEEE Transactions on Aerospace & Electronic Systems*.